Reflection Seismology for Nondestructive Evaluation

by

Osamu Suzuki

Submitted to the Department of Civil and Environmental Engineering
in partial fulfillment of the requirements for the degree of

Master of Science in Civil and Environmental Engineering

at the

MASSACHUSETTS INSTITUTE OF TECHNOLOGY

June 2002

Author .....
Department of Civil and Environmental Engineering
May 17, 2002

Certified by .....
Shi-Chang Wooh
Associate Professor of Civil and Environmental Engineering
Thesis Supervisor

Accepted by .....
Oral Buyukozturk
Chairman, Department Committee on Graduate Studies

Reflection Seismology for Nondestructive Evaluation

by

Osamu Suzuki

Submitted to the Department of Civil and Environmental Engineering
on May 17, 2002, in partial fulfillment of the
requirements for the degree of
Master of Science in Civil and Environmental Engineering

Abstract

Providing reliable results in understandable form is challenging for ultrasonic nondestructive evaluation. It is especially important to take into account the various parameters influencing the results. Our approach is unique in that (a) an array of ultrasonic receivers are used to reduce noise, (b) several kinds of filters are applied and (c) it provides geometrically correct images by migrating the data.

The main objective of this study is to adopt and extend the capabilities of reflection seismology which is commonly used in the area of geophysical survey. Various parameters have been studied in an effort to reduce noise and improve accuracy. The noise reduction method by considering the effects of beam directivity are discussed.

The techniques developed in this study have been investigated by both simulation and experimental studies for aluminum, mortar and concrete specimens. It has been shown that reflection seismology is feasible for small scale structures by considering the fundamental characteristics such as the dimension of wave sources and specimen.

Thesis Supervisor: Shi-Chang Wooh
Title: Associate Professor of Civil and Environmental Engineering

Acknowledgments

This study in MIT is a challenge for me. I cannot complete it without guidance and assistance of many people. Professor Shi-Chang Wooh offered me to use NDE lab where all experiments described in this thesis were carried out. He also held meeting every week and gave me a appropriate advice. His guidance encourage me to complete this study. Ji-Yong Wang helped me in NDE lab. He taught me the direction of the instruments, techniques for the experiment, and so on. He also maintain the computer network in NDE lab. Owing to his guidance, I could do an experiment.

I am a employee of East Japan Railway Company, they approve me to study in MIT for two years. They support me not only financially but also mentally. I appreciate their support.

Finally, I would like to say thank you for all staffs in MIT to offer me wonderful environment.

Contents

List of Tables

List of Figures

Chapter 1

Introduction

1.1 Needs of reliable and understandable NDE

Civil structures, such as bridges, tunnels and roads, should be inspected periodically to maintain their quality and safety, for which nondestructive evaluation (NDE) provides important inspection tools. In spite of the importance of NDE, visual inspection is still used dominantly for inspecting large structures. One of the reasons that ultrasonic NDE is not commonly used is the difficulty associated with the interpretation of its results. In most case, the ultrasonic NDE method presents complex waveform or series of numbers, which requires special skills to interpret. It is especially difficult to interpret the signals coming from cementatious materials because of the uncertainties introduced by the heterogeneous nature of materials. In order to resolve these problem and extend the use of NDE to var-

ious materials, it is necessary to develop techniques capable of providing the reliable and understandable and reliable results.

1.2 Imaging techniques

One of the way to present the data is imaging. Although it is desirable to obtain quantitative results, imaging provides intuitive and easy interpretation as summarized in reference [1]. Of the few methods for imaging cementatious materials by ultrasonic testing, it is interesting to note the following two methods: synthetic aperture focusing radar techniques [2], [3] and migration in reflection seismology [4], [5], [6]. For example, Krause *et al.* [7] realizes the image of internal duct in concrete slab by synthetic aperture focusing radar techniques and Liu *et al.* discuss the 2D [8] and 3D [9] imaging techniques for surface breaking cracks using reflection seismology which is our interest.

1.3 Reflection seismology

Reflection seismology is a technique commonly used in geophysical exploration employed in exploring Earth's subsurfaces [10], [4], [5]. This method is similar to the ultrasonic pulse-echo testing, but it is different in that the reflection seismology use an array of receivers to reduce noise. It is because the signal-noise-ratio of the measured data is poor due to the heterogeneous nature of soil subsurface [4]. This method also utilize include imaging process, "migration". Thus, due to the unique advantages of reflection seismology, the

same technique may be used for testing materials and structures using ultrasound despite that it requires larger number of measurements.

1.4 The goal of this study

The goal of this study to develop a method for detecting internal cracks or voids in material based on reflection seismology. Because of the difference in scale between the Earth and small scale structures, the scale effects play important role. The beam directivity is one of the critical factor considered in this study. Thus, this study includes not only analysis of the beam directivity but also to eliminate the effect.

Chapter 2

Reflection seismology

2.1 Introduction

Reflection seismology is one of the common techniques to explore the Earth's sub-surface. The procedure used in reflection seismology is similar to that of ultrasonic pulse-echo testing, in that both are based on the time-of-flight measurements. In operation, an incident wave transmitted from a wave source and reflected off a boundary or delamination is recorded by a receiver. In the measured waveform, the travel time of the wave represents the depth of the boundary or delamination. In contrast to pulse-echo testing, the reflected seismic waves are usually concealed by noise, since the Earth's sub-surface consists of various materials made of complex constituents. In order to penetrate into deep area, waves of extremely low frequency, having omni-directivities, are used.

Some techniques have been developed [4, 5] in order to reconstruct clear images of subsurface structures under these challenging conditions. The uniqueness of these techniques is on the data acquisition using an array of receivers, and their inversion process considerably reducing the noise. The low signal-noise-ratio (SNR) and the omni-directivity beam are also common in the ultrasonic pulse-echo testing of concrete structures, which prohibits clear imaging. In this thesis, the methods used in reflection seismology are extended to the for nondestructive evaluation (NDE) of concrete structures.

2.2 Data acquisition

Two-dimensional (2D) survey is a common data acquisition method used in reflection seismology, because it does not require complex calculations. In a 2D survey, several receivers are placed along the survey line at an interval of equal distances. Figure 2-1 shows a typical arrangement of receivers and transmitter.

The resulting distance between the transmitter and a receiver is called "offset". The offset is determined by considering the required resolution and the conditions of the survey site. Two-dimensional surveys consist of the following procedures: (1) wave propagates from the transmitter, (2) the reflected waves are recorded by all receivers, (3) the transmitter and all the receivers are shifted by a certain distance; the shifting distance is typically a half of the interval between the receivers, (4) continue along the survey line, as shown in Fig. 2-2.

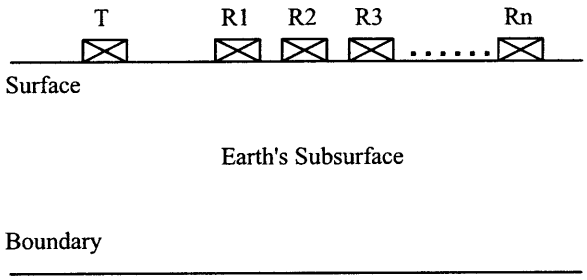

Figure 2-1: A typical arrangement of transmitter and receivers in reflection seismology, T = transmitter, R1, R2, $\cdots$, Rn = receiver.

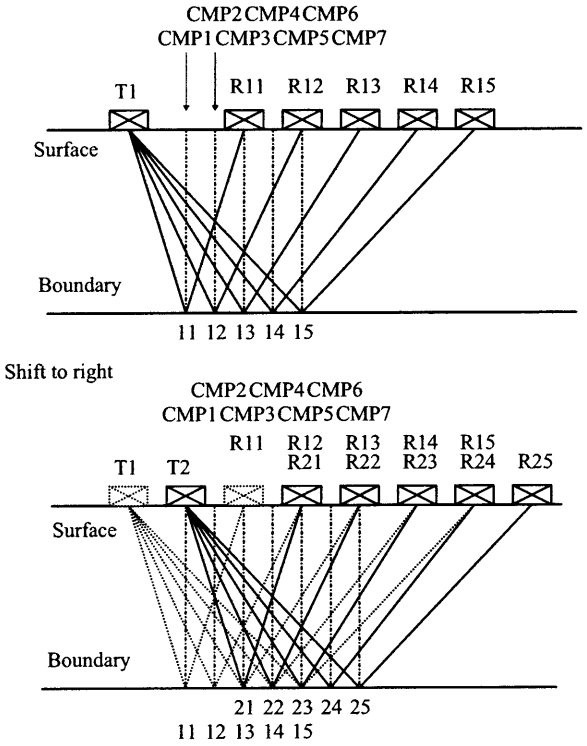

Figure 2-2: Two dimensional survey is carried out by the following procedures: (1) wave propagates from the transmitter, T1, (2) the reflected waves are recorded by receivers, R11, R12,$\cdots$, R15, (3) the transmitter is shifted to the position to T2 and receivers are shifted to R21, $\cdots$, R25, (4) a wave propagates from the transmitter, T2, and they continue measuring along the survey line, T1, T2: transmitter, R11, $\cdots$, R25: receivers, 11, $\cdots$, 25: the reflection point of each wave.

2.3 Deconvolution

Deconvolution is a filtering process that could improve the temporal resolution. The most common method to improve temporal resolution is the bandpass filtering, which can eliminate the signal of different frequency bands from the reflected wave. On the other hand, a deconvolution process can reduce the pulse width using the process as follows. Suppose that $s(t)$ is the measured signal, $e(t)$ is the reflected echo signal, $w(t)$ is the input signal and $n(t)$ is the noise, then the measured signal can be expressed as the convolution of $w(t)$ and $e(t)$ plus $n(t)$, i.e.,

$$s(t) = w(t) * e(t) + n(t). \tag{2.1}$$

Neglecting noise, it can be rewritten as

$$s(t) = w(t) * e(t). \tag{2.2}$$

We may introduce a filter function $a(t)$ which transforms the input signal into a spike pulse. The filter function has the following characteristics:

$$w(t) * a(t) = i(t), \tag{2.3}$$

where $i(t)$ is a spike pulse. If this filter function is convolved with the measured signal, then a series of spike pulses can be obtained where the number of spike pulses is equal to that of the reflections:

$$s(t) * a(t) = r(t), \tag{2.4}$$

where $r(t)$ represents the series of spike pulses. Using this process, the reflected waves can be compressed into spike pulses so that the wave consisting of several echoes is deconvolved into impulse signals.

The Wiener prediction filter [5] is employed in this study. The Wiener prediction filter is convenient in that it is only necessary to compute the auto-correlation coefficients of the measured signal. The Wiener prediction filter is defined as follows:

$$\begin{pmatrix} (1+\epsilon)r_0 & r_1 & r_2 & \dots & r_n \\ r_1 & (1+\epsilon)r_0 & r_1 & \dots & r_{n-1} \\ r_2 & r_1 & (1+\epsilon)r_0 & \dots & r_{n-2} \\ \vdots & \vdots & \vdots & \vdots & \vdots \\ r_n & r_{n-1} & r_{n-2} & \dots & (1+\epsilon)r_0 \end{pmatrix} \begin{pmatrix} a_0 \\ a_1 \\ a_2 \\ \vdots \\ a_{n-1} \end{pmatrix} = \begin{pmatrix} r_\alpha \\ r_{\alpha+1} \\ r_{\alpha+2} \\ \vdots \\ r_{\alpha+n-1} \end{pmatrix} \tag{2.5}$$

where r is the auto correlation coefficient, a is the filter component, α is the prediction time lag, and ϵ is the percent of prewhitening.

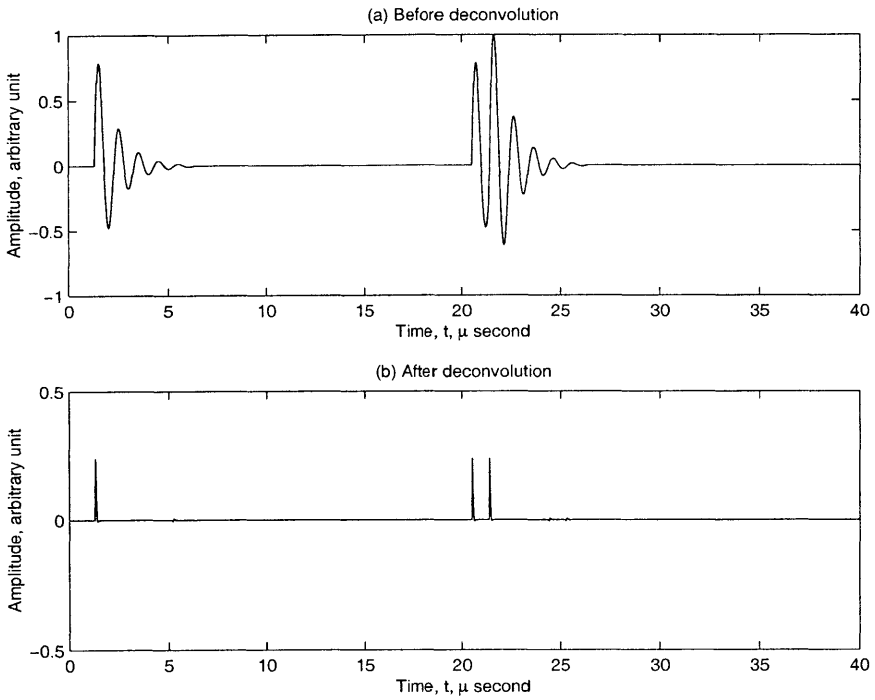

Figure 2-3: Demonstration of the Wiener prediction filtering. The simulation data containing the two close echoes (a) can be resolved (b) using the Wiener filter. See Appendix A-1 for the listing of this simulation program.

An example of Wiener deconvolution is shown in Fig. 2-3. In this simulation case, three reflected waves arrive, but only two waves can be distinguished in the time domain. The deconvolved signal clearly demonstrates the improved temporal resolution. Appendix A-1 show the Matlab programs to produce the simulation waveform in this figure and deconvolve the signal into the spike signals.

2.4 Data stacking

In order to improve the SNR, a group of signals are added together using the process called "data stacking". This process results in the amplification of the peak amplitude and the reduction of noise. Data stacking consists mainly of the following three steps: (1) data sorting—grouping of the signals, (2) normal moveout (NMO)—lining up the peak amplitudes of the reflected signals, and (3) stacking—adding the shifted signals.

2.4.1 Common midpoint (CMP) sorting

Several kinds of data sorting methods are available, of which the Common Midpoint (CMP) sorting is perhaps the most common data sorting algorithm for 2D surveying. The CMP is the middle point between the transducer and the receiver on the surface. For example, in Fig. 2-2, the waves traveling along the paths T1-13-R13 and T2-21-R21 have the same CMP. The reflected waves, having the same CMP are grouped together. If the reflector, i.e., the boundary or delamination, is flat and parallel to the surface, then all the waves will be reflected from the same point on the reflector. Thus, it is also referred to as "Common Depth Point (CDP) sorting".

2.4.2 NMO correction

The NMO correction is to compensate in time and line up the peaks of the reflected waves. The waves grouped by the CMP sorting are reflected from the same or in the close vicinity

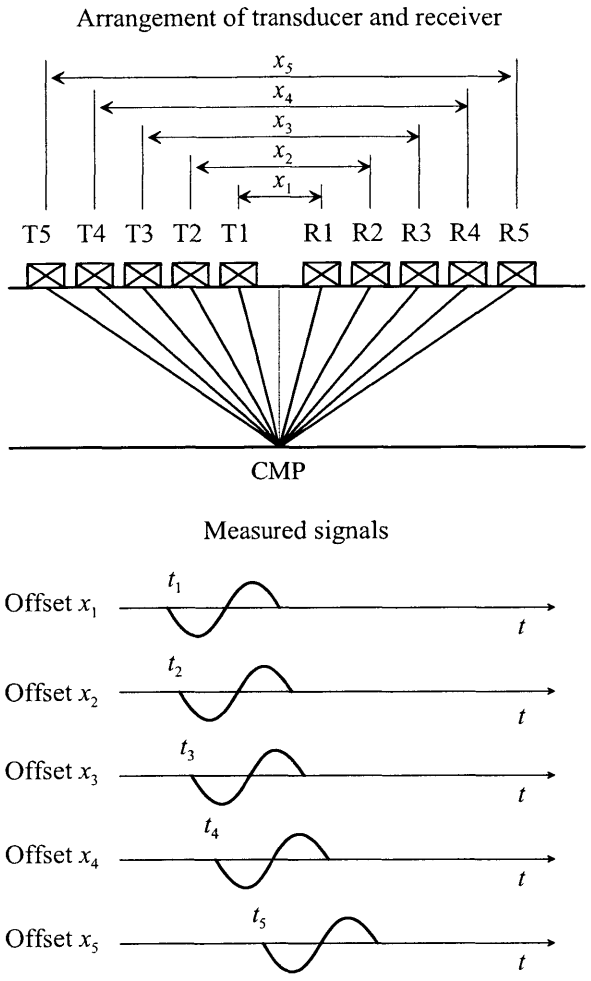

Figure 2-4: Illustration of the measured signal, which have the same CMP. The arrival time is different for each wave because the length of travel paths is different.

of the reflection point. However, the travel length of each wave is different because of the different distances between the transducer and receiver for each waveform. As a result, the arrival time of each wave is different, as illustrated in Fig. 2-4. To equalize the arrival times of each wave reflected from the same point, the time-depth relationship should be

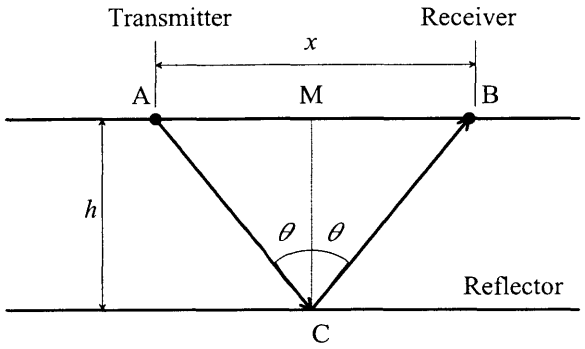

Figure 2-5: Wave path ACB. The wave emitted from transmitter A is reflected from point C, and received by B.

compensated to the standard travel time-depth relationship. In most cases, the standard travel time-depth relationship is condition for zero offset.

Figure 2-5 shows the wave path emitted from a source point A and received by receiver B. Then travel time of the wave is written as

$$t_x = \frac{\sqrt{x^2 + 4h^2}}{c}, \tag{2.6}$$

where x is offset between the transmitter and receiver, h is the depth of the reflector, and c is the wave propagation velocity in the medium.

Setting the depth of reflector as a variable, z, the travel time-depth relationship can be rewritten as

$$t_x = \frac{\sqrt{x^2 + 4z^2}}{c}, \tag{2.7}$$

and the standard travel time-depth relationship for zero offset is

$$t_0 = \frac{2z}{c}. \tag{2.8}$$

The difference between the zero offset and x-offset data is

$$\Delta t_x = t_x - t_0 = \frac{\sqrt{x^2 + 4z^2}}{c} - \frac{2z}{c}. \tag{2.9}$$

Substitute Eq. (2.8) to Eq. (2.9), we get

$$\Delta t_x = t_0 \left[\left\{ 1 + \left(\frac{x}{ct_0} \right)^2 \right\}^{\frac{1}{2}} - 1 \right]. \tag{2.10}$$

This is so called the Normal moveout (NMO). To compensate for the travel time-depth relation on the x offset data, the signals are shifted in time by this NMO. A compensated signal can now be described as

$$s_{xc}(t_0) = s_x(t - \Delta t_x), \tag{2.11}$$

where $s_{xc}(t_0)$ is the compensated signal, and $s_x(t - \Delta t_x)$ is the signal measured at a point with an offset of x.

2.4.3 Stacking

Figure 2-6 schematically illustrates the process for NMO correction and stacking. After the processing, the amplitude of the reflected wave is boosted and that of both coherent and incoherent noises is reduced. Coherent noises are introduced due to the interferences by the wave modes other than the mode in use. For example, longitudinal waves (P-wave) can be easily interfered with surface (R) or shear (S) waves traveling at different velocities. The NMO process is used to compensate for the P-wave, then the other modes are randomly diluted and thus the coherent noise can be canceled off. The compensated and stacked signal for the kth CMP should appear to be

$$s_k(t_0) = \sum_{i=1}^{N} s_{k,i}(t - \Delta t_{k,i}), \tag{2.12}$$

where $s_{k,i}(t)$ is the signal measured by the ith receiver from kth CMP, and i is an index to denote receivers.

2.5 Migration

The stacked signals contain the information about the location of the CMP and the time history of the reflected wave. Thus, they can be mapped in the x-t domain. On the other hands, the locations of discontinuities (i.e., crack, voids, etc.) are described in the x-z

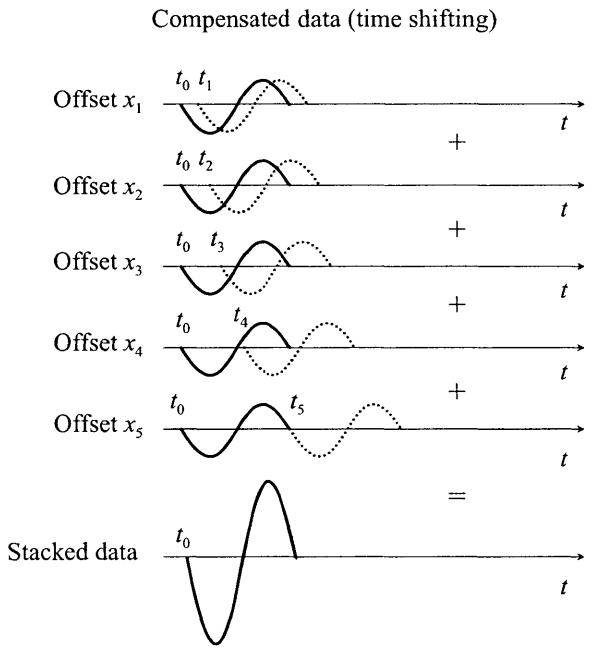

Figure 2-6: Schematic illustration of the processes for NMO correction and stacking procedure. The amplitude of the reflected wave is boosted up after this process.

domain. Migration is the process to transform the measured time histories from the x-t domain to those in the x-z domain.

In the x-t domain, all reflectors are geometrically mapped under each CMP. For a horizontal reflector, the location of the reflector is identical to that in the x-t domain. However, for an inclined reflector, the reflection points are not actually underneath the CMP but somewhere on the arc of a circle centered at the CMP.

Figure 2-7 illustrates the migration process, in which the points A and B are the CMPs on the surface and the line CD is a discontinuity to be mapped. Consider the two ray paths AC and BD. The time required for a round trip along these paths are t_a and t_b, respectively. It is clearly observed from the figure that the line segment CD appears as C'D' in the x-t domain. The migration is to manipulate the data by correcting this distortion using the geometric transformation that maps the data from the x-t domain to the x-z domain.

The migration is commonly carried out in the f-k domain, in which the measured data are first transformed from the x-t domain to the ω-k_x domain, where ω is the angular frequency and k_x is the wavenumber in the x-direction. Then, they are geometrically transformed from the ω-k_x domain to the k_x-k_z domain. At last, the inverse Fourier transform is carried out over both k_x and k_z to obtain the actual location in the x-z domain. We assume that the wave velocity in the medium is constant and that the reflector consists of multiple of point reflectors acting as point sources. The f-k migration process is described below.

The compressional wave field at a point (x, y, z) is denoted as $\phi(x, z, t)$, and the wave field measured on the surface is denoted as $\phi(x, 0, t)$. The objective is to find the location

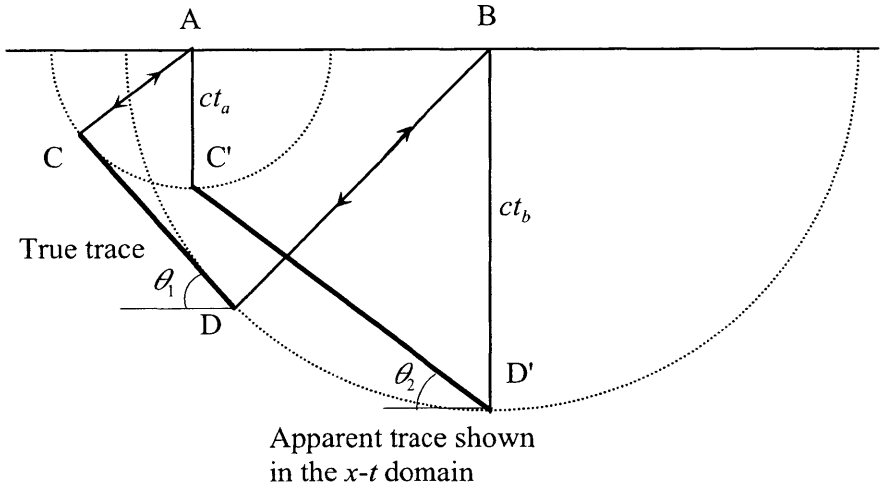

Figure 2-7: Geometric distortion introduced by the cylindrical propagation of waves. The line segment displayed in x-t domain is different from the actual one.

of the reflectors, $\phi(x, z, 0)$. In other words, the f-k migration is the transformation of the function $\phi(x, 0, t)$ to $\phi(x, z, 0)$. In a homogeneous and isotropic space, the wave equation is written as

$$\left(\frac{\partial^2}{\partial x^2} + \frac{\partial^2}{\partial z^2} - \frac{1}{c^2}\frac{\partial^2}{\partial t^2}\right)\phi(x, y, z) = 0. \tag{2.13}$$

Taking the Fourier transform over t and x, we get

$$\frac{\partial^2}{\partial z^2}\widehat{\phi}(k_x, z, \omega) + \left(\frac{\omega^2}{c^2} - k_x^2\right)\widehat{\phi}(k_x, z, \omega) = 0. \tag{2.14}$$

Note that the two-dimensional Fourier transform and its inverse transform are defined as

$$\widehat{\phi}(k_x, z, \omega) = \int\int \phi(x, z, t) \exp[j(k_x x - \omega t)] dx dt, \tag{2.15}$$

$$\phi(x, z, t) = \left(\frac{1}{2\pi}\right)^2 \int\int \widehat{\phi}(k_x, z, \omega) \exp[-j(k_x x - \omega t)] dk_x d\omega, \tag{2.16}$$

where j is unit imaginary number. There exist two solutions in Eq. (2.14): one propagating upward and the other propagating downward. However, this solution is for one-way wave equation, and the measured travel time is for a round trip. Thus, we should use half the velocity to compensate for this. Considering the upward wave, the solution becomes

$$\widehat{\phi}(k_x, z, \omega) = \widehat{\phi}(k_x, 0, \omega) \exp\left[-j\left(\frac{\omega^2}{(c/2)^2} - k_x^2\right)^{\frac{1}{2}} z\right]. \tag{2.17}$$

This is also a solution of the following one-way wave equation,

$$\frac{\partial}{\partial z}\widehat{\phi}(k_x, z, \omega) = -j\left(\frac{4\omega^2}{c^2} - k_x^2\right)^{\frac{1}{2}} \widehat{\phi}(k_x, z, \omega). \tag{2.18}$$

Now, we define the vertical wave number as

$$k_z = \left(\frac{4\omega^2}{c^2} - k_x^2\right)^{\frac{1}{2}}. \tag{2.19}$$

Substituting Eq. (2.19) into Eq. (2.17), we get

$$\widehat{\phi}(k_x, z, \omega) = \widehat{\phi}(k_x, 0, \omega) \exp(-jk_z z). \tag{2.20}$$

This expression shows the relationship between the wave field at an arbitrary position and that at the surface. Therefore, the wave field at an arbitrary position and time can be obtained by the inverse Fourier transform of Eq. (2.20).

$$\phi(x, z, t) = \left(\frac{1}{2\pi}\right)^2 \int\int \hat{\phi}(k_x, 0, \omega) \exp\left[-j\left(k_x x + k_z z - \omega t\right)\right] dk_x d\omega. \tag{2.21}$$

The location of the reflectors is obtained by substituting $t = 0$ as

$$\phi(x, z, 0) = \left(\frac{1}{2\pi}\right)^2 \int\int \hat{\phi}(k_x, 0, \omega) \exp\left[-j\left(k_x x + k_z z\right)\right] dk_x d\omega. \tag{2.22}$$

After all, the relationship between time signals and location of cracks is obtained. However, this equation is described in the ω-k_x domain. Then the equation is transformed to k_x-k_z domain. Rewriting Eq. (2.19)

$$\omega = \frac{c}{2}\left(k_x^2 + k_z^2\right)^{\frac{1}{2}}, \tag{2.23}$$

and differentiating, we get

$$d\omega = \frac{c}{2}\frac{k_z}{(k_x^2 + k_z^2)^{\frac{1}{2}}}dk_z. \tag{2.24}$$

Substituting Eq. (2.23) and Eq. (2.24) into Eq. (2.22), the solution for constant wave velocity migration is obtained as

$$\phi(x,z,0) = \left(\frac{1}{2\pi}\right)^2 \int\int \left(\frac{c}{2}\frac{k_z}{(k_x^2 + k_z^2)^{\frac{1}{2}}}\right) \widehat{\phi}\left(k_x, 0, \frac{c}{2}(k_x^2 + k_z^2)^{\frac{1}{2}}\right) \exp\left[-j\left(k_x x + k_z z\right)\right] dk_x d\omega. \tag{2.25}$$

Chapter 3

Beam Directivity and Wave Scattering

In this chapter, the beam directivity of an incident wave and the wave scattering from a cylindrical void are discussed. The wave source employed in this study is the transducer which generates ultrasound of several hundred kilohertz to several megahertz. On the other hand, explosive wave source are normally used in reflection seismology [4]. These wave sources generate seismic wave of a few hertz to few hundred hertz. The difference between these two applications is the operating frequency range. The beam directivity of a low frequency wave is omni-directional, thus, the directivity of the wave is not normally considered in reflection seismology. Although, the frequency of the waves used in this study is relatively lower than that for steel or other metals, it is high enough to produce a non-uniform directivity. Thus, it is important to take into account the directivity in our analysis. Similar to the beam directivity, In this chapter, directivity of incident wave and scattering wave are described mathematically.

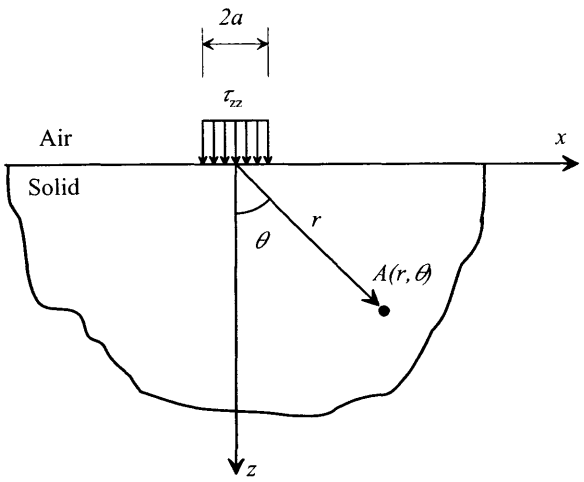

Figure 3-1: The transducer on the surface of half space generates the normal uniform stress.

3.1 Beam directivity of incident wave

Consider a half space loaded by a piston transducer, whose solution is sought by Miller *et al.* [11] and Wooh *et al.* [12]. The first part of this chapter is the review of their paper. Consider a transducer of radius a placed on the surface (Fig. 3-1). The transducer generates the uniform harmonic traction in the direction normal to the surface over the circular area, $\tau_{zz} = T_{zz}e^{j\omega t}$. The equation of motion is

$$(\lambda + 2\mu)\nabla\nabla \cdot \mathbf{u} - \mu\nabla \times \nabla \times \mathbf{u} = \rho\frac{\partial^2 \mathbf{u}}{\partial t^2}. \tag{3.1}$$

where λ, and μ are lamé constants of the medium, ρ is the density of the medium and the symbol $\times$ denotes the cross product. The boundary conditions on the free surface are that

the normal traction

$$T_{zz} = \begin{cases} 1, & |x| \leq a, \\ 0, & |x| > a, \end{cases} \tag{3.2}$$

and shear traction

$$T_{xz} = 0. \tag{3.3}$$

and the displacement field of the P-wave is

$$U_L^a(r,\theta) = \left(\frac{a_t^2}{\mu}\right)\left(\frac{e^{-jk_L r}}{r}\right)\left(\frac{J_1(k_L a \sin\theta)}{k_L a \sin\theta}\right) U_0^l(r,\theta), \tag{3.4}$$

where

$$U_0^l(r,\theta) = \frac{-k_L^2(k_T^2 - 2k_L^2\sin^2\theta)\cos\theta}{G(k_L \sin\theta)},$$

$$G(\zeta) = (2\zeta^2 - k_T^2)^2 - 4\zeta^2\sqrt{(\zeta^2 - k_L^2)(\zeta^2 - k_T^2)},$$

k_L : wave number of longitudinal wave, and

k_T : wave number of shear wave.

Some directivity patterns are obtained for various parameters from the above equation and shown in Figs. (3-2 and 3-3). The 1MHz transducer of 6.35 mm radius and 500kHz transducer of 20.64 mm radius are used in these simulations and the experiments discussed

later. I can be observed from these figures that the waves emitted from a transducer of higher frequency and larger dimension are more directed. In case f:1MHz, a=2.12 mm and aluminum specimen, strong signal propagates to broad area. However, in case f:1MHz, a=6.35 mm and aluminum specimen, the extremely low signal, less than 10% of maximum amplitude, propagates to the area over 30 degrees. For the low frequency transducer (500kHz), the directivity tends to be broader, however, in this case, because of a large dimension, the directivity become narrower.

The directivity restricts the detectable area. If the depth of reflector is 5 cm and the receiver can receive the signal having 30% of maximum amplitude, 1MHz transducer of 6.35 mm radius can detect this reflector while the transducer is within $\pm$2.3 cm from it, while $\pm$5.75 cm for the transducer of 3.18 mm radius. In the case of concrete, the detectable area of transducer is $\pm$2.55 cm for the transducer of 12.70 mm radius and $\pm$1.25 cm for the transducer of 14.29 mm radius.

3.2 Beam scattering from a cylindrical void

Similar to the directivity of incident wave, the distribution of scattering wave is affected by the transducer frequency and the dimension of the scatterer. In this study, scattering P-waves due to an infinitely long cylindrical cavity is discussed. This problem is a review of solution solved by Pao and Mow [13].

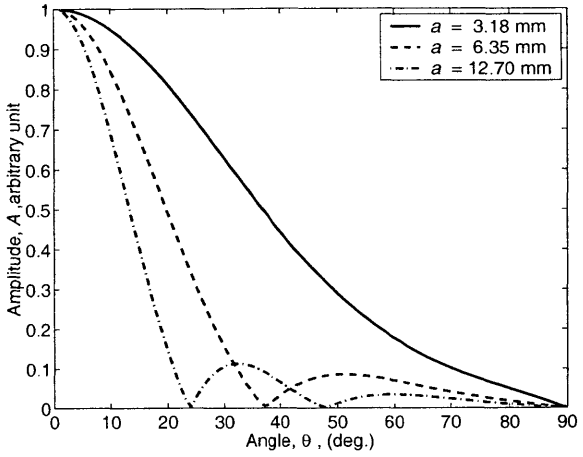

Figure 3-2: Directivity pattern of P-waves in aluminum from a circular piston source of a=6.35 mm radius and f=1MHz.

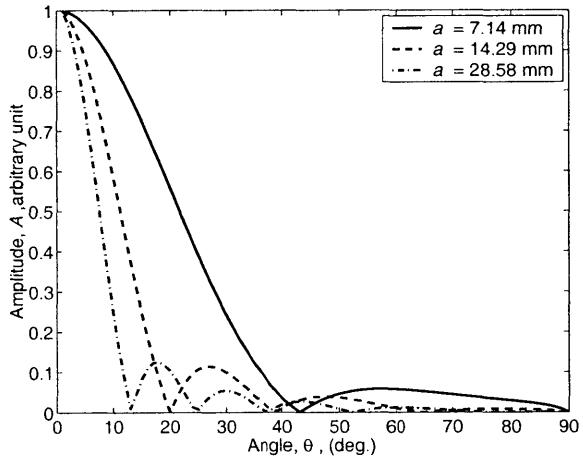

Figure 3-3: Directivity pattern of P-waves in concrete from a circular piston source of a_t=14.29mm and f=500kHz.

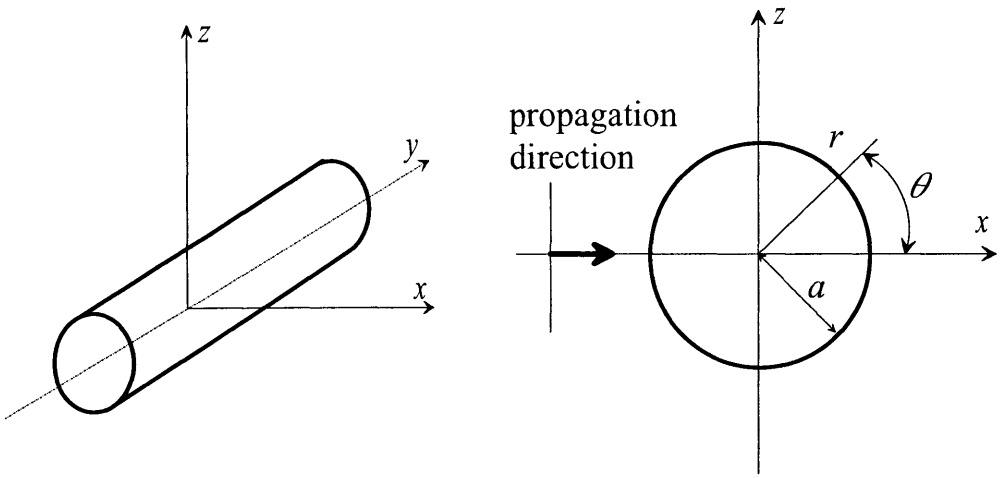

Figure 3-4: P-wave incident on cylindrical cavity.

Consider a plane harmonic P-wave propagating in the x-direction as shown Fig. 3-4.

$$\phi^i = \phi_0 e^{j(k_L x - \omega t)}, \tag{3.5}$$

where the superscript i denotes the incident wave.

When the incident wave strikes the cavity, the two waves are produced:, P- and SV waves, where solutions are of the forms:

$$\phi^r = \sum_{n=0}^{\infty} A_n H_n^1(k_L r)\cos(n\theta)e^{j(k_L x - \omega t)}, \tag{3.6}$$

$$\psi^r = \sum_{n=0}^{\infty} B_n H_n^1(k_T r)\sin(n\theta)e^{j(k_L x - \omega t)}, \tag{3.7}$$

where H_n^1 is the Hankel function of the first kind, A_n and B_n are coefficients of the expansions to be determined from appropriate boundary conditions.

Note that these waves are diverging from the origin. To determine the unknown coefficients, A_n and B_n, the incident wave Eq. (3.5) is rewritten in terms of cylindrical wave function.

$$\phi^i = \phi_0 \sum_{n=0}^{\infty} \epsilon_n (i)^n J_n(k_L r) \cos(n\theta) e^{j(k_L x - \omega t)}, \tag{3.8}$$

where

$$\epsilon_n = \begin{cases} 1 & n = 0, \\ 2 & n \geq 1. \end{cases}$$

The total wave field is

$$\phi = \phi^i + \phi^r, \tag{3.9}$$

$$\psi = \psi^r. \tag{3.10}$$

Traction should be zero on the surface of cavity, i.e.,

$$\sigma_{rr} = \sigma_{r\theta} = 0 \quad \text{at } r = a_c. \tag{3.11}$$

where a_c is th radius of the cavity. These stresses are derived from Eqs. (3.6), (3.7), and (3.8).

$$\sigma_{rr} = \frac{2\mu}{r^2} \sum_{n=0}^{\infty} \left(\epsilon_n j^n \phi_0 \epsilon_{11}^{(1)} + A_n \epsilon_{11}^{(3)} + B_n \epsilon_{12}^{(3)} \right) \cos(n\theta) \Big) e^{-j\omega t}, \tag{3.12}$$

$$\sigma_{r\theta} = \frac{2\mu}{r^2} \sum_{n=0}^{\infty} \left(\epsilon_n j^n \phi_0 \epsilon_{41}^{(1)} + A_n \epsilon_{41}^{(3)} + B_n \epsilon_{42}^{(3)} \right) \sin(n\theta) e^{-j\omega t}, \tag{3.13}$$

$$\sigma_{\theta\theta} = \frac{2\mu}{r^2} \sum_{n=0}^{\infty} \left(\epsilon_n j^n \phi_0 \epsilon_{21}^{(1)} + A_n \epsilon_{21}^{(3)} + B_n \epsilon_{22}^{(3)} \right) \cos(n\theta) e^{-i\omega t}, \tag{3.14}$$

where

$$\epsilon_{11}^{(1)} = \left(n^2 + n - \frac{k_T^2 r2}{2} \right) J_n(k_L r) - k_L r J_{n-1}(k_L),$$

$$\epsilon_{11}^{(3)} = \left(n^2 + n - \frac{k_T^2 r2}{2} \right) H_n^{(1)}(k_L r) - k_L r H_{n-1}^{(1)}(k_L),$$

$$\epsilon_{12}^{(3)} = -n(n+1) H_n^{(1)}(k_T) + k_T r H_{n-1}^{(1)}(k_T).$$

The coefficients A_n and B_n can be determined from Eqs. (3.12), (3.13), and (3.14), and the boundary conditions as

$$A_n = -\epsilon_n j^n \phi_0 \frac{\Delta_n^a}{\Delta_n}, \tag{3.15}$$

$$B_n = -\epsilon_n j^n \phi_0 \frac{\Delta_n^b}{\Delta_n}, \tag{3.16}$$

where

$$\Delta_n^a = \begin{vmatrix} E_{11}^{(1)} & E_{12}^{(3)} \\ E_{41}^{(1)} & E_{42}^{(3)} \end{vmatrix}, \quad \Delta_n^b = \begin{vmatrix} E_{11}^{(3)} & E_{11}^{(1)} \\ E_{41}^{(3)} & E_{41}^{(1)} \end{vmatrix}, \quad \Delta_n = \begin{vmatrix} E_{11}^{(3)} & E_{11}^{(1)} \\ E_{41}^{(3)} & E_{41}^{(1)} \end{vmatrix}.$$

$E_{11}^{(3)} \cdots$, etc., are the value of function, $\epsilon_{11}^{(1)} \cdots$, etc., evaluated at $r = a$.

Substituting A_n and B_n into Eqs. (3.6), (3.7), the scattered P- and SV-wave fields can be obtained. Only the PP-waves are analyzed in this study. Suppose only u_{rr} is measured by receiver, the measured scattered waves as of the form

$$s(r,t) = \sum_{n=0}^{\infty} A_n \frac{\partial \phi}{\partial r}, \tag{3.17}$$

$$= \frac{1}{r} k_L r H_{n-1}^1(k_L r) - n H_n^1(k_L r) \cos(n\theta) e^{j\omega t}. \tag{3.18}$$

Using this function, the directional characteristics of the scattering field at $10a$ away from the center of cavity is calculated and shown in Figs. 3-5, 3-6, 3-7 and 3-8. Similar to the directivity of incident wave, higher frequency or bigger cavity cause well-directed beam. In case f=1MHZ, a_c=1.59mm for aluminum, due to omni-directivity, reflected wave prop-

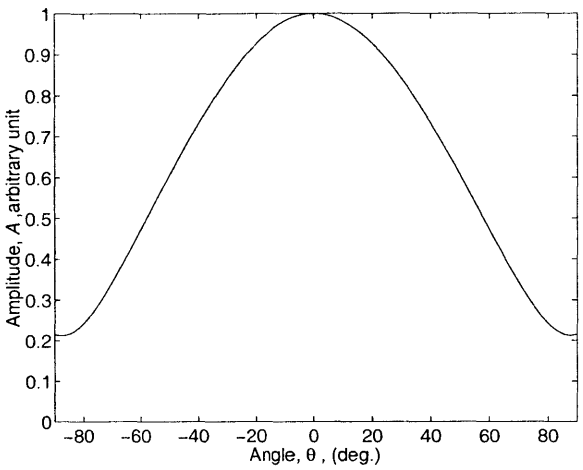

Figure 3-5: Directivity of waves scattered from cylindrical void of a_c=1.59mm for an incident wave of 1 MHz in aluminum.

agates broad area. On the other hand, the wave of 1MHz reflected from cavity of 12.7 mm radius only propagates extremely narrow area, approximately ± 10 degree. For lower frequency, the reflected wave propagate broader area than higher frequency case. However, in the case of larger cavity, a_c=25.4 mm, the beam becomes well-directed.. The angle is determined by the depth of cavity and the distance between transmitter and receiver, and the maximum angle is the angle when the cavity is middle point between transmitter and receiver. Therefore, for the well-directed beam case, reflected wave cannot be measured there.

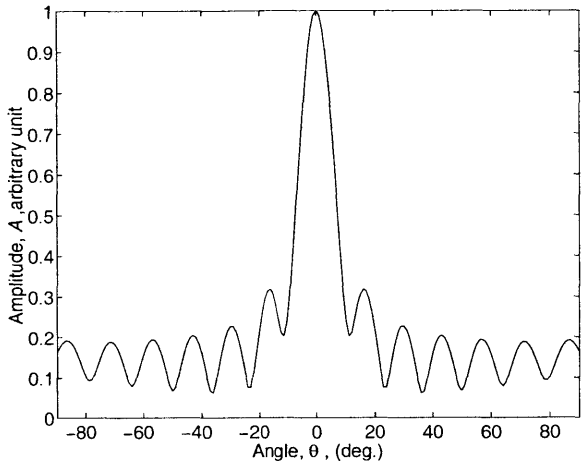

Figure 3-6: Directivity of waves scattered from cylindrical void of a_c=12.70mm for an incident wave of 1 MHz in aluminum.

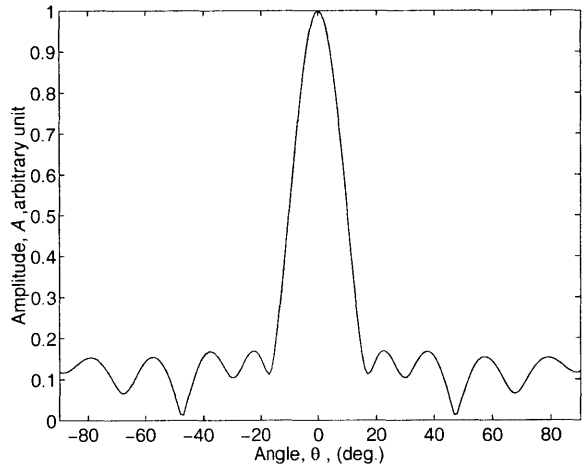

Figure 3-7: Directivity of waves scattered from cylindrical void of a_c=12.70mm for an incident wave of 500kHz in concrete.

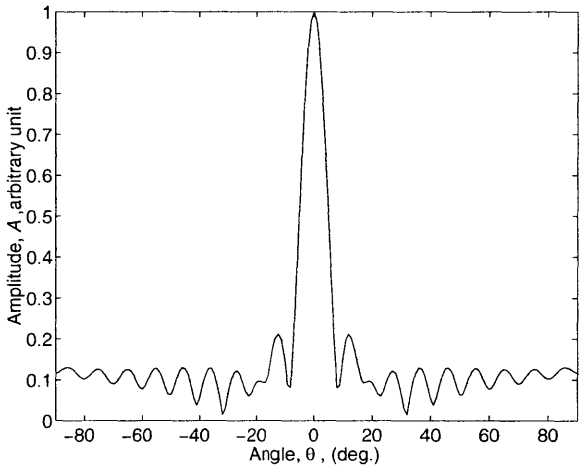

Figure 3-8: Directivity of waves scattered from cylindrical void of a_c=25.40mm for an incident wave of 500kHz in concrete.

Chapter 4

The Effect of Beam Directivity

4.1 Introduction

In the previous chapter, the effects of beam directivity is discussed. To employ reflection seismology to concrete testing, the consideration of the effect of beam directivity is inevitable. In this section, the noise reduction considering directivity and the filter to eliminate the effects of the beam directivity are discussed.

4.2 Noise reduction

One of the main reasons to employ reflection seismology is to improve the signal-to-noise ratio (SNR). As explained earlier, noise in time histories can be divided into two groups:

coherent and incoherent noises. Coherent noises introduced in the process include surface, PS and S-waves, while incoherent is ambient noise.

Since the surface PS- and S-waves propagates at wave speed different velocities from P-waves, coherent noises are canceled after the CMP stacking. Incoherent noise can also be reduced by stacking. However, the degree of noise reduction is different from that of the Earth's subsurface. In this section, the improvement of SNR by stacking of time histories is studied theoretically for both conditions.

4.2.1 Characteristics of noise

Incoherent noises introduced to a reflected wave are assumed to be white and distributed uniformly in range $(-b_1 < y < b_1)$. The mean and variance of the noise in a signal are described as

$$E_1(y) = \frac{\{b_1 + (-b_1)\}}{2} = 0, \tag{4.1}$$

$$V_1(y) = \frac{(b_1 + b_1)^2}{12} = \frac{b_1^2}{3}. \tag{4.2}$$

If the distributions of noise are identical for all the signals, the mean and variance of the two summed signals are

$$E_2(y) = E_1(y) + E_1(y) = 0, \tag{4.3}$$

$$V_2(y) = V_1(y) + V_1(y) = \frac{2b_1^2}{3}. \tag{4.4}$$

As the distribution is not changed by adding the signals with identical distributions, the maximum value ($-b_2 < y \leq b_2$) remains the same, i.e., $b_2 = b_1\sqrt{2}$ and for a signal constructed by adding n time histories, $-b_n < y \leq b_n$, $b_n = b_1\sqrt{n}$.

4.2.2 Improvement of SNR used in geophysical surveys

Previously we assumed that

1. The maximum amplitude of reflected wave, measured by pulse-echo testing is a_0.

2. The offset-depth ratio d/h is so small and the frequency of the incident wave is so low that the beam directivity does not play a significant role; i.e., the wave source are considered to produce spherical waves and the maximum amplitude of each reflected wave is identical: $f_{i,max} = a_0$.

The SNR of each signal is then defined as a_0/b. After summing n time histories, the SNR becomes

$$\frac{na_0}{\sqrt{n}b} = \sqrt{n}\frac{a_0}{b}. \tag{4.5}$$

Therefore, the SNR can be improved by a factor of $\sqrt{n}$ by adding n time histories. Furthermore, the improvement of SNR is independent of the offset value.

4.2.3 Improvement of SNR for concrete testing

In our work for evaluating concrete, the

1. The maximum amplitude of reflected wave, which is measured by Pulse echo testing, is a_0.

2. In our case, the d/h ratio is not small and the frequency of the incident wave is not so low. Thus, directivity should be considered; i.e. maximum amplitude of each reflected wave depends on offset value.

3. We only consider the propagation of P-waves.

4. The directivity is calculated based on the model discussed at Chapter 3.

The maximum amplitude of P-wave at a point (r, θ, t) is given by the directivity function

$$U_a^L(r,\theta,t) = \frac{a^2 b}{\mu} \frac{J_1(k_L a \sin\theta)}{k_L a \sin\theta} \left(\frac{e^{-jk_L r}}{r}\right) U_0^L(\theta) f\left(t - \frac{r}{c_L}\right). \tag{4.6}$$

where

$$U_0^l(r,\theta) = \frac{-k_L^2(k_T^2 - 2k_L^2\sin^2\theta)\cos\theta}{G(k_L\sin\theta)},$$

$$G(\zeta) = (2\zeta^2 - k_T^2)^2 - 4\zeta^2\sqrt{(\zeta^2 - k_L^2)(\zeta^2 - k_T^2)},$$

$$\theta = \text{atan}\left(\frac{d}{2h}\right),$$

k_L : wave number of longitudinal wave, and

k_T : wave number of shear wave.

Since the receiver is located at distance, d, from the transmitter, the incident wave is reflected at the middle point between the transmitter and the receiver. Thus, the reflected wave arrived at receiver obliquely. Suppose the reflector is located at the depth z_a and the cosine term of the reflected wave is recorded by the receiver. The maximum amplitude at the point on the surface $A_i(x_i, 0, t = t_i)$ is

$$A_i(d_i, 0, t_i) = U_a^L(d_i, z_a, t_i)\cos\left(\frac{ct_i}{\sqrt{ct_i^2 - (d_i/2)^2}}\right), \tag{4.7}$$

where, d_i is the offset of the ith receiver and t_i is the travel time of the wave reflected off the reflector located at z_a. Before the time histories are added, each time history is compensated by NMO process described in Chapter 2 from t_i to t_0. Then, the SNR can be

expressed.

$$\text{SNR} = \frac{\sum_{i=1}^{n} A_i(x_i, 0, t_0)}{\sqrt{n}b}. \tag{4.8}$$

Since the maximum amplitude of the reflected wave is a_0, we have the condition that

$$A_0(0, 0, t_0) = a_0. \tag{4.9}$$

a_0 is rewritten by U_0^l described in Chapter 3,

$$a_0 = U_0^l(r, 0) = \frac{-k_L^2 k_T^2}{2k_L^2 - k_T^2}, \tag{4.10}$$

Then, the SNR of the pulse-echo signals becomes

$$\text{SNR} = \frac{A_0(0, 0, t_0)}{b}. \tag{4.11}$$

Now, the ratio of the SNR between of the pulse-echo method and of the reflection seismology is defined.

$$\xi = \frac{\sum_{i=1}^{n} A_i(x_i, 0, t_0)}{A_0(0, 0, t_0\sqrt{n})}. \tag{4.12}$$

Table 4.1: Parameters used in this study

Parameter	Aluminum	Concrete
Center frequency	1 MHz	500 kHz
Sampling frequency	25 MHz	10 MHz
Radius of transducer	6.35 mm	14.29 mm
P-wave speed	6230 m/s	4000 m/s
S-wave speed	3130 m/s	2450 m/s
Density	2.7 g/cm^3	2.3 g/cm^3

In order to improve the SNR above that of pulse-echo testing, it should be satisfied that

$$\xi > 1. \tag{4.13}$$

In the following (Fig. 4-2– 4-8), we will study the influence of the offset, depth of reflector and number of receivers on the SNR for aluminum and concrete. The parameter used in this study is shown in table‘4.1. As described in Chapter 3, The beam in aluminum that is generated by 1MHz transducer of 6.35 mm radius is well-directed and one side lobe is observed in the directivity pattern (Fig. 4-1).

Figure 4-2 shows the relationship between minimum offset of the array and ξ of equation 4.12. The depth of cavity is 29.5 mm, and the number of receivers that consist array is changed as 6, 12, 24 and 48. Due to well-directed beam and the big offset-depth ratio, the only weak signal can be received at far offset receivers. Thus, clear difference among the SNR of the arrays with 12, 24 and 48 receivers is not observed. When ξ is greater than

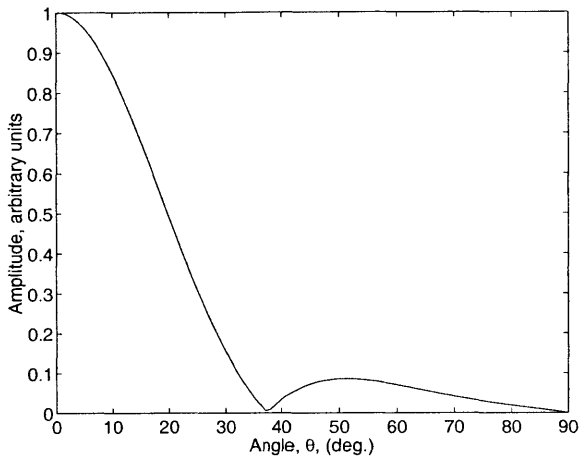

Figure 4-1: Directivity pattern of P-waves in aluminum from a circular piston source of a=6.35 mm radius and f=1MHz. See Chapter 3.

1, the SNR of reflection seismology is better than it of pulse-echo testing. In this case, in order to make ξ greater than 1, the minimum offset should be the value less than 20 mm.

The relationship between minimum offset of the array and ξ in the deep cavity case (z_a = 59.0 mm) is shown in figure 4-3. Due to the small offset-depth ratio, the signals received at the far offset receivers are stronger than it of the shallow cavity case. The good SNR can be obtained even the arrays with larger offset and, in this case, the SNR of the large number of receivers case is much better than small number of receivers case.

Figure 4-4 shows the influence of reflector location on the SNR for the offset of 28.6 mm and the receiver spacing of 0.80 mm. As shown in the figure, the SNR is better than it of pulse-echo testing when a reflector is located deeper than 40 mm. The SNR of the reflected wave off the shallow cavity is not improved by increasing the number of receivers,

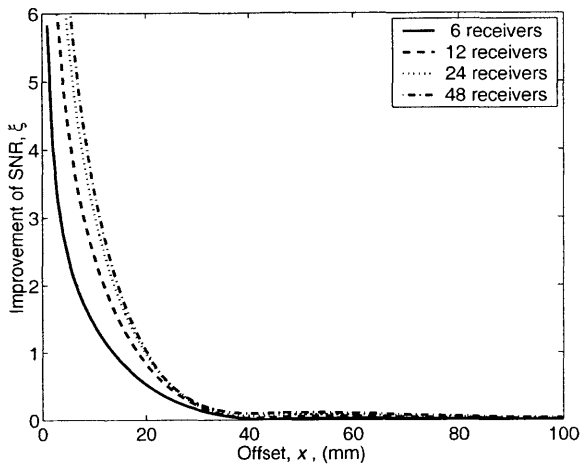

Figure 4-2: Improvement of the SNR, ξ vs. change of the offset. The depth of reflector is 29.5mm. aluminum case

however in the case of deep cavity, the SNR of the reflected wave is increased by increasing the number of receivers.

The directivity pattern of P-waves in concrete by 500 kHz transducer of 14.29 mm radius is shown in figure 4-5. In testing concrete, since the beam concentrate very narrow area, the reflected wave cannot be observed at the area of big offset-depth ratio. Therefore, it is very difficult to improve the SNR of the reflected wave off the shallow cavity. When reflector is located below a depth of 80 mm, the SNR become better than it of pulse-echo testing.

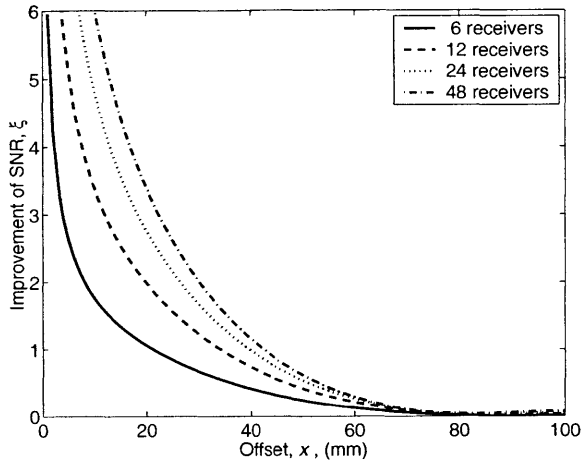

Figure 4-3: Improvement of the SNR, ξ vs. change of the distance between receivers. The depth of reflector is 59.0 mm. aluminum case.

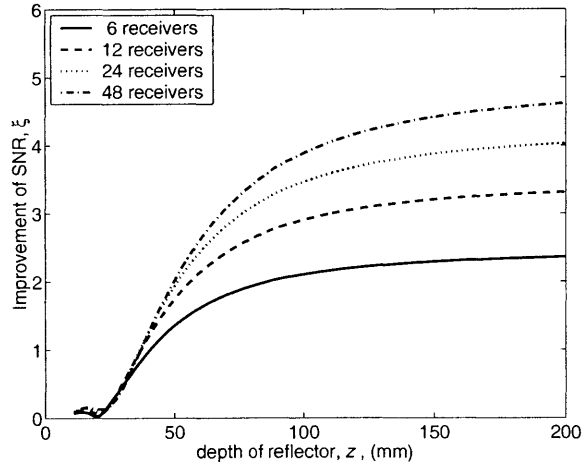

Figure 4-4: Improvement of the SNR, ξ vs. change of the depth of reflector. The offset is 28.6 mm and the distance between receivers is 0.80 mm. aluminum case.

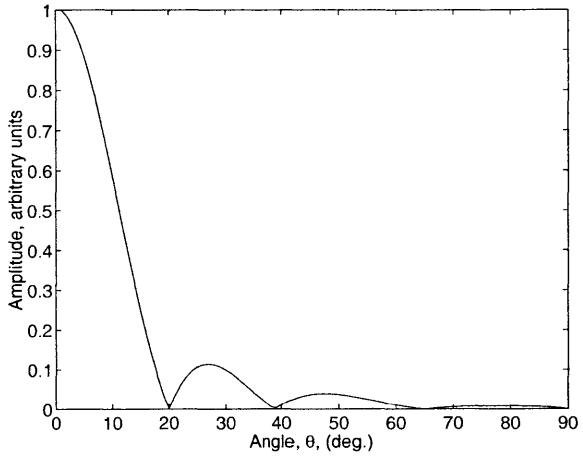

Figure 4-5: Directivity pattern of P-waves in concrete from a circular piston source of a_t=14.29mm and f=500kHz.

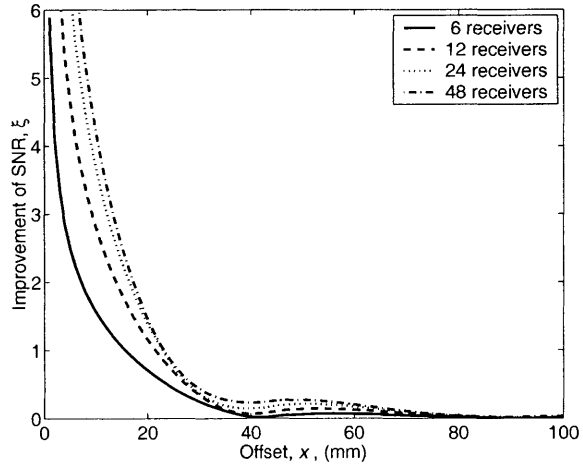

Figure 4-6: Improvement of the SNR, ξ vs. the change of the distance between receivers. The depth of the reflector is 60.4 mm, concrete case.

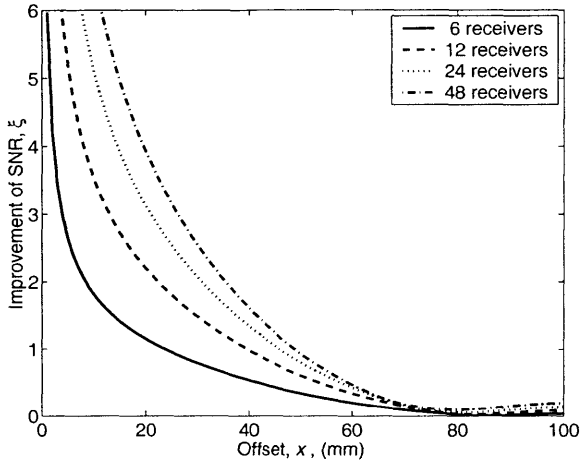

Figure 4-7: Improvement of the SNR, ξ vs. change of the distance between receivers. The depth of the reflector is 120.7 mm, concrete case.

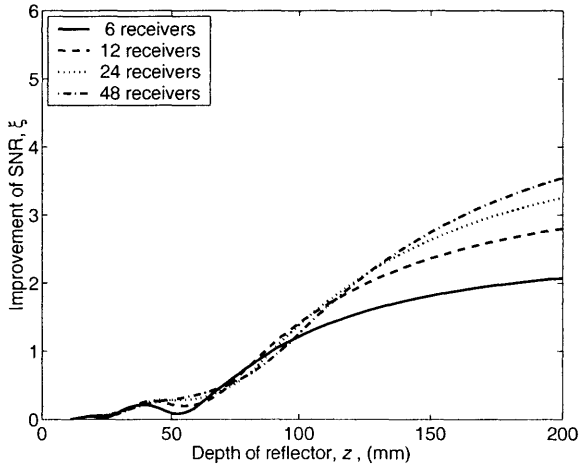

Figure 4-8: Improvement of the SNR, ξ vs. the change of the depth of the reflector. the offset is 34.9 mm, the distance between transducers is 1.59 mm, concrete case.

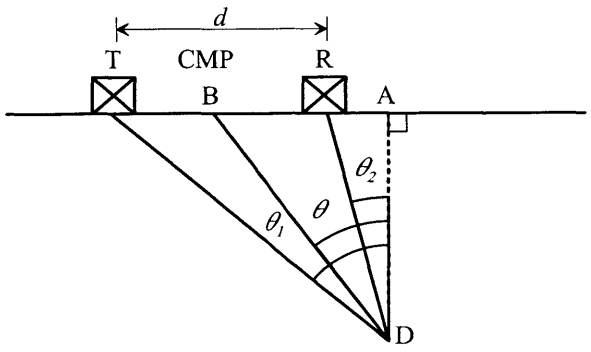

Figure 4-9: The geometric relations among $\cos\theta$, $\cos\theta_1$ and $\cos\theta_2$

4.3 Filtering to eliminate the effect of directivity

Beam directivity could greatly distort the images under the certain conditions. An inverse filter is developed to eliminate the effects of directivity. This filtering process is carried out in the frequency domain. The signal obtained at the CMP is

$$s(x,0,t) = U_L^a(r,\theta_1)\phi(x,0,t)\cos(\theta_2), \tag{4.14}$$

where $U_L^a(r,\theta_1)$ is the directivity function discussed in Chapter 3, and $\phi(x,0,t)$ is the compressional wave field. With the geometrical relation illustrated in figure 4-9, $\cos\theta_1$ and $\cos\theta_2$ are rewritten in terms of $\cos\theta$ and $\sin\theta$ as follows:

$$\cos\theta_1 = \frac{c/2t_0\cos\theta}{\sqrt{(c/2t_0\sin\theta + d/2)^2 - (c/2t_0\cos\theta)^2}}, \tag{4.15}$$

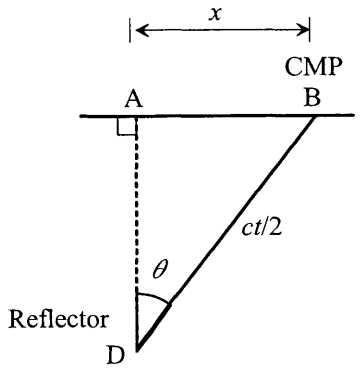

Figure 4-10: The geometric relations among $\cos\theta$, t_0 and x

$$\cos\theta_2 = \frac{c/2t_0\cos\theta}{\sqrt{(c/2t_0\sin\theta - d/2)^2 - (c/2t_0\cos\theta)^2}}, \tag{4.16}$$

where t_0 is the time scale of the zero-offset data. From Fig. 4-10, the relationship between θ, t_0 and d is

$$t_0 = \frac{2x\sin\theta}{c}. \tag{4.17}$$

Differentiating Eq. (4.17) with respect to x,

$$\frac{dt_0}{dx} = \frac{2\sin\theta}{c}. \tag{4.18}$$

In the k_x-f domain, dt_0/dx can be described as

$$\frac{dt_0}{dx} = \frac{k_x}{\omega_0}. \tag{4.19}$$

Substituting Eq. (4.19) into (4.18), we obtain

$$\frac{2\sin\theta}{c} = \frac{k_x}{\omega_0}. \tag{4.20}$$

The travel time of the reflected wave is compensated by the NMO discussed in Chapter 2. It can compensate for the travel time perfectly when the reflector is a flat crack or a cavity located under the CMP. However the reflector is an inclined crack or a cavity that is not loaded under the CMP, the NMO could cause a small error. In order to compensate for this error, Dip-Moveout (DMO) is used [14]. DMO is usually used for compensation of the signal off the dipped reflector, however, in this study, it is also employed to make a clear image of the cavity.

Referring to the Fig. 4-9, the measured travel time is described as

$$t = \sqrt{t_0^2 + \frac{d^2\cos^2\theta}{c^2}}, \tag{4.21}$$

where t_0 is the zero-offset travel time. It is rewritten as

$$t = \sqrt{t_0^2 + \frac{d^2}{c^2} - \frac{d^2\sin^2\theta}{c^2}}. \tag{4.22}$$

The travel time compensated by the NMO is

$$t_n = \sqrt{t^2 - \frac{d^2}{c^2}}. \tag{4.23}$$

Thus, the travel time compensated by the NMO is described by zero-offset travel time.

$$t_n = \sqrt{t_0^2 - \frac{d^2 \sin^2\theta}{c^2}}. \tag{4.24}$$

Its differentials is

$$A = \frac{dt_n}{dt_0} = \frac{t_n}{t_0} = \sqrt{1 + \frac{4sin^2\theta}{c^2}\frac{d^2}{4t_n^2}}. \tag{4.25}$$

Now, the travel time compensated by the NMO is used for the filtering. The compensated signal is rewritten as

$$s(d, 0, t_n) = U_L^a(r, \theta_1)\phi(d, 0, t_n)\cos(\theta_2). \tag{4.26}$$

From Eqs (4.15), (4.16), (4.20),(4.24) and (4.26), and considering $r = ct_0/2$, the two-dimensional Fourier transform of the compressional wave field at the CMP is described as a function of t_0, ω_0, and k_x.

$$\widehat{s}(k_x, 0, \omega_0) = \int_{-\infty}^{\infty}\int_{-\infty}^{\infty} U_L^a(t_0, \omega_0, k_x)\phi(k_x, 0, t_0)\cos[\theta_2(t, \omega, k_x)]e^{i\omega_0 t}e^{-ik_x x}dt_0 dk_x, \tag{4.27}$$

Table 4.2: The parameters used in the simulation

Material	Aluminum	Concrete
Center frequency	1 MHz	500 kHz
Sampling frequency	25 MHz	10 MHz
Radius of the transducer	6.35 mm	14.29 mm
Offset	28.6 mm	60.33 mm
Bandwidth	500 kHz	500 kHz
Spatial sampling rate	0.80 mm	1.59 mm
Depth of the cavity	29.5 mm	60.33 mm

By substituting Eq. (4.24) and (4.25) into Eq. (4.27) is replaced by t_n

$$\widehat{s}(k_x, 0, \omega_0) = \int_{-\infty}^{\infty}\int_{-\infty}^{\infty} \frac{1}{A} U_L^a(t_n, \omega_0, k_x)\widehat{\phi}(k_x, 0, t_n)\cos[\theta_2(t, \omega_0, k_x)]e^{i\omega_0 t_n A}e^{-ik_x x}dt_n dx. \tag{4.28}$$

The filtered diffraction curve is obtained by the two dimensional inverse Fourier transform of Eq.(4.28).

$$s(x, 0, t_0) = \left(\frac{1}{2\pi}\right)^2 \int_{-\infty}^{\infty}\int_{-\infty}^{\infty} \widehat{s}(k_x, 0, \omega_0)e^{i\omega_0 t_0}e^{-ik_x x}d\omega_0 dk_x \tag{4.29}$$

An examples is shown below for the parameter tabulated in Table 4.2.

The images of a cavity obtained without filtering and with filtering are shown in Figs 4-11 and 4-12. The cavity becomes smaller and it is plotted at its exact location in Fig. 4-12.

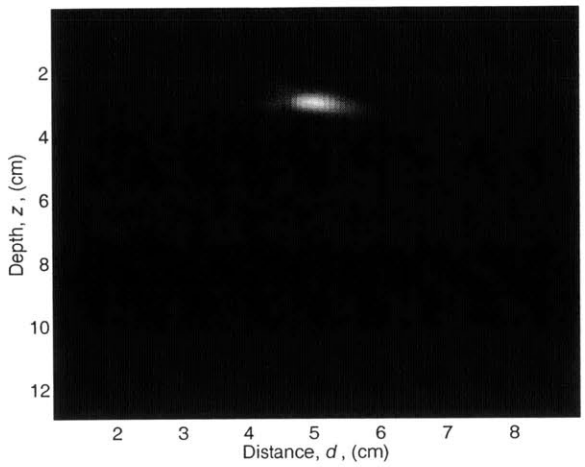

Figure 4-11: The image of the cavity in aluminum without filtering.

In the case of concrete, however, the distortion of the image is worse than it of the aluminum case, the image of the cavity becomes smaller and is plotted at the exact position (Fig. 4-13 and 4-14).

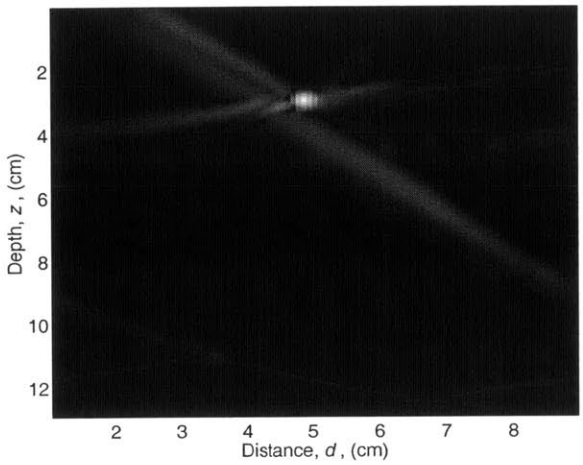

Figure 4-12: The image of the cavity in aluminum after filtering.

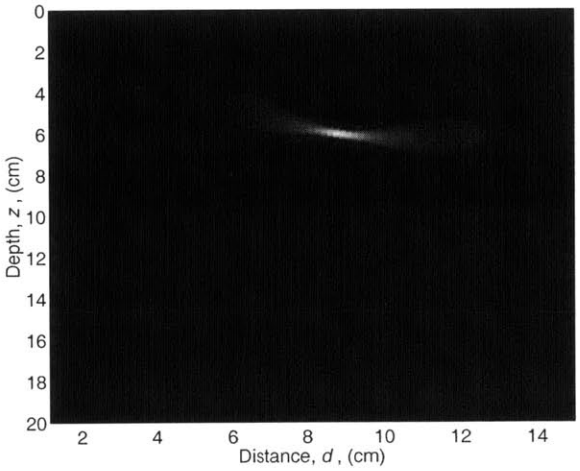

Figure 4-13: The image of the cavity in concrete without filtering. The image is shifted to the right.

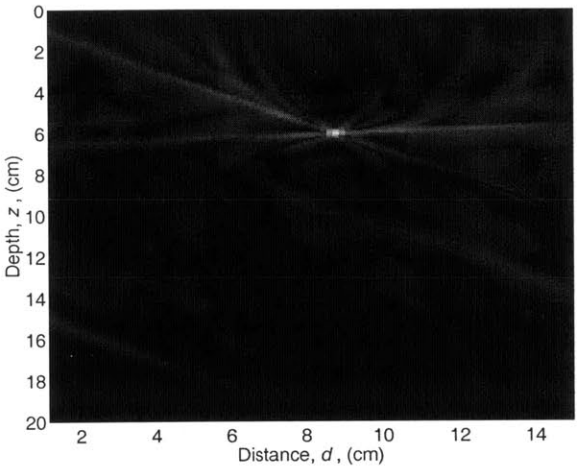

Figure 4-14: The image of the cavity in concrete after filtering. The image is shown at actual position.

Chapter 5

Simulation

5.1 Introduction

The simulation results are discussed in this chapter. The simulation studies are carried out using three models: the point source, the directivity, and the scattering models. The point source model simulates zero offset data, in which the directivity of incident wave and the scattering wave are not considered. The directivity model is a realistic model for concrete testing. In this model, the directivity of incident wave is considered. The scattering model is the most accurate one in these three models, which takes into account the directivity of the scattered wave in addition to the directivity of incident wave.

Table 5.1: Parameters used in the simulation studies

Parameter	Aluminum	Concrete
Center frequency	1 MHz	500 kHz
Sampling frequency	25 MHz	10 MHz
P-wave speed	6230 m/s	4000 m/s
S-wave speed	3130 m/s	2450 m/s
Offset	28.6 mm	34.9 mm
Density	2.7 g/cm^3	2.3 g/cm^3

5.2 The parameters used in the simulations

In these simulation studies, the following parameters are varied: bandwidth, sampling rate, depth of the reflector, the radius of transducer, and the radius of the cavity. These parameters are tabulated in table 5.1.

5.3 The point source model

Simulations studies for the point source model are carried out. In this model, the wave directivity is neglected, i.e., the wave source is considered as a point source generating spherical waves (Fig. 5-1).

For a reflector located at the depth z, and the incident wave, $f(0,t)$, measured signal $s(x,t)$ can be written as

$$s(x,t) = \frac{1}{r} f\left(0, t - \frac{r}{c_L}\right), \tag{5.1}$$

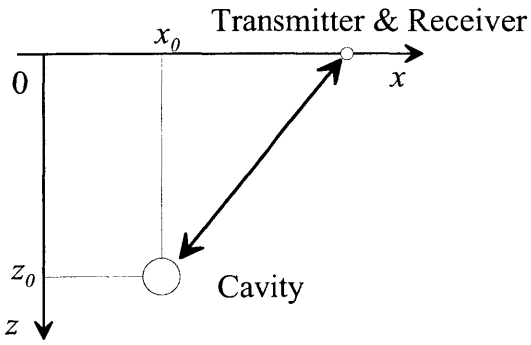

Figure 5-1: The transmitter is assumed to be a point source.

Table 5.2: The parameters used in the simulation (the point source model in aluminum) See figure 5-1

Case	bandwidth	spatial sampling ratio	location of the cavity (x_0,z_0)
1-1-1	500 kHz	0.80 mm	(50, 29.50) mm
1-2-1	100 kHz	0.80 mm	(50, 29.50) mm
1-2-2	1 MHz	0.80 mm	(50, 29.50) mm
1-3-1	500 kHz	3.99 mm	(50, 29.50) mm
1-3-2	500 kHz	0.16 mm	(50, 29.50) mm
1-4-1	500 kHz	0.80 mm	(50, 9.83) mm
1-4-2	500 kHz	0.80 mm	(50, 88.50) mm

where $r = \sqrt{(x - x_0)^2 + 4z_0^2}$.

5.3.1 The cavity case

Aluminum specimen

In order to investigate the effects of the parameters, bandwidth, spatial sampling rate and the depth of the cavity are varied (Table 5.2), and results are shown in Figs. 5-2 to 5-13.

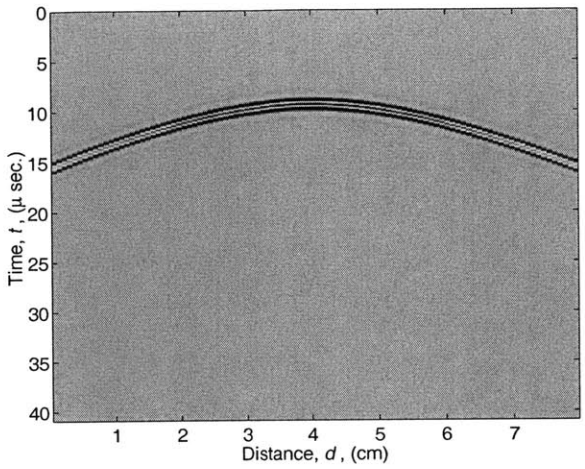

Figure 5-2: Case 1-1-1: the diffraction hyperbola obtained by the point source model, bandwidth: 500 kHz, spatial sampling rate: 0.80 mm, depth of cavity: 29.50m.

The reflected waves measured at each CMP on the surface are plotted in the x-t domain in Fig. 5-2. In this domain, the amplitude of the reflected wave is indicated as the pixel array values, where the arrival time of the reflected wave at x appears can be described as a hyperbolic function of x and the cavity depth, z. Thus, this curve is called "diffraction hyperbola". Since the beam directivity is not considered in this model, the amplitude of the reflected waves is symmetry about the apex of the diffraction curve. This diffraction curve is transformed from x-t domain to k_x-ω domain using two dimensional Fourier transform. Then, they geometrically transformed from the k_x-ω domain to the k_x-k_z domain. At last, Inverse Fourier transform is carried out over both k_x and k_z and the image of the cavity is obtained (Fig. 5-3).

Figure 5-4 shows the effect of bandwidth. The size of cavity created using a narrow bandwidth signal appears bigger than that for a broadband signal. The reason is following:

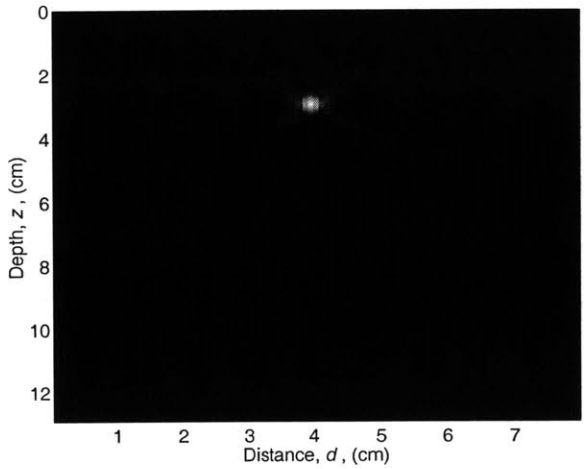

Figure 5-3: Case 1-1-1: the image of the cavity in aluminum obtained by the point source model, bandwidth: 500 kHz, spatial sampling rate: 0.80 mm, depth of cavity: 29.50 mm

The wave of narrow bandwidth in frequency domain generates wide signals in time domain. The same effect occurs in migration in transforming from the k_x-k_z domain to the x-z domain. By contrast, the cavity using a broad band signal is smaller and clearer as shown in Fig. 5-5. From these results, it can be observed that the bandwidth controls the temporal resolution. The wider the bandwidth is the better the spatial resolution.

Next, the spatial sampling rate is varied (Fig. 5-3 and 5-6 to 5-9). A coarse spatial sampling rate results in poor horizontal resolution as well as the spatial aliasing effect. The spatial aliasing is clearly observed in the k_x-ω domain (Fig. 5-6). The spatial aliasing is a phenomenon equivalent to the temporal aliasing, but in space, caused by the coarse spatial sampling rate. In the other two cases, Case 1-1-1 and Case 1-2-2, spatial aliasing does not arise (Fig. 5-7).

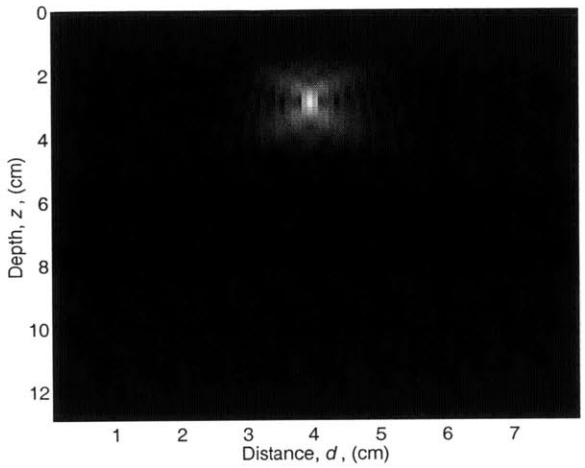

Figure 5-4: Case 1-2-1: the image of the cavity in aluminum obtained by the point source model, bandwidth: 100 kHz, spatial sampling rate: 0.80 mm, depth of cavity: 29.50 mm

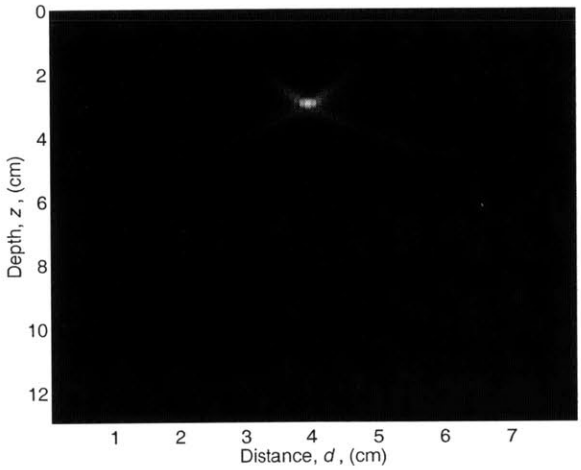

Figure 5-5: Case 1-2-2: the image of the cavity in aluminum obtained by the point source model, bandwidth: 1 MHz, spatial sampling rate: 0.80 mm, depth of cavity: 29.50 mm

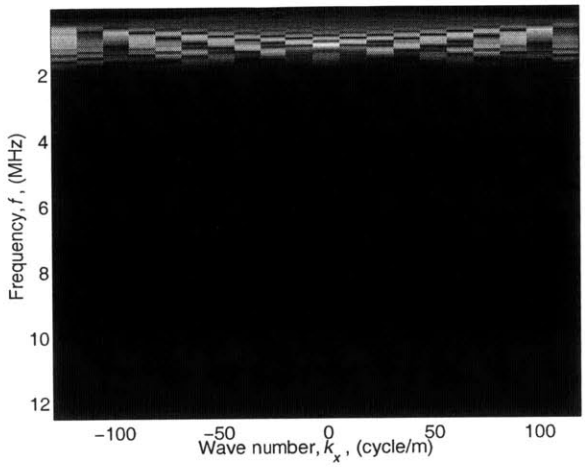

Figure 5-6: Case 1-3-1: the transformed diffraction hyperbola in the k_x-ω domain by the point source model, bandwidth: 500 kHz, spatial sampling rate: 3.99 mm, depth of cavity: 29.50 mm spatial aliasing is seen in this figure.

The image for Case 1-3-2 is clearer than the image in Case 1-1-1, but the number of data in Case 1-3-2 is five times as much as that of Case 1-1-1. Therefore, the cost for data acquisition and computation is much greater than that of Case 1-1-1.

The depth of cavity is varied (Fig. 5-10 to 5-13). The shape of diffraction hyperbola is determined by the cavity depth as well. The gradient of diffraction hyperbola for deeper cavity is lower than that of a closer cavity, approaching a straight line as $z \rightarrow \infty$ and it becomes closer to the straight line (Fig. 5-11). Consequently, it becomes more difficult to construct clear images for deeper cavities (Fig. 5-12). In order to solve this problem, the frequency resolution is improved by adding zeros to the measured waveform. As shown in Fig. 5-13, a better image is obtained, although it is bigger than that of a close cavity.

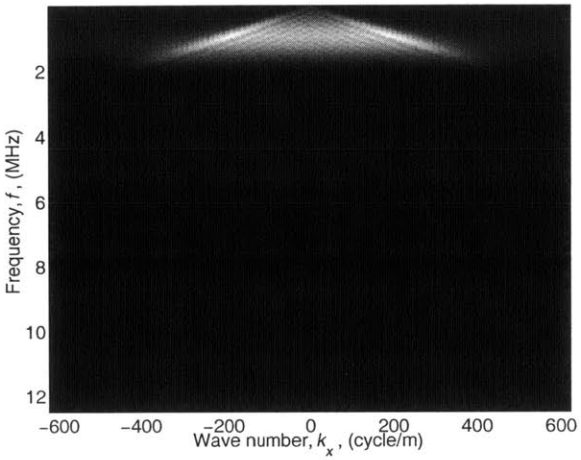

Figure 5-7: Case 1-1-1: the transformed diffraction hyperbola in the k_x-ω domain by the point source model, bandwidth: 500 kHz, spatial sampling rate: 0.80 mm, depth of cavity: 29.50 mm spatial aliasing is not seen in this figure.

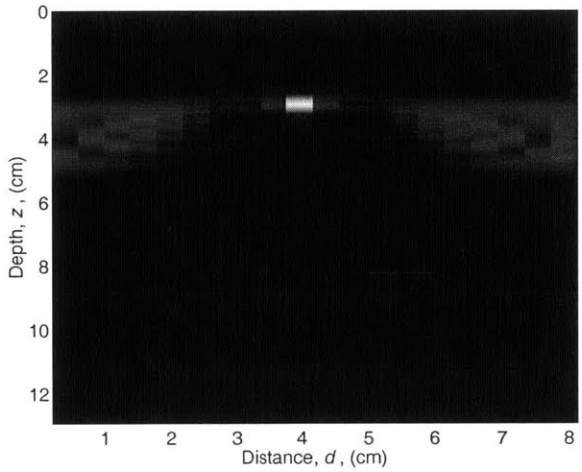

Figure 5-8: Case 1-3-1: the image of the cavity in aluminum obtained by the point source model, bandwidth: 500 kHz, spatial sampling rate: 3.99 mm, depth of cavity: 29.50 mm

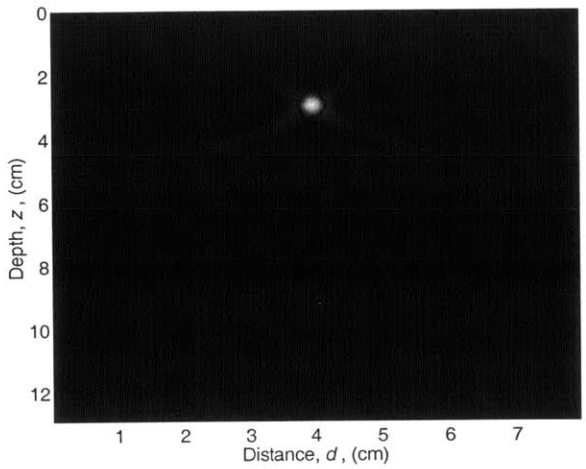

Figure 5-9: Case 1-3-2: the image of the cavity in aluminum obtained by the point source model in aluminum, bandwidth: 500 kHz, spatial sampling rate: 0.16 mm, depth of cavity: 29.50 mm

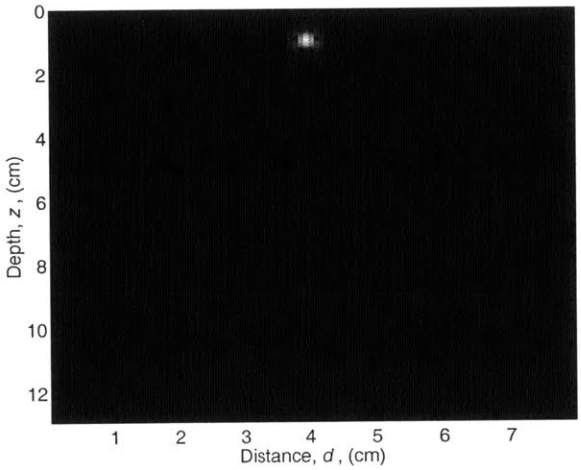

Figure 5-10: Case 1-4-1: the image of the cavity in aluminum obtained by the point source model, bandwidth: 500 kHz, spatial sampling rate: 0.80 mm, depth of cavity: 9.83 mm.

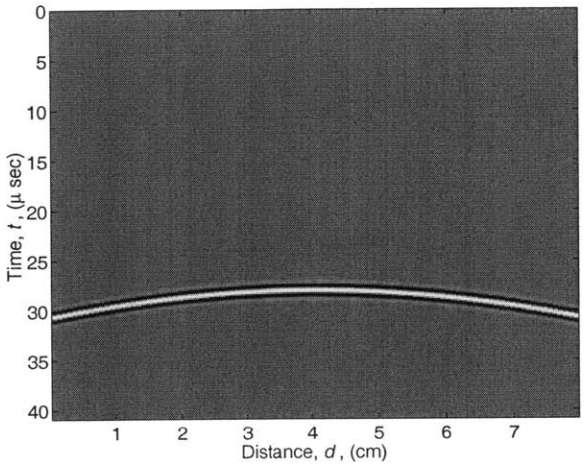

Figure 5-11: Case 1-4-2: the diffraction curve obtained by the point source model in aluminum, bandwidth: 500 kHz, spatial sampling rate: 0.80 mm, depth of cavity: 88.50 mm. The gradient of diffraction curve is lower than that of shallow case (Fig. 5-2).

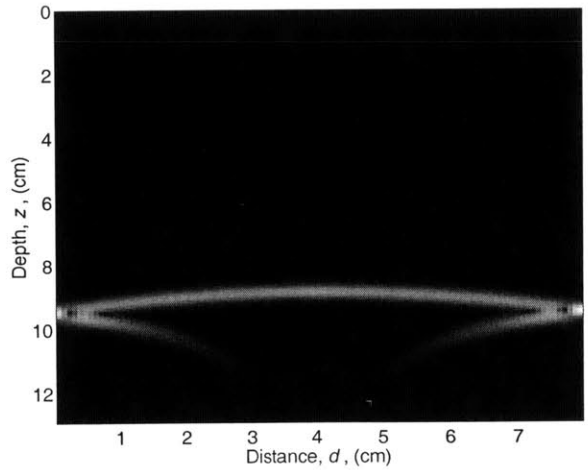

Figure 5-12: Case 1-4-2: the image of the cavity in aluminum obtained by the point source model with lower temporal frequency resolution, bandwidth: 500 kHz, spatial sampling rate: 0.80 mm, depth of cavity: 88.50 mm.

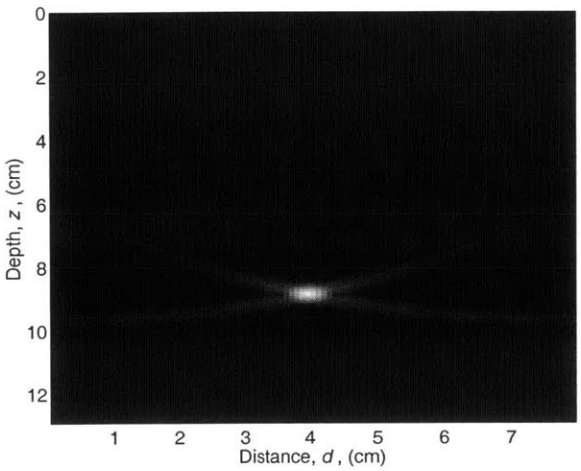

Figure 5-13: Case 1-4-2: the image of the cavity in aluminum obtained by the point source model with higher temporal frequency resolution, bandwidth: 500 kHz, spatial sampling rate: 0.80 mm, depth of cavity: 88.50 mm

Concrete specimen

The parameters used in the simulation study for concrete are shown in Table 5.3 and the simulation results are shown in Fig 5-14 to. 5-20. The only difference between the aluminum specimen and concrete model is the wavespeed in the medium. As the wavespeed decreases, the gradient of diffraction curve becomes steeper. This is preferable to construct clear image. As same as aluminum case, clear images are obtained except for the narrow bandwidth signals and coarse sampling rate.

5.3.2 crack

The simulation study is extended to cracks. It is assumed that cracks consist of infinitely many point reflectors (Fig. 5-21). The crack is inclined at 14.0 degrees and the length of

Table 5.3: The parameters used in the simulation for concrete specimen (the point source model)

Case	bandwidth	spatial sampling ratio	location of the cavity (x_0, z_0)
2-1-1	100 kHz	1.59 mm	(80, 60.33) mm
2-2-1	500 kHz	1.59 mm	(80, 60.33) mm
2-2-2	1 MHz	1.59 mm	(80, 60.33) mm
2-3-1	500 kHz	7.95 mm	(80, 60.33) mm
2-3-2	500 kHz	0.32 mm	(80, 60.33) mm
2-4-1	500 kHz	1.59 mm	(80, 20.11) mm
2-4-2	500 kHz	1.59 mm	(80, 180.98) mm

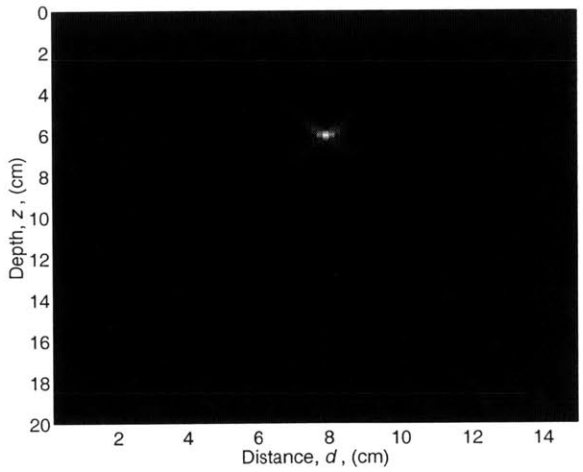

Figure 5-14: Case 2-1-1: The image of the cavity in concrete obtained by the point source model, bandwidth: 500 kHz, spatial sampling rate: 1.59 mm, depth of cavity: 60.33 mm

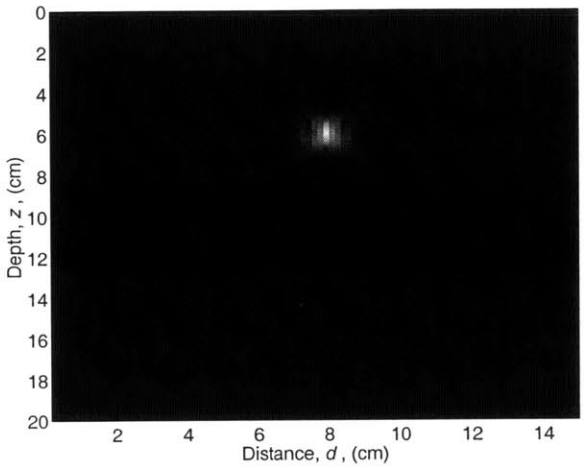

Figure 5-15: Case 2-2-1: The image of the cavity in concrete obtained by the point source model, bandwidth: 20 kHz, spatial sampling rate: 1.59 mm, depth of cavity: 60.33 mm

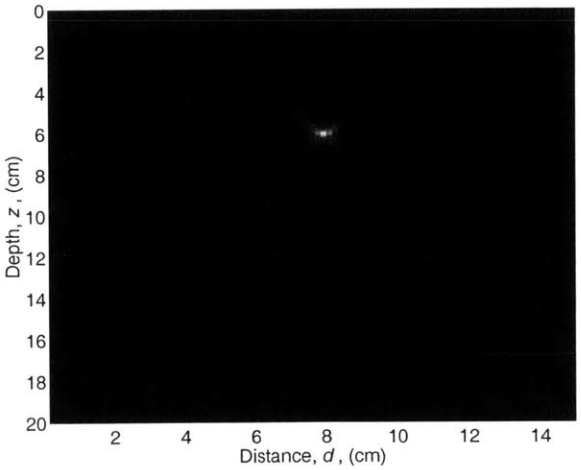

Figure 5-16: Case 2-2-2: The image of the cavity in concrete obtained by the point source model, bandwidth: 500 kHz, spatial sampling rate: 1.59 mm, depth of cavity: 60.33 mm

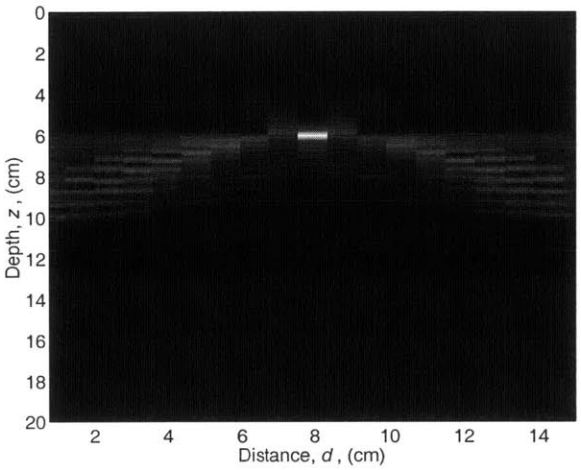

Figure 5-17: Case 2-3-1: The image of the cavity in concrete obtained by the point source model, bandwidth: 500 kHz, spatial sampling rate: 7.95 mm, depth of cavity: 60.33 mm

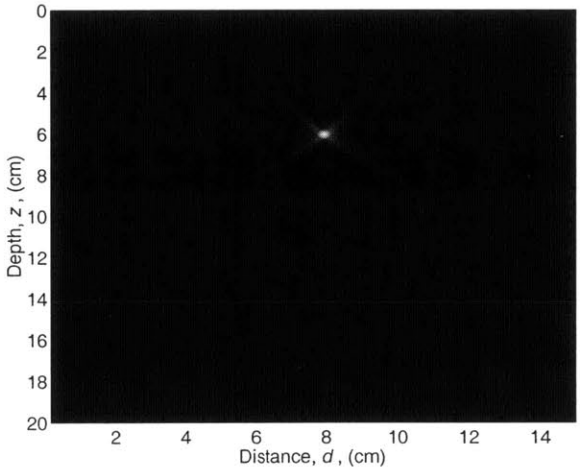

Figure 5-18: Case 2-3-2: The image of the cavity in concrete obtained by the point source model, bandwidth: 500 kHz, spatial sampling rate: 0.32 mm, depth of cavity: 60.33 mm

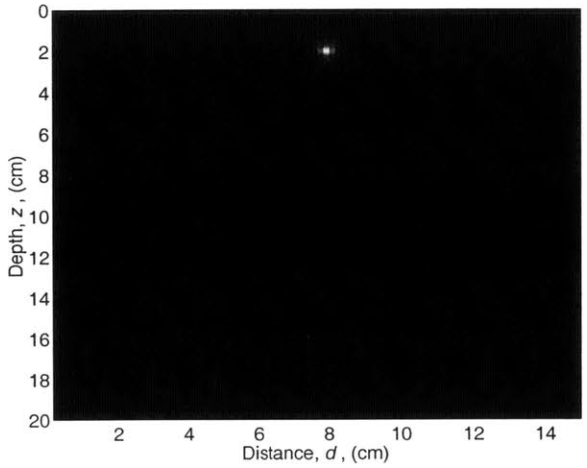

Figure 5-19: Case 2-4-1: The image of the cavity in concrete obtained by the point source model, bandwidth: 500 kHz, spatial sampling rate: 1.59 mm, depth of cavity: 20.11 mm

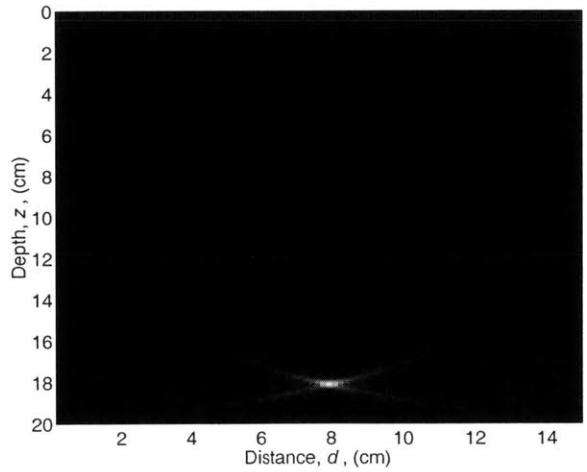

Figure 5-20: Case 2-4-2: The image of the cavity in concrete obtained by the point source model, bandwidth: 500 kHz, spatial sampling rate: 1.59 mm, depth of cavity: 180.98 mm

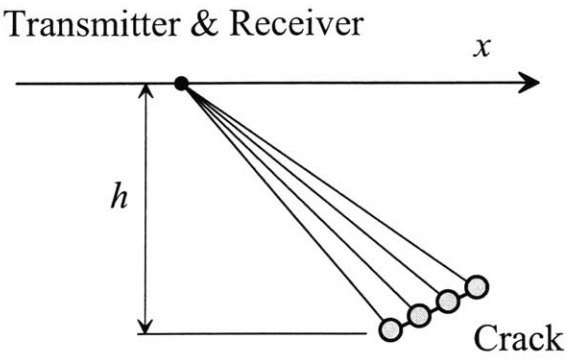

Figure 5-21: Illustration of the point source model for dipped crack. The crack is assumed to be a series of small cavities.

Table 5.4: The parameters used in the simulation (the point source model in aluminum)

Case	bandwidth	spatial sampling ratio	depth of the crack
3-1-1	500 kHz	0.80 mm	29.50 mm
3-2-1	100 kHz	0.80 mm	29.50 mm
3-2-2	1 MHz	0.80 mm	29.50 mm
3-3-1	500 kHz	3.99 mm	29.50 mm
3-3-2	500 kHz	0.16 mm	29.50 mm
3-4-1	500 kHz	0.80 mm	9.83 mm
3-4-2	500 kHz	0.80 mm	88.50 mm

crack is 1.24cm (4.2cm–5.4cm) for aluminum and 2.48cm (3.6cm–6.0cm) for concrete. The results are shown in Fig 5-22 to 5-35. Good results are obtained except for narrow bandwidth and coarse spatial sampling rate (Case 3-2-1, 4-2-1, 3-3-1, 4-3-1). The tendency is as the same as that of the cavity.

Table 5.5: The parameters used in the simulation (the point source model in concrete)

Case	bandwidth	spatial sampling ratio	depth of cavity
4-1-1	500 kHz	1.59 mm	60.33 mm
4-2-1	100 kHz	1.59 mm	60.33 mm
4-2-2	1 MHz	1.59 mm	60.33 mm
4-3-1	500 kHz	7.94 mm	60.33 mm
4-3-2	500 kHz	0.32 mm	60.33 mm
4-4-1	500 kHz	1.59 mm	20.11 mm
4-4-2	500 kHz	1.59 mm	180.98 mm

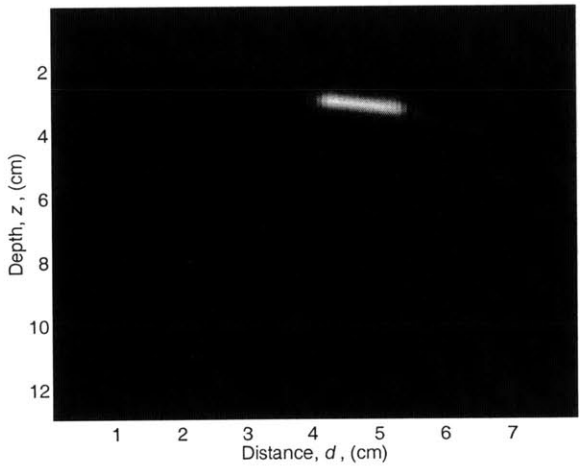

Figure 5-22: Case 3-1-1: The image of the crack in aluminum obtained by the point source model, bandwidth: 500 kHz, spatial sampling rate: 0.80 mm, the depth of crack: 29.50 mm.

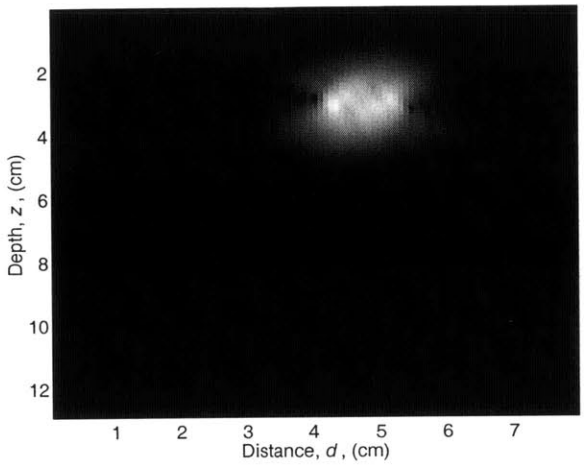

Figure 5-23: Case 3-2-1: The image of the crack in aluminum obtained by the point source model, bandwidth: 100 kHz, spatial sampling rate: 0.80 mm, the depth of crack: 29.50 mm

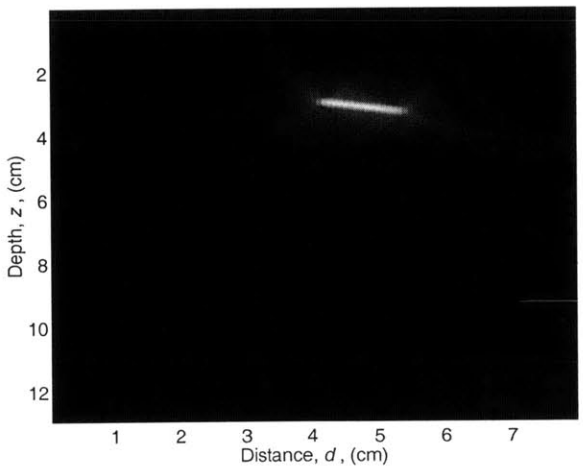

Figure 5-24: Case 3-2-2: The image of the crack in aluminum obtained by the point source model, bandwidth: 1 MHz, spatial sampling rate: 0.80 mm, the depth of crack: 29.50 mm

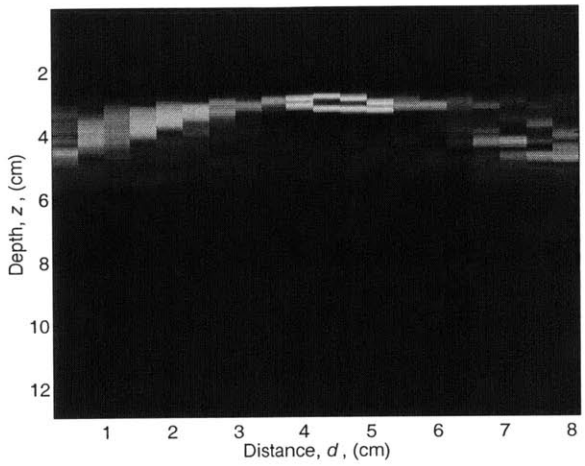

Figure 5-25: Case 3-3-1: The image of the crack in aluminum obtained by the point source model, bandwidth: 500 kHz, spatial sampling rate: 3.99 mm, the depth of crack: 29.50 mm

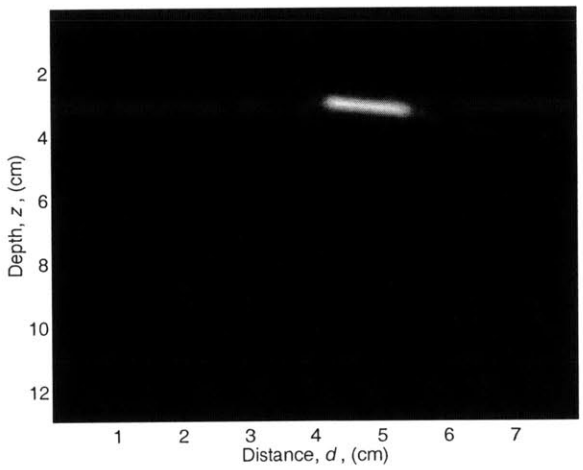

Figure 5-26: Case 3-3-2: The image of the crack in aluminum obtained by the point source model, bandwidth: 500 kHz, spatial sampling rate: 0.16 mm, the depth of crack: 29.50 mm

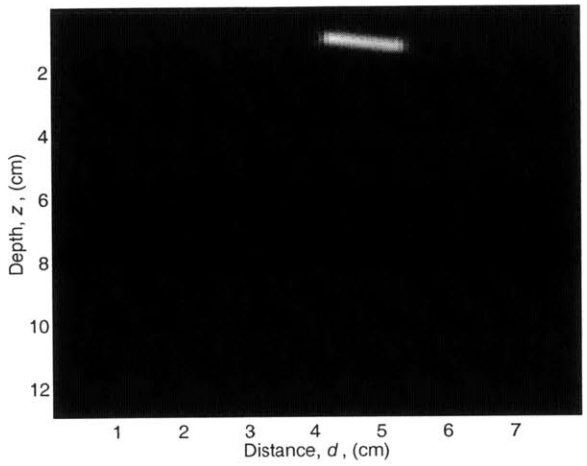

Figure 5-27: Case 3-4-1: The image of the crack in aluminum obtained by the point source model, bandwidth: 500 kHz, spatial sampling rate: 0.80 mm, the depth of crack: 9.83 mm

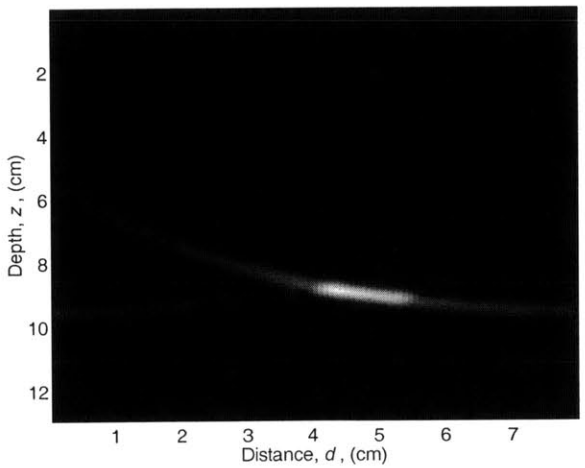

Figure 5-28: Case 3-4-2: The image of the crack in aluminum obtained by the point source model, bandwidth: 500 kHz, spatial sampling rate: 0.80 mm, the depth of crack: 88.50 mm

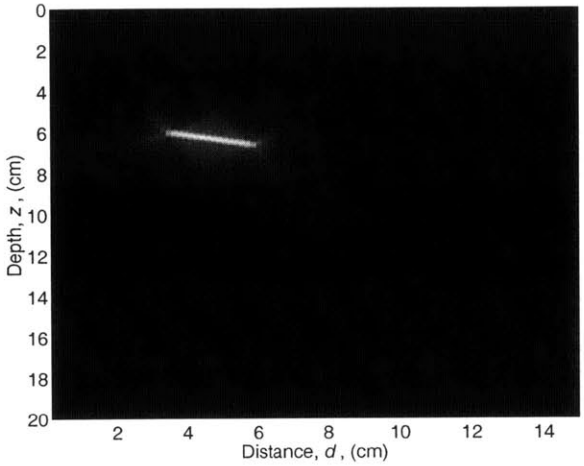

Figure 5-29: Case 4-1-1: The image of the crack in concrete obtained by the point source model, bandwidth: 100 kHz, spatial sampling rate: 1.59 mm, the depth of cavity: 60.33 mm.

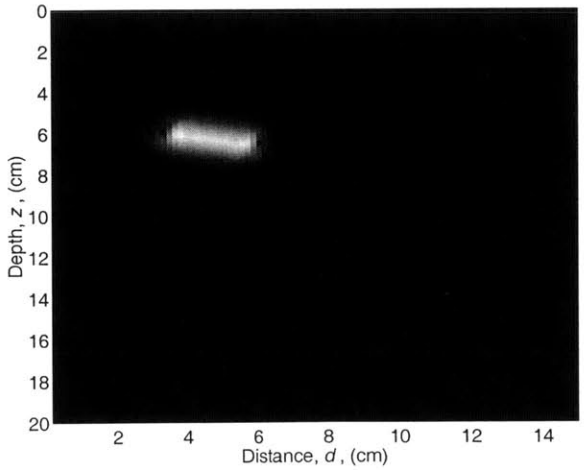

Figure 5-30: Case 4-2-1: The image of the crack in concrete obtained by the point source model, bandwidth: 20 kHz, spatial sampling rate: 1.59 mm, the depth of cavity: 60.33 mm.

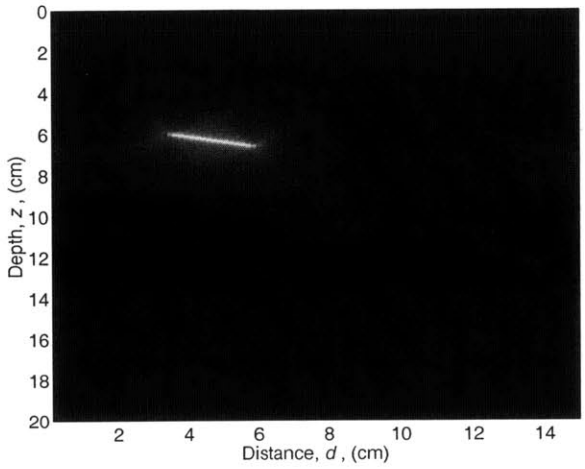

Figure 5-31: Case 4-2-2: The image of the crack in concrete obtained by the point source model, bandwidth: 500 kHz, spatial sampling rate: 1.59 mm, the depth of cavity: 60.33 mm.

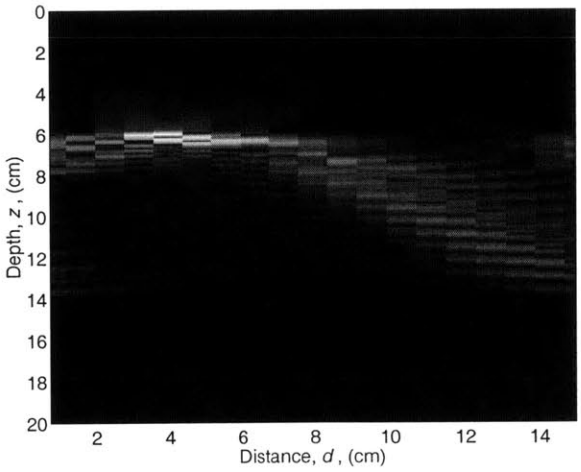

Figure 5-32: Case 4-3-1: The image of the crack in concrete obtained by the point source model, bandwidth: 500 kHz, spatial sampling rate: 7.93 mm, the depth of cavity: 60.33 mm.

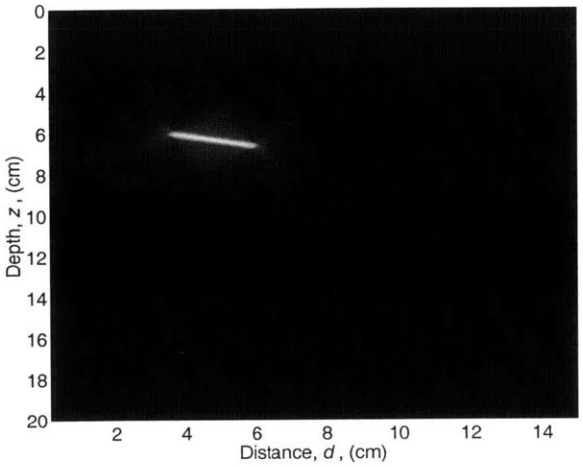

Figure 5-33: Case 4-3-2: The image of the crack in concrete obtained by the point source model, bandwidth: 500 kHz, spatial sampling rate: 0.32 mm, the depth of cavity: 60.33 mm.

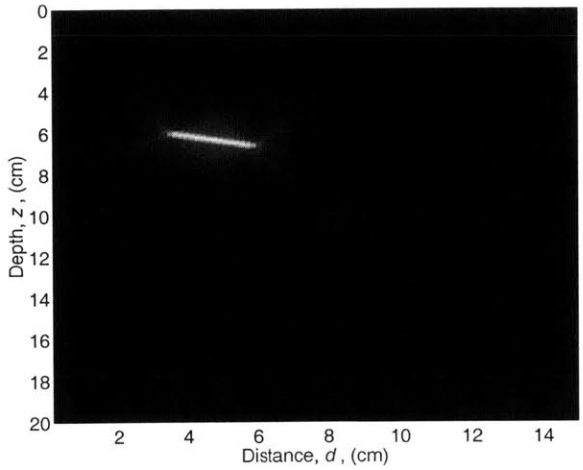

Figure 5-34: Case 4-4-1: The image of the crack in concrete obtained by the point source model, bandwidth: 500 kHz, spatial sampling rate: 1.59 mm, the depth of cavity: 20.11 mm.

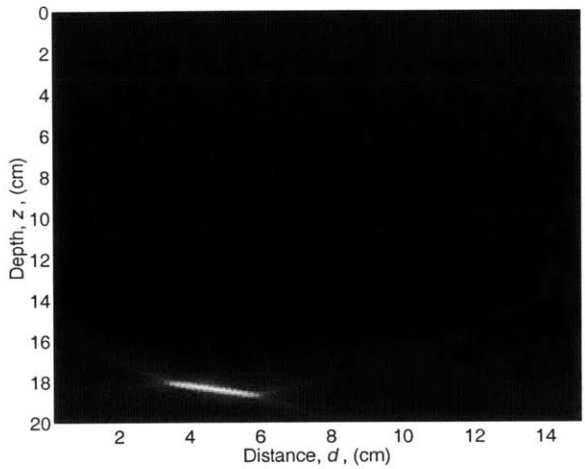

Figure 5-35: Case 4-4-2: The image of the crack in concrete obtained by the point source model, bandwidth: 500 kHz, spatial sampling rate: 1.59 mm, the depth of cavity: 180.98 mm

5.4 The directivity model

The directivity of incident wave is considered in the simulation studies based on the theoretical directivity function discussed in Chapter 3. Figure 5-36 illustrates the model, in which the directivity is considered for the transmitter and only the cosine term is used for receiver. The directivity of the scattered wave off the cavity is not considered and the scattered wave is assumed to be a spherical wave. The illustration of the directivity model for the cavity is shown in Fig. 5-36. For an incident wave, $f(t)$, the received signal, $s(x,t)$, can be expressed as

$$s(x,t) = \frac{1}{r} U_L^a(\theta_t) f\left(t - \frac{r}{c_L}\right), \tag{5.2}$$

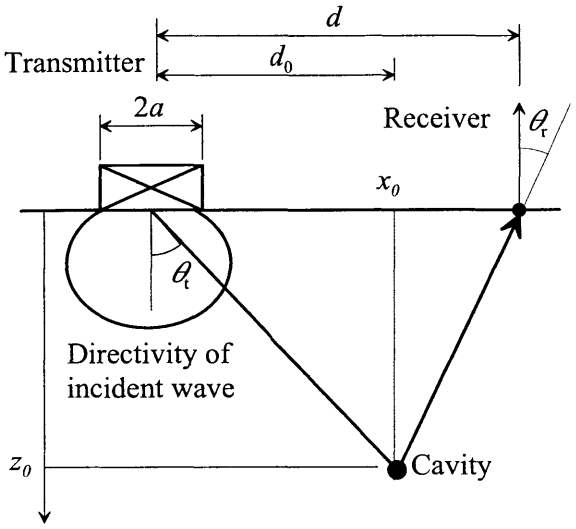

Figure 5-36: In this simulation, the directivity of the incident wave is considered and the receiver can only receive cosine term of the reflected wave.

where

$$f(t) = \exp(j\omega t)\exp(-\alpha^2 t^2),$$

$$r_i = \sqrt{d_0^2 + z_0^2} + \sqrt{(d-d_0)^2 + z_0^2},$$

$$\cos\theta_t = \frac{z_0}{\sqrt{d^2 + z_0^2}},$$

$$\cos\theta_r = \frac{z_0}{\sqrt{(d-d_0)^2 + z_0^2}},$$

$U_L^a(r,\theta)$: directivity function discussed in chapter 3,

α : bandwidth.

5.4.1 The cavity case

Aluminum specimen

The simulation results are shown in Fig. 5-37 to 5-45. Due to the directivity of the incident wave, the diffraction curve in the x-t domain is not symmetric and there exist two zero crossing (Fig. 5-37).

The effects of cavity depth and the transmitter dimension are investigated. Table 5.6 shows the parameters used in the study. When the cavity is located in the near field (Case 5-2-1), the cavity in the image appears to be inclined and a ghost signals appears in left hand side in Fig. 5-41. Since the offset is much larger than the cavity depth, the diffraction curve becomes flat (Fig. 5-39). Moreover, the wave will be reflected strongly off the cavity when the transmitter is above the cavity because of the narrow mainlobe. Thus, the diffraction curve is skewed to the right.

For a deeper cavity (Case 5-2-2), the angle θ_t in Fig. 5-36 is small, so that the effect of the directivity is less influential and the image becomes clearer (Fig. 5-42).

The image resolution is determined by the width of transmitter (Fig. 5-43, 5-44), i.e., a smaller transducer increases the resolution and vice versa (Fig. 5-43). However, a wide transmitter has well directed beam profile and more zero crossings, so that the diffraction curve is concentrated to the right and divided to several parts. This diffraction curve is similar to the shallow cavity case and the image of the cavity becomes large and inclined (Fig. 5-45).

Table 5.6: The parameters used in the simulation in aluminum (The directivity model)

Case	bandwidth	spatial sampling ratio	location of the cavity (x_0, z_0)	radius of transducer
5-1-1	500 kHz	0.80 mm	(48.1, 29.50) mm	6.35 mm
5-3-1	500 kHz	0.80 mm	(48.1, 9.83) mm	6.35 mm
5-3-2	500 kHz	0.80 mm	(48.1, 88.50) mm	6.35 mm
5-4-1	500 kHz	0.80 mm	(48.1, 29.50) mm	3.18 mm
5-4-2	500 kHz	0.80 mm	(48.1, 29.50) mm	12.70 mm

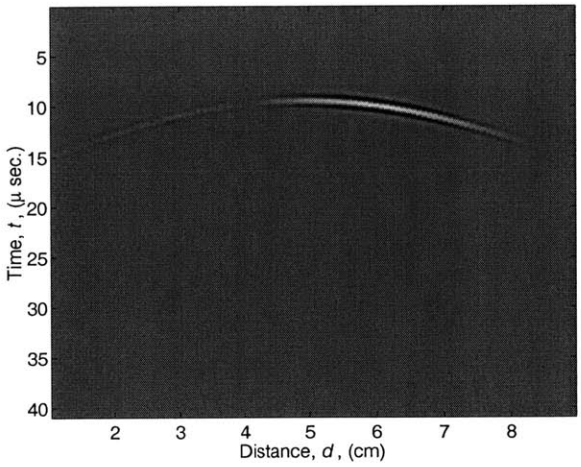

Figure 5-37: Case 5-1-1: The diffraction curve obtained by the directivity model. It is not symmetric against the apex, because of the directivity of incident wave. bandwidth: 500 kHz, spatial sampling rate: 0.80 mm, the depth of cavity: 29.50 mm, the radius of transducer: 6.35 mm

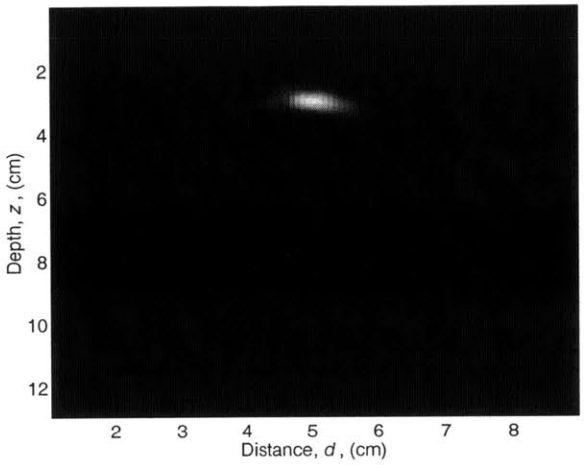

Figure 5-38: Case 5-1-1: The image of the cavity in aluminum obtained by the directivity mode, bandwidth: 500 kHz, spatial sampling rate: 0.80 mm, the depth of cavity: 29.50 mm, the radius of transducer: 6.35 mm

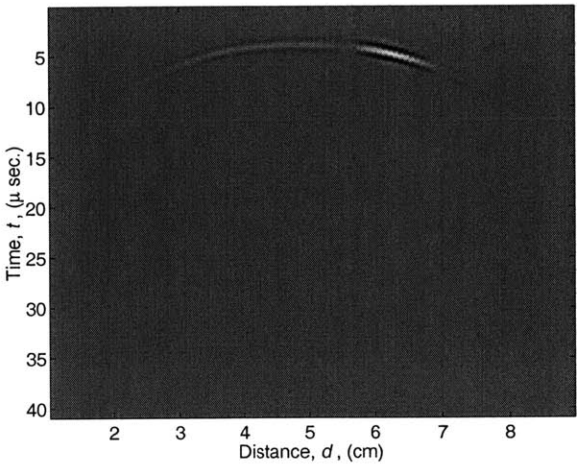

Figure 5-39: Case 5-4-1: The diffraction curve by the cavity in aluminum obtained by the directivity model. The gradient of diffraction curve is lower than it obtained by the point source case (Fig 5-40). bandwidth: 500 kHz, spatial sampling rate: 0.80 mm, the depth of cavity: 9.83 mm, the radius of transducer: 6.35 mm

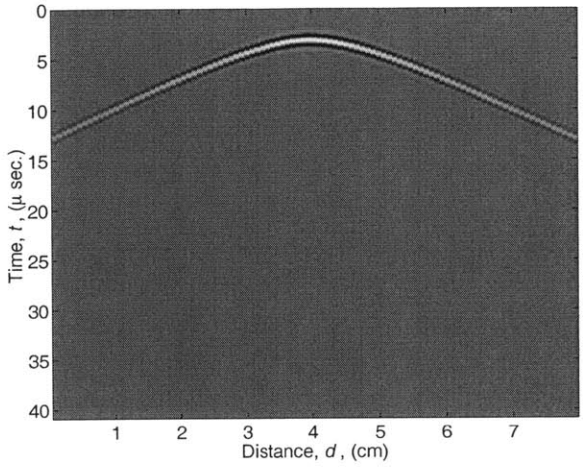

Figure 5-40: Case 1-4-1: The diffraction curve by the cavity in aluminum obtained by the point source model, bandwidth: 500 kHz, spatial sampling rate: 0.80 mm, the depth of cavity: 29.50 mm, the radius of transducer: 6.35 mm

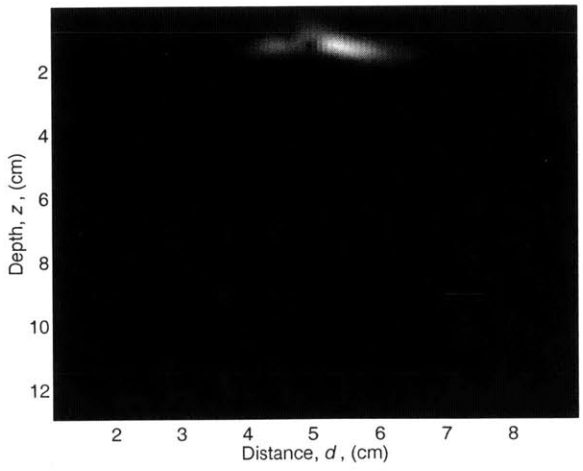

Figure 5-41: Case 5-4-1: The image of the cavity in aluminum obtained by the directivity model, bandwidth: 500 kHz, spatial sampling rate: 0.80 mm, the depth of cavity: 9.83 mm, the radius of transducer: 6.35 mm

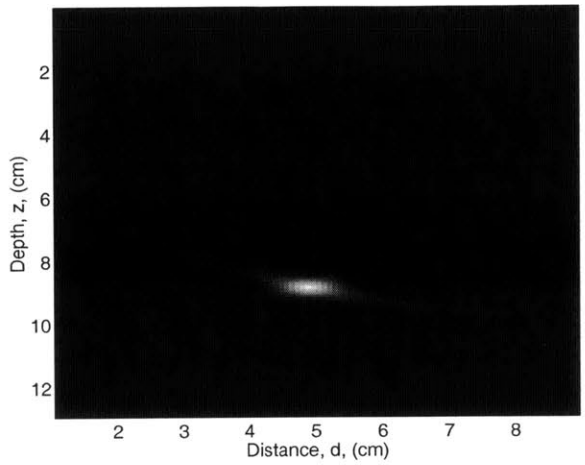

Figure 5-42: Case 5-4-2: The image of the cavity in aluminum obtained by the directivity model, bandwidth: 500 kHz, spatial sampling rate: 0.80 mm, the depth of cavity: 88.50 mm, width of transmitter: 6.35 mm

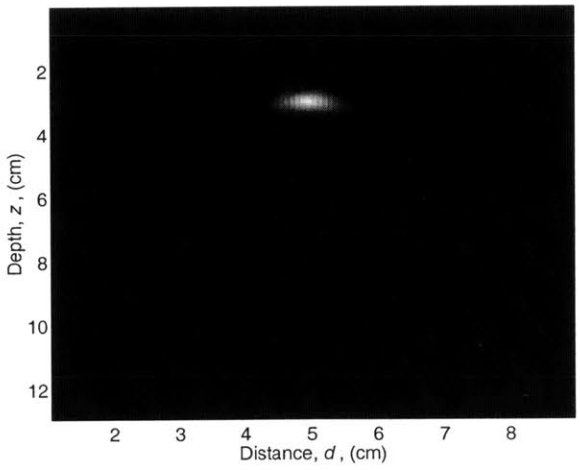

Figure 5-43: Case 5-5-1: The image of the cavity in aluminum obtained by the directivity model, bandwidth: 500 kHz, spatial sampling rate: 0.80 mm, the depth of cavity: 29.50 mm, the width of transmitter: 3.18 mm

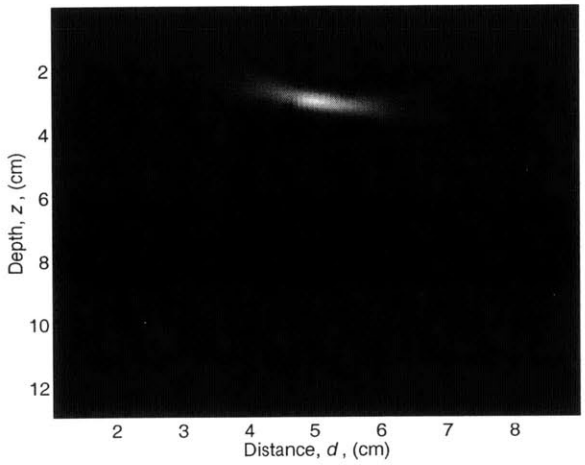

Figure 5-44: Case 5-5-2: The image of the cavity in aluminum obtained by the directivity model, bandwidth: 500 kHz, spatial sampling rate: 0.80 mm, the depth of cavity: 12.70 mm, the radius of transducer: 12.70 mm

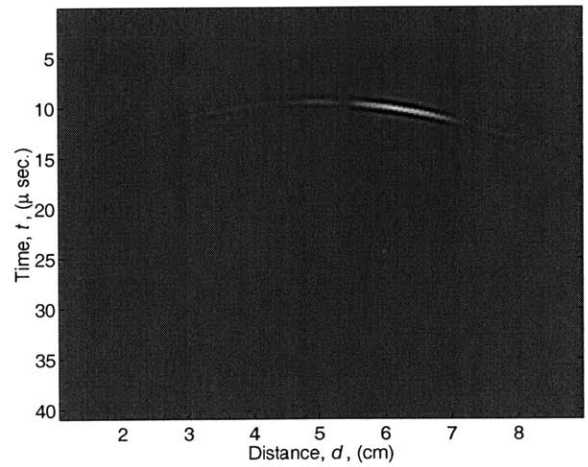

Figure 5-45: Case 5-5-2: The diffraction curve by the cavity in aluminum obtained by the directivity model, bandwidth: 500 kHz, spatial sampling rate: 0.80 mm, the depth of cavity: 29.50 mm, the radius of transducer: 12.70 mm

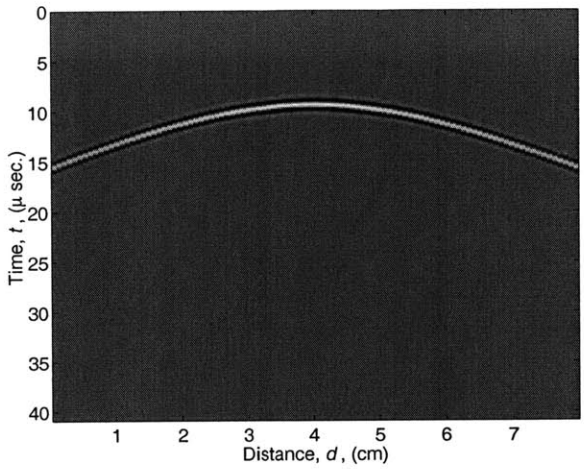

Figure 5-46: Case 5-5-2: The diffraction curve by the cavity in aluminum obtained by the directivity model, bandwidth: 500 kHz, spatial sampling rate: 0.80 mm, the depth of cavity: 29.50 mm, the radius of transducer: 12.70 mm

Concrete specimen

Figures 5-53 to 5-55 shows the results for concrete. The directivity of incident wave in concrete is more directed than that in aluminum. Thus, the images for Case 6-1-1 and 6-3-1 are greatly distorted. In order to reconstruct better images, the filter discussed in Chapter 4 is applied for these cases. The filtered diffraction curves and those without filtering are compared in Figs 5-53 and 5-48. Without filtering, the diffraction curve is skewed to the right. After the filtering, strong amplitude shift to the vicinity of the center and the shape of the diffraction curve around vicinity of the apex becomes steeper without changing the position of the apex. The image of the cavity becomes smaller and located at the exact position (Fig. 5-53 and 5-48). The image could not be constructed correctly for a shallow cavity. In this case, the diffraction curve is divided into several sections due to the zero

Table 5.7: The parameters used in the simulation in concrete (The directivity model)

Case	bandwidth	spatial sampling ratio	location of the cavity (x_0, z_0)	radius of transducer
6-1-1	500 kHz	1.59 mm	(86.2, 60.33) mm	20.64 mm
6-3-1	500 kHz	1.59 mm	(86.2, 20.11) mm	20.64 mm
6-3-2	500 kHz	1.59 mm	(86.2, 180.98) mm	20.64 mm
6-4-1	500 kHz	1.59 mm	(86.2, 60.33) mm	10.32 mm

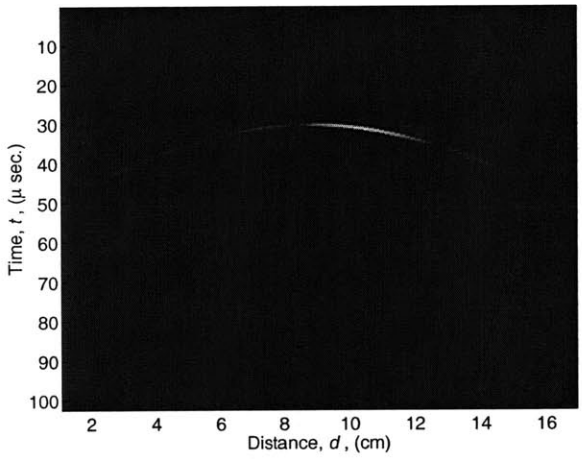

Figure 5-47: 6-1-1: The diffraction curve obtained by the directivity model without filtering, concrete case, bandwidth: 500 kHz, spatial sampling rate: 1.59 mm, the depth of cavity: 60.33 mm, the radius of transducer: 20.64 mm

crossings of the directivity function (Fig. 5-53). These zero crossing points prevent us from constructing correct images.

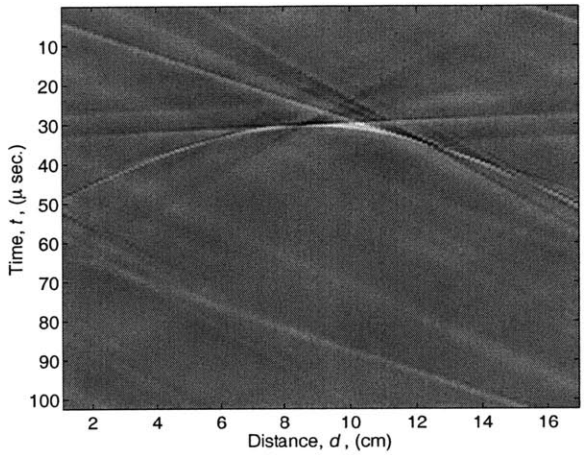

Figure 5-48: 6-1-1: The diffraction curve obtained by the directivity model with filtering, concrete case, bandwidth: 500 kHz, spatial sampling rate: 1.59 mm, the depth of cavity: 60.33 mm, the radius of transducer: 20.64 mm

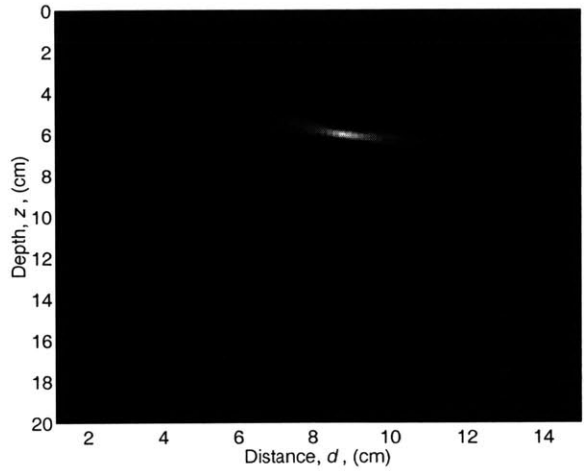

Figure 5-49: 6-1-1: The image of the cavity in concrete obtained by the directivity model without filtering, bandwidth: 500 kHz, spatial sampling rate: 1.59 mm, the depth of cavity: 60.33 mm, the radius of transducer: 20.64 mm

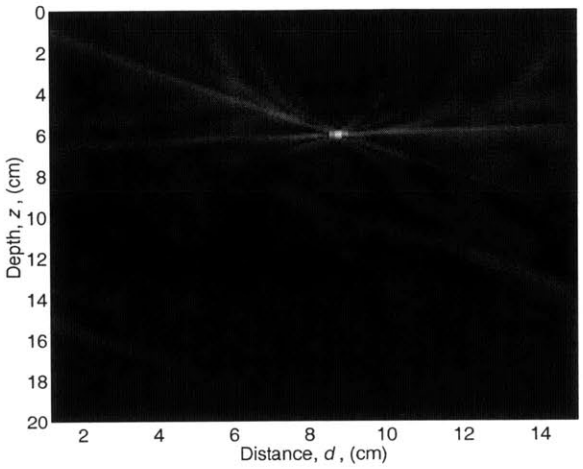

Figure 5-50: 6-1-1: The image of the cavity in concrete obtained by the directivity model applied filter discussed in Chapter 4, bandwidth: 500 kHz, spatial sampling rate: 1.59 mm, the depth of cavity: 60.33 mm, the radius of transducer: 20.64 mm

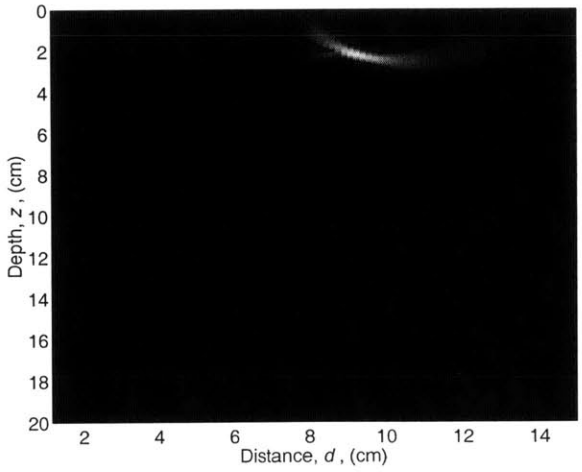

Figure 5-51: Case 6-2-1: The image of the cavity in concrete obtained by the directivity model, bandwidth: 500 kHz, spatial sampling rate: 1.59 mm, the depth of cavity: 20.11 mm, the radius of transducer: 20.64 mm

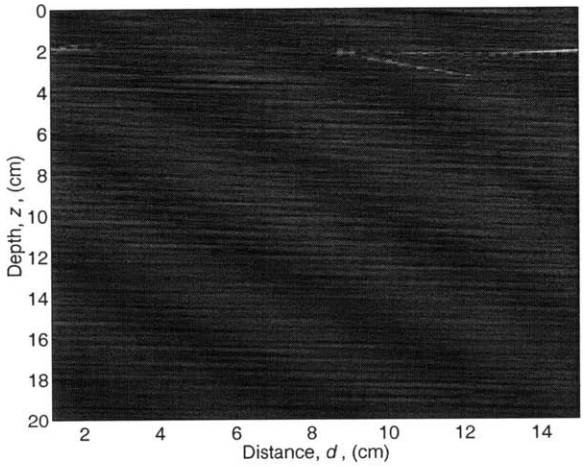

Figure 5-52: Case 6-2-1: The image of the cavity in concrete obtained by the directivity model applied filter discussed in Chapter 4, bandwidth: 500 kHz, spatial sampling rate: 1.59 mm, the depth of cavity: 60.33 mm, the radius of transducer: 20.64 mm

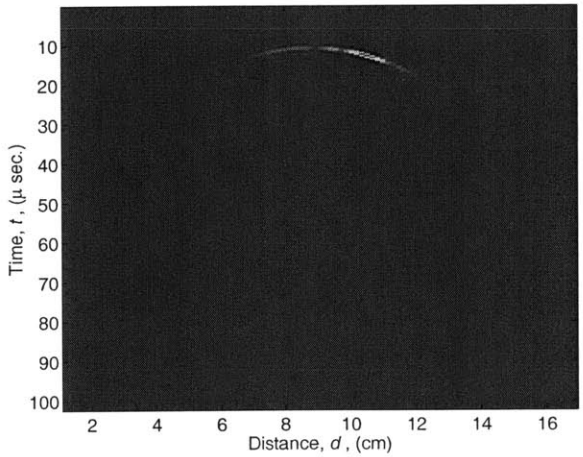

Figure 5-53: 6-1-1: The diffraction curve obtained by the directivity model without filtering, concrete case, bandwidth: 500 kHz, spatial sampling rate: 1.59 mm, the depth of cavity: 20.11 mm, the radius of transducer: 20.64 mm

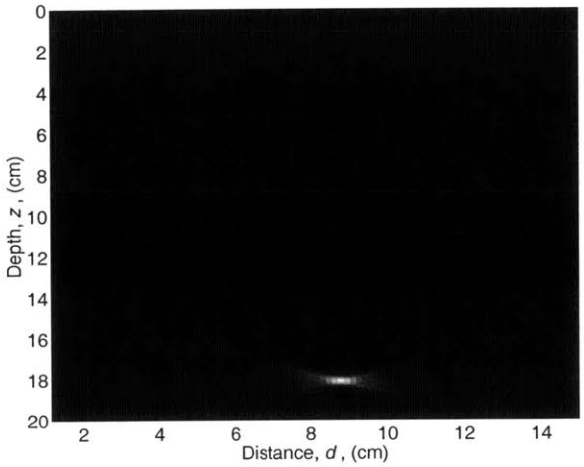

Figure 5-54: Case 6-2-2: The image of the cavity in concrete obtained by the directivity model, bandwidth: 500 kHz, spatial sampling rate: 1.59 mm, the depth of cavity: 180.98 mm, the width of transmitter: 20.64 mm

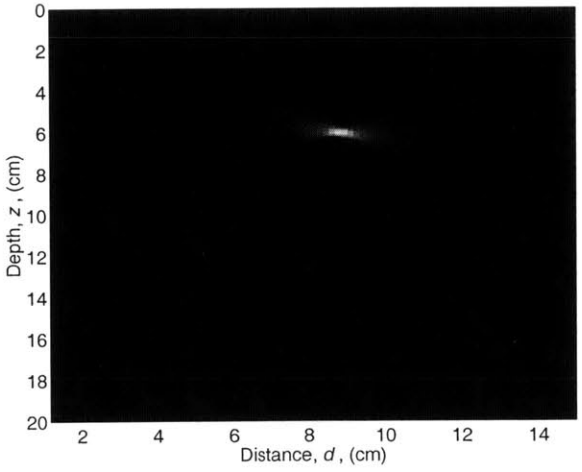

Figure 5-55: Case 6-3-1: The image of the cavity in concrete obtained by the directivity model applied filter discussed in Chapter 4, bandwidth: 500 kHz, spatial sampling rate: 1.59 mm, depth of cavity: 60.33 mm, width of transmitter: 10.32 mm

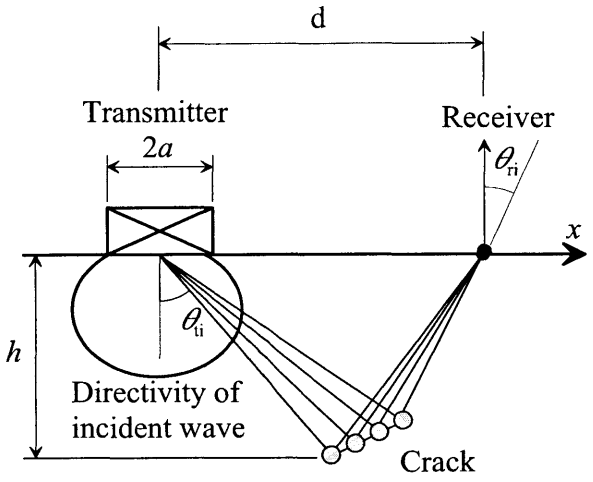

Figure 5-56: The transmitter is assumed to be point source.

5.4.2 Crack

Like the Case 3 simulation study, a crack is regarded as series of small cavities (Fig. 5-56). In addition, the directivity of incident wave is considered in this study. The crack is inclined 14.0 degree and the length of crack is 1.24cm (5.2cm–6.4cm) for aluminum and 2.48cm (4.6cm–7.0cm) for concrete. The results are shown in Fig. 5-57 to 5-65. The results are more obscure than those of the point source model, but they are generally satisfactory except for shallow crack cases and Case 8-1-1. In the case of shallow crack (Fig. 5-58 and 5-63), the length of crack appears shorter than the actual length and the image is shifted to the right.

Table 5.8: The parameters used in the simulation in aluminum (the directivity model in aluminum)

Case	bandwidth	spatial sampling ratio	depth of the crack	radius of transducer
7-1-1	500 kHz	0.80 mm	29.50 mm	6.35 mm
7-3-1	500 kHz	0.80 mm	9.83 mm	6.35 mm
7-3-2	500 kHz	0.80 mm	88.50 mm	6.35 mm
7-4-1	500 kHz	0.80 mm	29.50 mm	3.18 mm
7-4-2	500 kHz	0.80 mm	29.50 mm	12.70 mm

Table 5.9: The parameters used in the simulation in concrete (the directivity model in concrete)

Case	bandwidth	spatial sampling ratio	depth of the crack	radius of transducer
8-1-1	500 kHz	0.80 mm	29.50 mm	20.64 mm
8-3-1	500 kHz	0.80 mm	20.11 mm	20.64 mm
8-3-2	500 kHz	0.80 mm	180.98 mm	20.64 mm
8-4-1	500 kHz	0.80 mm	29.50 mm	10.32 mm

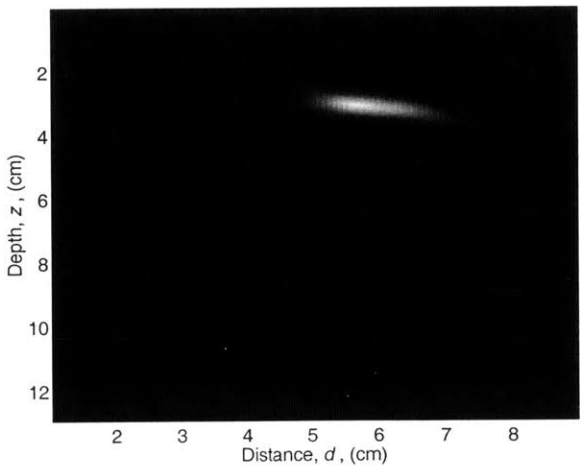

Figure 5-57: Case 7-1-1: The image of crack in aluminum obtained by the directivity model, bandwidth: 500 kHz, spatial sampling rate: 0.80 mm, the depth of crack: 29.50 mm, the radius of transducer: 6.35 mm.

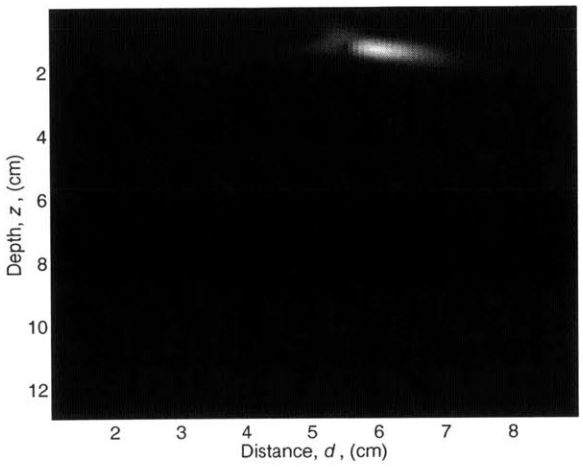

Figure 5-58: Case 7-4-1: The image of the crack in aluminum obtained by the directivity model, bandwidth: 500 kHz, spatial sampling rate: 0.80 mm, the depth of crack: 9.83 mm, the radius of transducer: 6.35 mm.

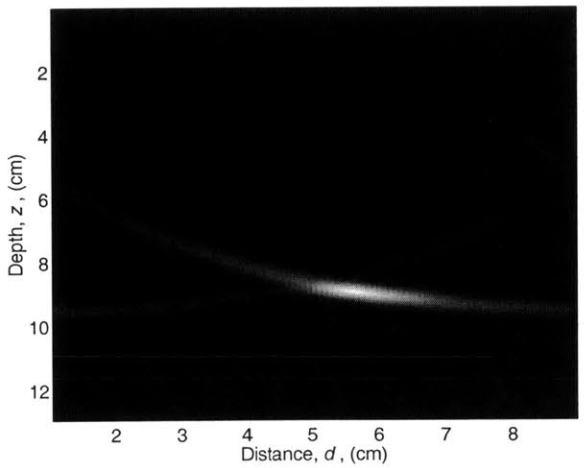

Figure 5-59: Case 7-4-2: The image of the crack in aluminum obtained by the directivity model, bandwidth: 500 kHz, spatial sampling rate: 0.80 mm, the depth of crack: 88.50 mm, the radius of transducer: 6.35 mm.

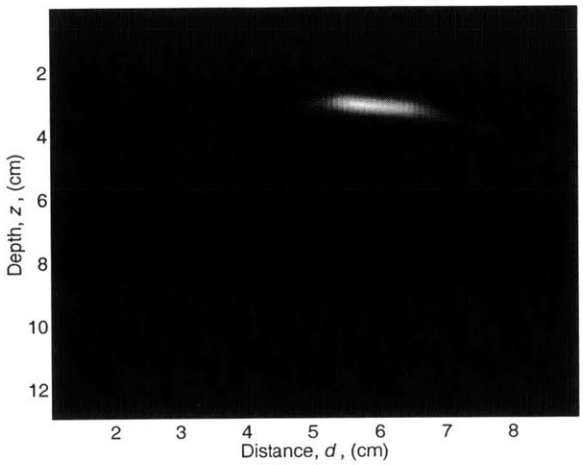

Figure 5-60: Case 7-5-1: The image of the crack in aluminum obtained by the directivity model, bandwidth: 500 kHz, spatial sampling rate: 0.80 mm, the depth of crack: 29.50 mm, the radius of transducer: 3.18 mm.

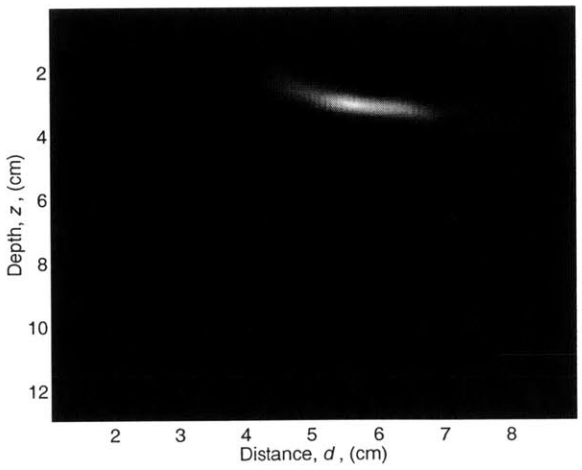

Figure 5-61: Case 7-5-2: The image of the crack in aluminum obtained by the directivity model, bandwidth: 500 kHz, spatial sampling rate: 0.80 mm, the depth of crack: 29.50 mm, the radius of transducer: 12.70 mm.

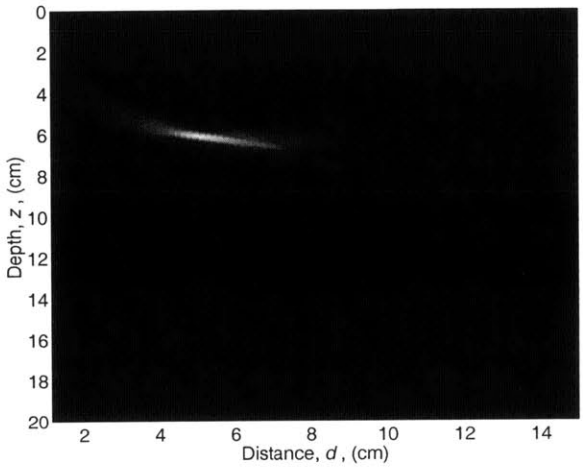

Figure 5-62: Case 8-1-1: The image of the crack in concrete obtained by the directivity model, bandwidth: 500 kHz, spatial sampling rate: 0.80 mm, the depth of crack: 60.33 mm, the radius of transducer: 20.64 mm.

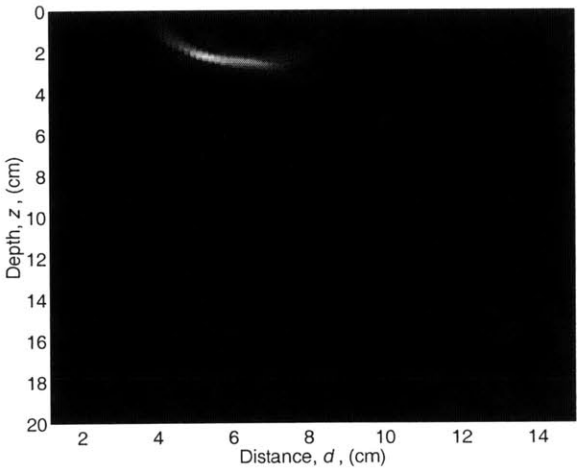

Figure 5-63: Case 8-4-1: The image of the crack in concrete obtained by the directivity model, bandwidth: 500 kHz, spatial sampling rate: 1.59 mm, the depth of crack: 20.11 mm, the radius of transducer: 20.64 mm.

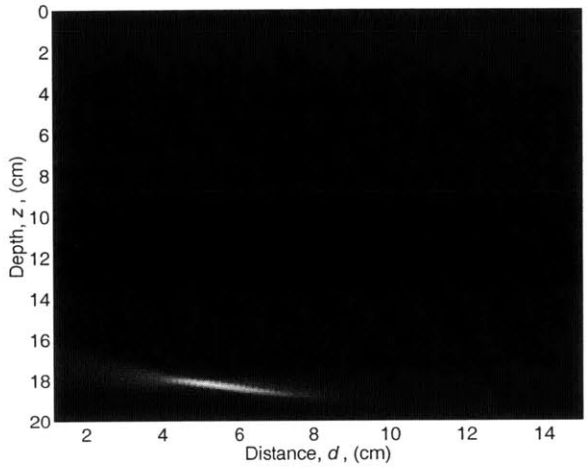

Figure 5-64: Case 8-4-2: The image of the crack in concrete obtained by the directivity model, bandwidth: 500 kHz, spatial sampling rate: 1.59 mm, the depth of crack: 180.98 mm, the radius of transducer: 20.64 mm.

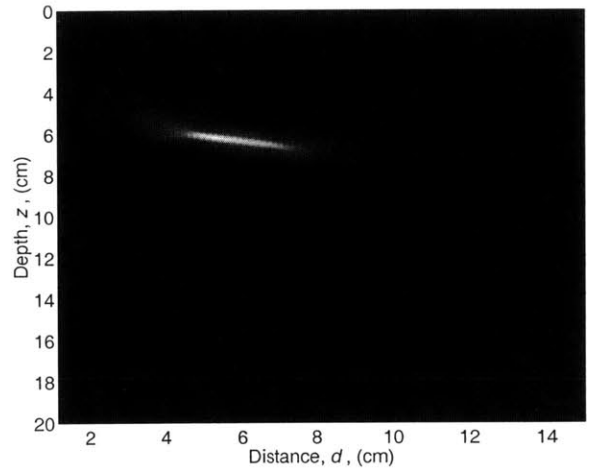

Figure 5-65: Case 8-5-1: The image of the crack in concrete obtained by the directivity model, bandwidth: 500 kHz, spatial sampling rate: 1.59 mm, the depth of crack: 60.33 mm, the radius of transducer: 10.32 mm.

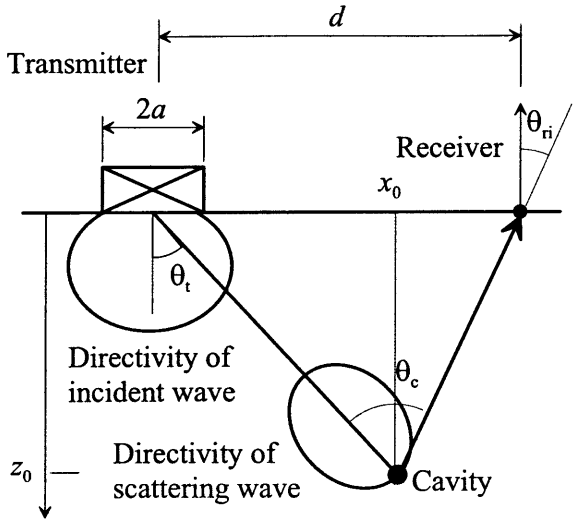

Figure 5-66: In this simulation, the directivity of the incident wave and scattering field off the cavity are considered and the receiver can only receive cosine term of the reflected wave.

5.5 Scattering model

The directivity of scattering wave is also considered as well as that of the incident wave (Fig. 5-66). The condition of this simulation is quite similar to the experimental condition.

The received signal can be rewritten as

$$s(x,t) = \frac{1}{r} U_L^a(\theta) H_L^{ac}(\theta, r) f\left(t - \frac{r}{c_L}\right) \tag{5.3}$$

where

$$f(t) = e^{i\omega t}e^{-\alpha^2 t^2},$$

$$r_i = \sqrt{(x - d_{ri})^2 + z_0^2},$$

$$\cos\theta_2 = \frac{z_0}{r_i},$$

$U_L^a(\theta)$: directivity of the incident wave,

$H_L^{a_c}(\theta, r)$: directivity of scattering wave,

α : bandwidth.

The configuration of this simulation is shown in Table 5.10 for a cavity of 1.59 mm radius and the results are shown in Figs. 5-67 to 5-77. The angle θ_c in Fig. 5-66 depends on the depth and offset. The maximum angle occurs when the mid point between the transmitter and receiver is above the cavity. If d is 25.4 mm and h is 29.50 mm (Case 9-1-1), the maximum angle is 43.6 degree. Referring to the directional characteristics of scattering wave in Chapter 3 (Fig. 3-5), the amplitude is approximately 60% of the amplitude at zero degree. Therefore, the effect of the directivity due to scattering is not significant and the image of the cavity is similar to the result in Case 5. However, in the Case 9-4-1, the maximum angle becomes more than 90 degree, and the amplitude becomes 20% of maximum amplitude. Thus, the amplitude at the apex of diffraction curve becomes small, and diffraction curve split into several parts (Fig. 5-69). This causes the deteriolation

Table 5.10: The parameters used in the simulation (the scattering model)

Case	bandwidth	spatial sampling ratio	location of the cavity (x_0, z_0)	radius of transducer	radius of cavity
9-1-1	500 kHz	0.80 mm	(48.10, 29.50) mm	6.35 mm	1.59 mm
9-4-1	500 kHz	0.80 mm	(48.10, 9.83) mm	6.35 mm	1.59 mm
9-4-2	500 kHz	0.80 mm	(48.10, 88.50) mm	6.35 mm	1.59 mm
9-6-1	500 kHz	0.80 mm	(48.10, 29.50) mm	6.35 mm	12.7 mm

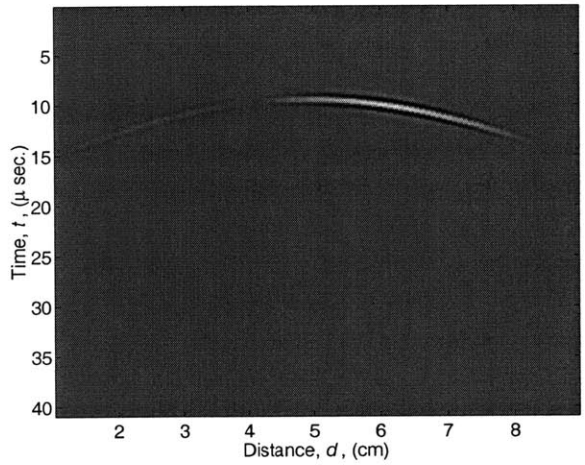

Figure 5-67: Case 9-1-1: The diffraction curve by the cavity in aluminum obtained by the scattering model, bandwidth: 500 kHz, spatial sampling rate: 0.80 mm, the depth of cavity: 29.50 mm, the width of the transducer: 6.35 mm the radius of cavity: 1.59 mm.

of the image (Fig. 5-70). Furthermore, in the case of Case 9-6-1, because of well-directed wave and zero crossing, the diffraction curve is also distorted (Fig. 5-72).

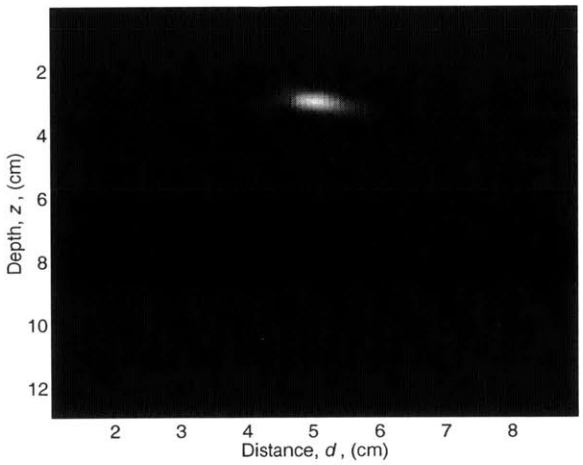

Figure 5-68: Case 9-1-1: The image of the cavity in aluminum obtained by the scattering model, bandwidth: 500 kHz, spatial sampling rate: 0.80 mm, the depth of cavity: 29.50 mm, the width of the transducer: 6.35 mm, the radius of cavity: 1.59 mm.

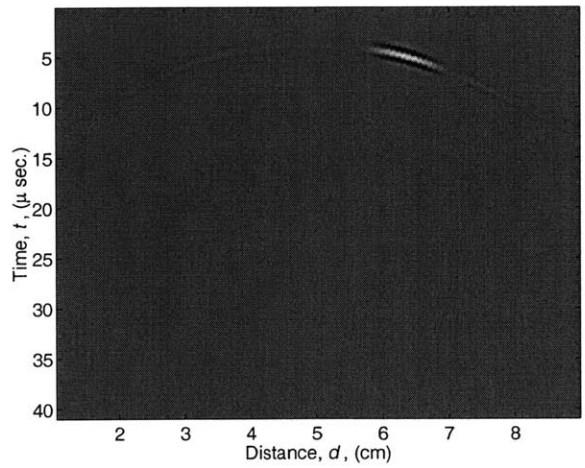

Figure 5-69: Case 9-4-1: The diffrction curve the cavity in aluminum obtained by the scattering model, bandwidth: 500 kHz, spatial sampling rate: 0.80 mm, the depth of cavity: 9.83 mm, the width of the transducer: 6.35 mm, the radius of cavity: 1.59 mm.

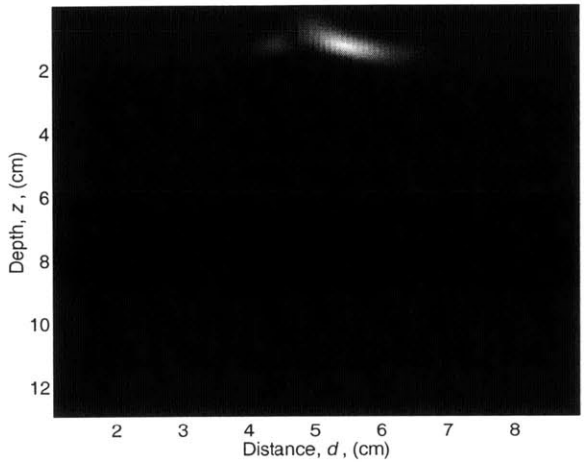

Figure 5-70: Case 9-4-1: The image of the cavity in aluminum obtained by the scattering model, bandwidth: 500 kHz, spatial sampling rate: 0.80 mm, the depth of cavity: 9.83 mm, the width of the transducer: 6.35 mm, the radius of cavity: 1.59 mm.

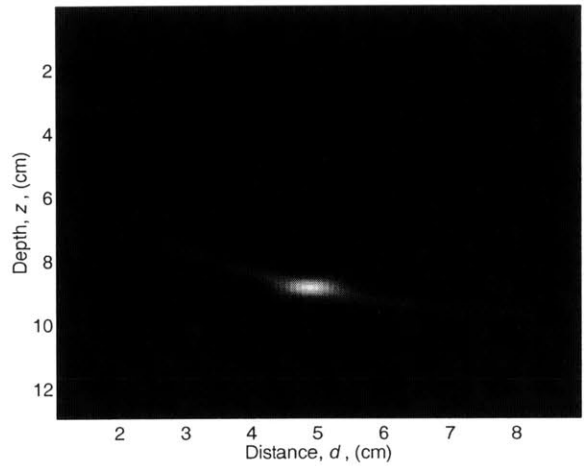

Figure 5-71: Case 9-4-2: The image of the cavity in aluminum obtained by the scattering model, bandwidth: 500 kHz, spatial sampling rate: 0.80 mm, depth of cavity: 88.50 mm, the width of the transducer: 6.35 mm, the radius of cavity: 1.59 mm.

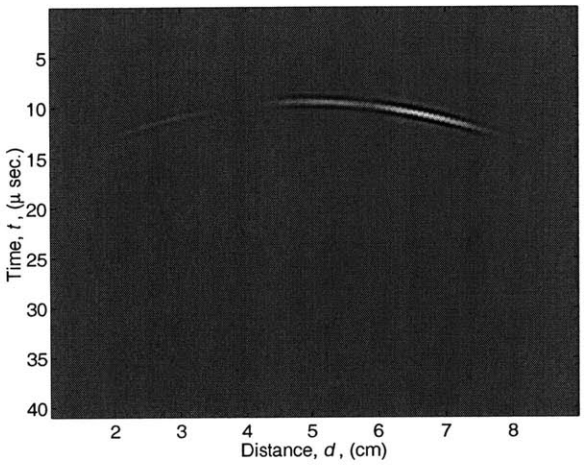

Figure 5-72: Case 9-6-1: The diffraction curve by the cavity in aluminum obtained by the scattering model, bandwidth: 500 kHz, spatial sampling rate: 0.80 mm, depth of cavity: 29.50 mm, width of transmitter: 3.18 mm, the radius of cavity: 12.7 mm.

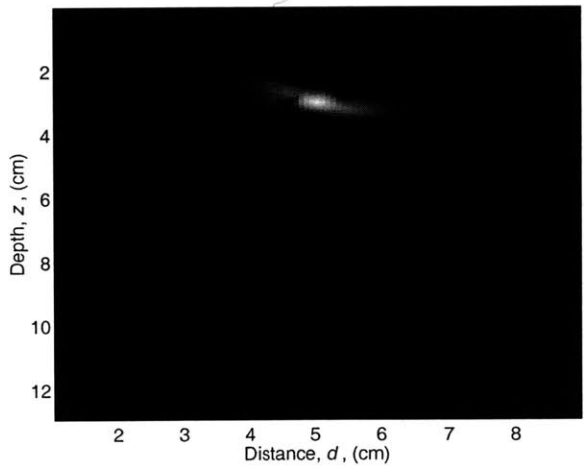

Figure 5-73: Case 9-6-1: The image of the cavity in aluminum obtained by the scattering model, bandwidth: 500 kHz, spatial sampling rate: 0.80 mm, depth of cavity: 29.50 mm, width of transmitter: 3.18 mm, the radius of cavity: 12.7 mm.

Table 5.11: The parameters used in the simulation (The scattering model)

Case	bandwidth	spatial sampling ratio	location of the cavity (x_0, z_0)	width of transmitter	radius of the cavity
10-1-1	500 kHz	1.59 mm	(86.2, 60.33) mm	20.64 mm	12.7 mm
10-4-1	500 kHz	1.59 mm	(86.2, 20.11) mm	20.64 mm	12.7 mm
10-4-2	500 kHz	1.59 mm	(86.2, 180.98) mm	20.64 mm	12.7 mm
10-5-2	500 kHz	1.59 mm	(86.2, 60.33) mm	20.64 mm	12.7 mm

5.5.1 Concrete specimen

In this simulation, the parameters are set as follows: bandwidth: 500 kHz, spatial sampling ratio: 1.59 mm, radius of transducer: 20.64 mm. Referring back to Chapter 3 (Fig. 3-7), the scattered wave propagates within narrow angles ($\pm$ 20 degree). Thus, the extremely small portion of the diffraction curve can be shown. Moreover, it is deviated by zero crossings (Fig. 5-74). Reconstruction of the image is very difficult even by using this filter.

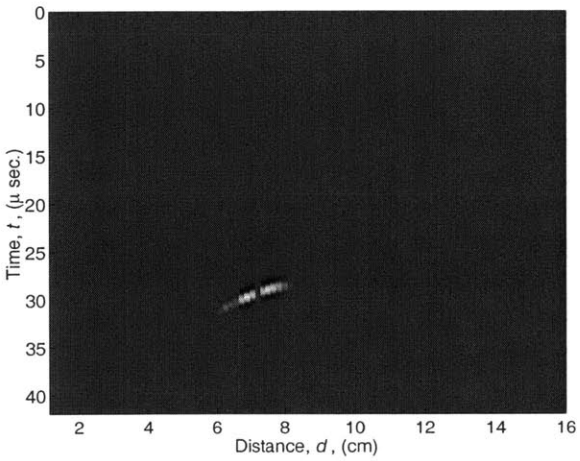

Figure 5-74: Case 10-1-1: The image of the cavity in concrete obtained by the scattering model applied filtering, bandwidth: 500 kHz, spatial sampling rate: 1.59 mm, depth of cavity: 60.33 mm, the width of transmitter: 20.64 mm, the radius of cavity: 12.7 mm.

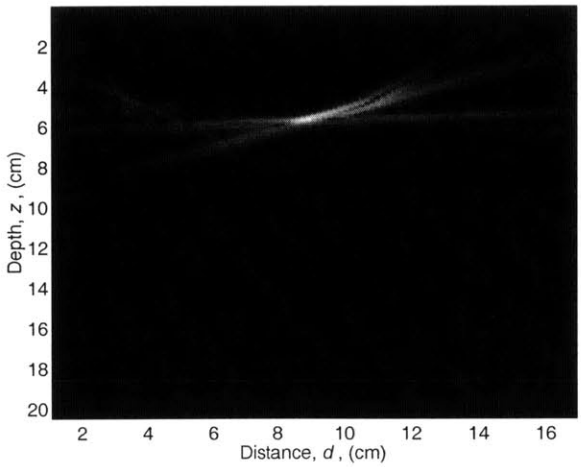

Figure 5-75: Case 10-1-1: The image of the cavity in concrete obtained by the scattering model applied filtering, bandwidth: 500 kHz, spatial sampling rate: 1.59 mm, depth of cavity: 60.33 mm, the width of transmitter: 20.64 mm, the radius of cavity: 12.7 mm.

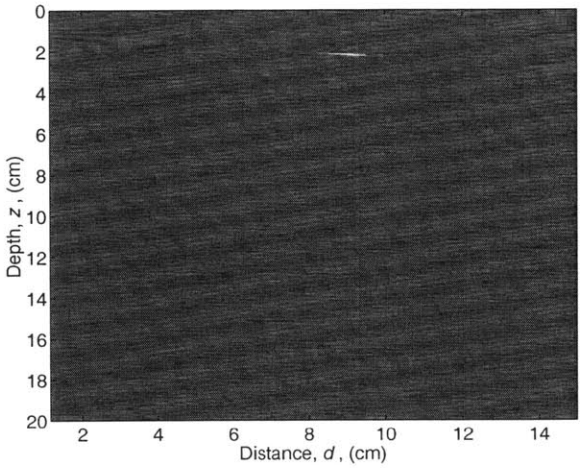

Figure 5-76: Case 10-4-1: The image of the cavity in concrete obtained by the scattering model applied filtering, bandwidth: 500 kHz, spatial sampling rate: 1.59 mm, depth of cavity: 20.11 mm, the width of transmitter: 20.64 mm, the radius of cavity: 12.7 mm.

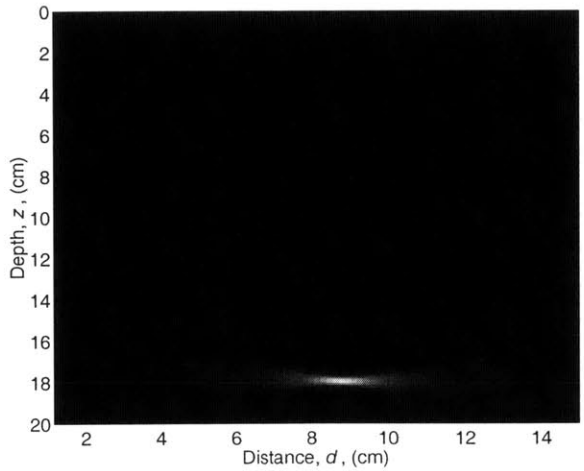

Figure 5-77: Case 10-4-2: The image of the cavity in concrete obtained by the scattering model, bandwidth: 500 kHz, spatial sampling rate: 1.59 mm, depth of cavity: 180.98 mm, the width of transmitter: 20.64 mm, the radius of cavity: 12.7 mm.

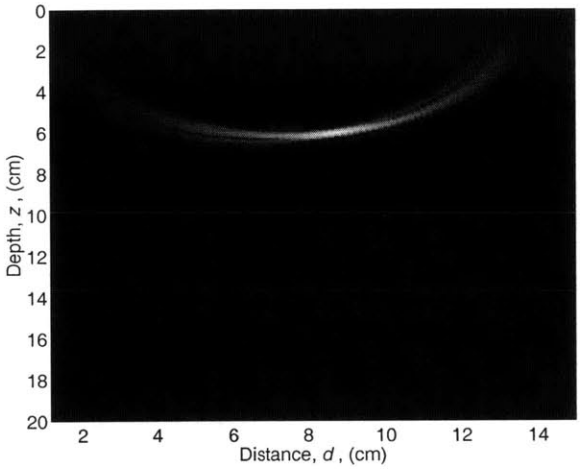

Figure 5-78: Case 10-6-1: The image of the cavity in aluminum obtained by the scattering model, bandwidth: 500 kHz, spatial sampling rate: 1.59 mm, depth of cavity: 60.33 mm, the width of transmitter: 20.64 mm, the radius of cavity: 25.4 mm.

Chapter 6

Experimental Results

The experimental results are discussed in this chapter for aluminum and mortar specimen.

6.1 Aluminum specimen

The aluminum specimens are scanned in an immersion tank. The transducers used in the experiments are 1 MHz unfocused transducers operating in pitch-catch mode as shown in Fig. 6-1. The measurements are made at 50, 98 or 150 points on the surface, respectively. For simplicity, the data stacking is not employed in this process. The detailed configuration of the experiments is shown in Table 6.1, and 6.2.

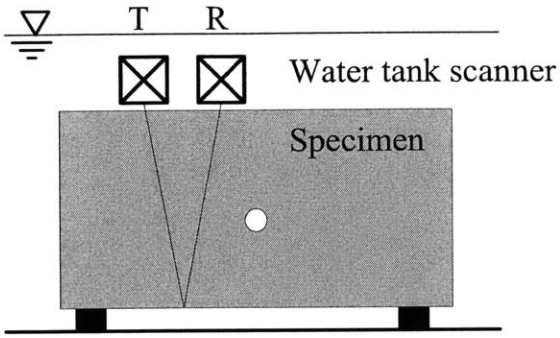

Figure 6-1: The experiment of the aluminum block is carried out in this water tank scanner.

Table 6.1: The configurations of the parameters used in the experiments (Specimen with cavity)

Specimen	Case 1	Case 2	Case 3	Case 4
Model	One cavity	One cavity	One cavity	Ten cavities
The depth of discontinuity	29.5 mm	29.5 mm	66.5 mm	1.8–75.0 mm
The radius of the cavity	1.59 mm	1.59 mm	1.59 mm	0.79 mm
Transducer	1MHz flat	1MHz flat	1MHz flat	1MHz flat
Radius of the transducer	6.35 mm	6.35 mm	6.35 mm	6.35 mm
Sampling frequency	25MHz	25MHz	25MHz	25MHz
Data number	1024	1024	1024	1024
Offset	28.6 mm	28.6 mm	28.6 mm	28.6 mm
The number of measurement	50	98	98	150

Table 6.2: The configuration of the parameters used in the experiment (Specimen with crack)

Specimen	Case 5
Model	One dipped crack
The depth of discontinuity	32.50 mm
The length of the crack	9.6 mm
The angle of crack	14.0 °
Transducer	1MHz flat
Radius of the transducer	6.35 mm
Sampling frequency	25MHz
Data number	1024
Offset	28.6 mm
The number of shot	50

6.1.1 The specimen with a cavity

The measured diffraction curves of Case 1 is shown in Figs. 6-2 and 6-3 . The horizontal line appearing approximately at 35 μsec represents the echo reflected off the boundary, and the curves appearing near 13 to 25 μsec are the echoes returned from the cavity. Waves of various mode arrive at different times, i.e., PP wave (13 μsec), and PS (19 μsec) and SS waves (25 μsec). The image of the internal structure is shown in Fig. 6-4. Since the reflected waves off the boundary is strong, the image of the cavity looks vanished. The magnified image is shown in Fig. 6-5.

However the wave from transmitter propagates both in water and aluminum, to avoid complicated calculation, only the constant wave speed, which is wave speed in aluminum, is employed in migration. Therefore, the image of the cavity may appear the deeper position than actual one, because wave speed in water (1480 m/s) is slower than that in aluminum

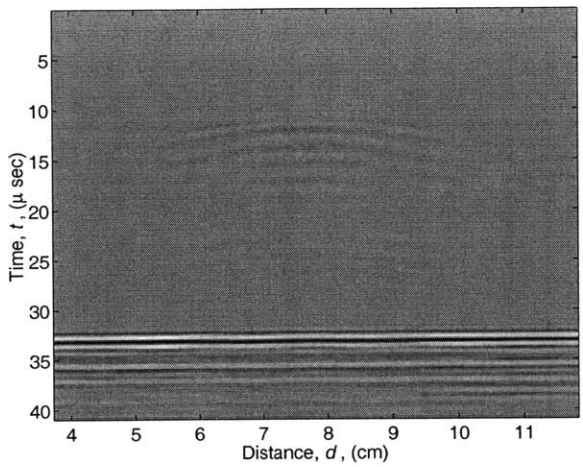

Figure 6-2: Case 1: The diffraction curve by the cavity and the border of aluminum specimen, spatial sampling rate: 1.59 mm, depth of cavity: 30.00 mm, the radius of the transducer: 6.35mm.

(6320 m/s). The distance between the transducer and the surface of aluminum is 1mm. Thus, the image of the cavity in these figure locates 4.27 mm deeper than actual position, say 33.8 mm. The image which location is compensated is shown in Fig. 6-6. The image is shifted to the proper position, 29.5 mm.

The spatial sampling rate is changed without changing the other conditions from the previous case. Similar to the results in simulation, the resolution of the image is improved and the image becomes clear as the sampling rate increases (Fig. 6-8). In addition to improve temporal resolution, the Weiner filter is applied to this signals. Although ghost appear near the cavity, the cavity becomes smaller than that without applying Weiner filter.

The inverse filter discussed in Chapter 4 is applied to these signals. The diffraction hyperbola both without filtering and with filtering are shown in Figs. 6-10 and 6-11, re-

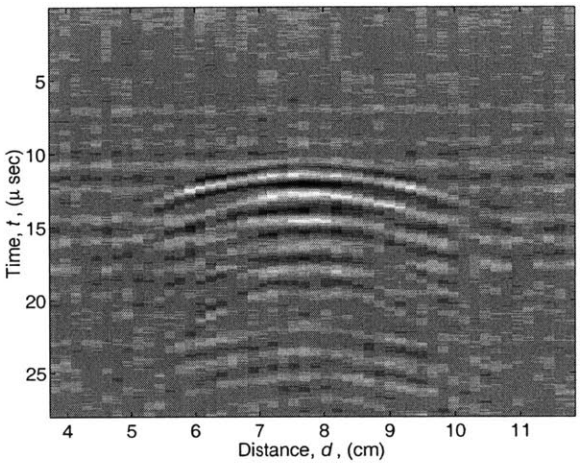

Figure 6-3: Case 1: The zoomed diffraction curve by the cavity in aluminum specimen, spatial sampling rate: 1.59 mm, depth of cavity: 30.00 mm, the radius of the transducer: 6.35mm.

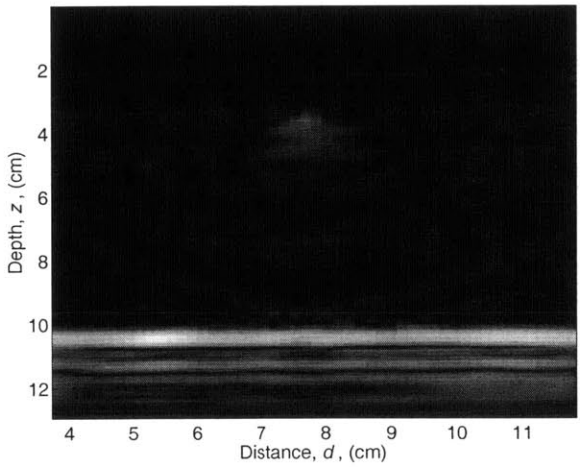

Figure 6-4: Case 1: The image of the cavity and the border of the aluminum specimen, spatial sampling rate: 1.59 mm, depth of cavity: 30.00 mm, the radius of the transducer: 6.35mm.

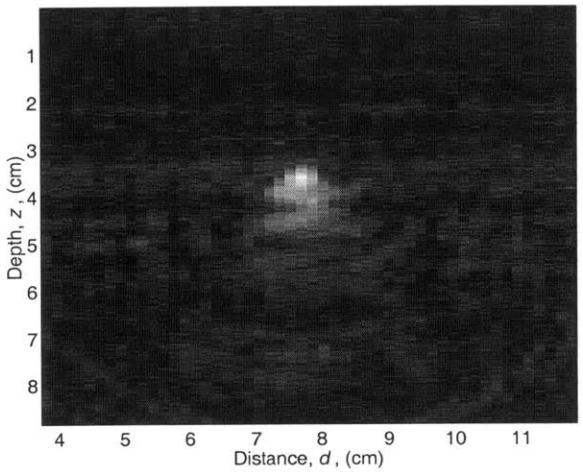

Figure 6-5: Case 1: The zoomed image of the cavity in aluminum specimen, spatial sampling rate: 1.59 mm, depth of cavity: 30.00 mm, the radius of the transducer: 6.35mm.

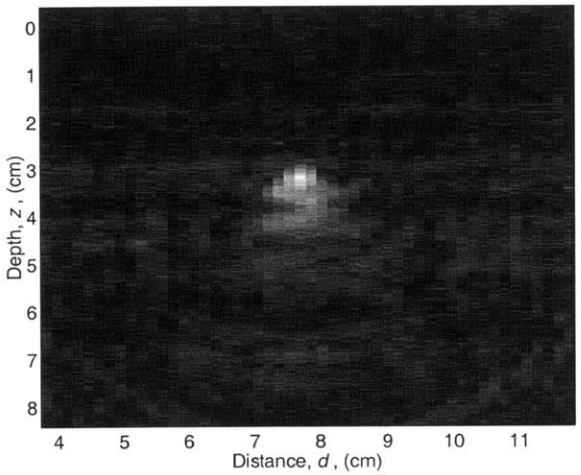

Figure 6-6: Case 1: The zoomed image of the cavity in aluminum specimen, spatial sampling rate: 1.59 mm, depth of cavity: 30.00 mm, the radius of the transducer: 6.35mm. The wave speed in the water is considered, then the image is located at proper position.

spectively. This filter not only eliminate the effects of the beam directivity and compensate travel time obliquely arrived at receivers but also remove noise. Because the wave number of reflected P-wave must be real number in f-k_x domain, the signals which has complex wave number is noise. By analysing only real wave number region, some of the noise can be removed (Fig. 6-11). The migration is carried out using filtered diffraction curve (Fig. 6-12). Although the size of the image becomes bigger, the ghost becomes smaller and the image becomes brighter than that without filtering.

The image for deeper cavity case is shown in Fig. 6-13. The cavity appears bigger than the shallower cavity case. It is because the gradient of the diffraction curve became lower the depth increases. This tendency is also observed in the simulation studies. Figure 6-15 shows the constructed image of the specimen with multiple cavities. Note that because the echo from the cavity located at 1.8 mm is so weak that it is not shown in this figure. The reflected wave off the deeper cavities is stronger than it off the shallower one.

Next, the results for the specimen with an inclined crack case are shown in Fig. 6-16. The reflected signal off the crack is so strong that the image of the crack and boundary can be seen together. The length and angle of the image is as same as actual one.

6.2 Mortar specimen

Figure 6-17 shows the dimension of the mortar specimen. In this experiment, 500 kHz unfocused transducers are directory placed on the surface of a mortar specimen. The outer

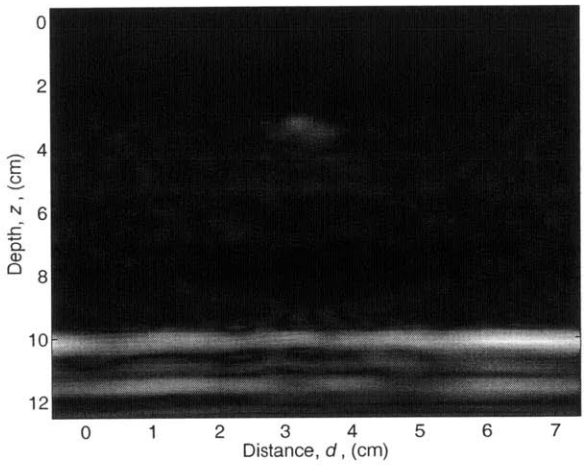

Figure 6-7: Case 2: The image of the cavity and the border between of aluminum specimen, spatial sampling rate: 0.80 mm, depth of cavity: 30.00 mm, the radius of the transducer: 6.35mm.

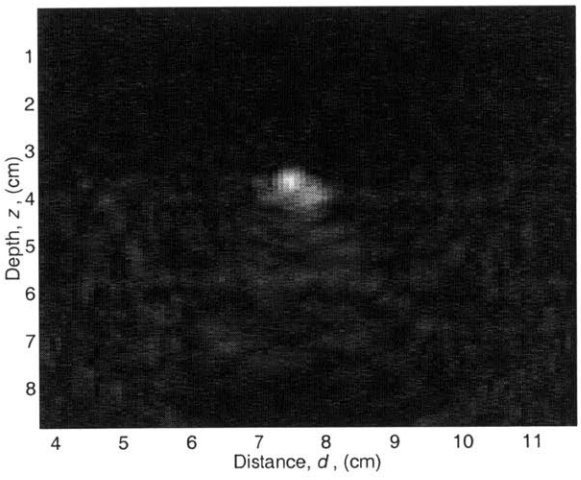

Figure 6-8: Case 2: The zoomed image of the cavity and the border of aluminum specimen without filtering process, spatial sampling rate: 0.80 mm, depth of cavity: 30.00 mm, the radius of the transducer: 6.35mm.

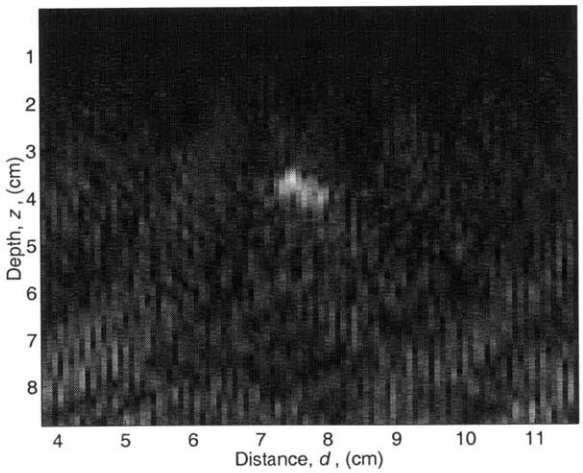

Figure 6-9: Case 2: The Wiener filter is applied to improve temporal resolution of the image of the cavity in aluminum specimen, spatial sampling rate: 0.80 mm, depth of cavity: 30.00 mm, the radius of the transducer: 6.35mm.

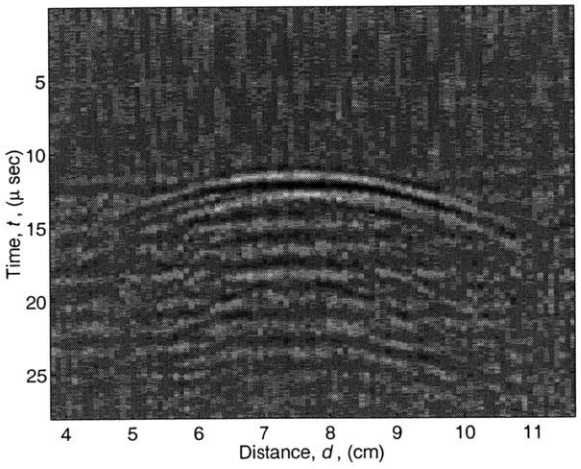

Figure 6-10: Case 1: The zoomed diffraction curve by the cavity in aluminum specimen, spatial sampling rate: 1.59 mm, depth of cavity: 30.00 mm, the radius of the transducer: 6.35mm.

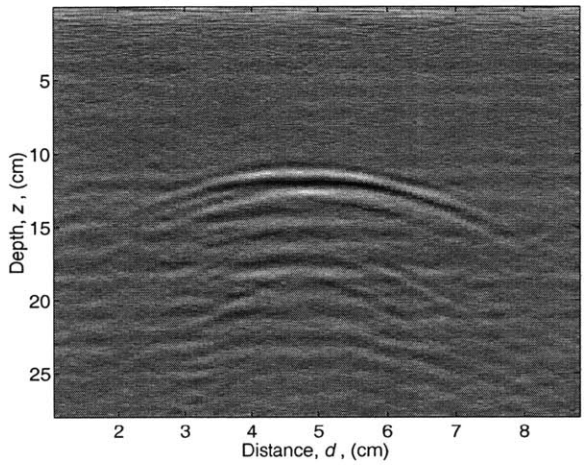

Figure 6-11: Case 1: The zoomed diffraction curve by the cavity in aluminum specimen, spatial sampling rate: 1.59 mm, depth of cavity: 30.00 mm, the radius of the transducer: 6.35mm.

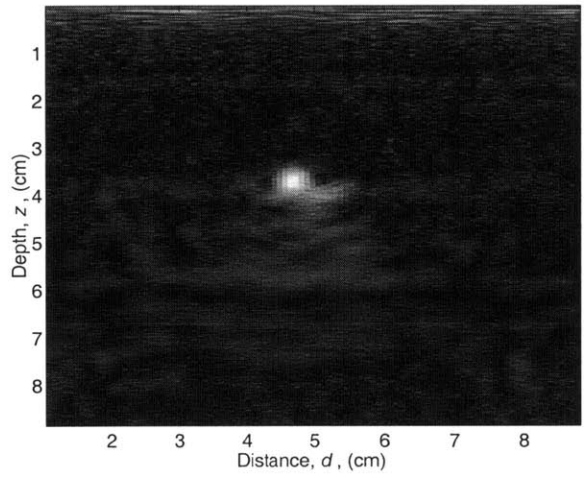

Figure 6-12: Case 2: The inverse filter discussed in Chapter 4 is applied to construct a clear image of the cavity in aluminum specimen, spatial sampling rate: 0.80 mm, depth of cavity: 30.00 mm, the radius of the transducer: 6.35mm.

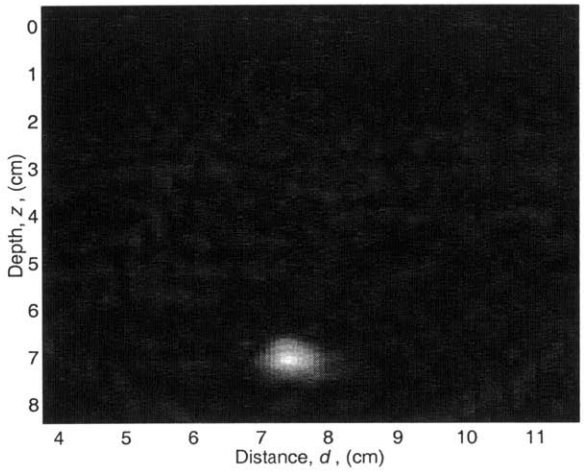

Figure 6-13: Case 3: The zoomed image of the cavity in aluminum specimen, spatial sampling rate: 0.80 mm, depth of cavity: 30.00 mm, the radius of the transducer: 6.35mm.

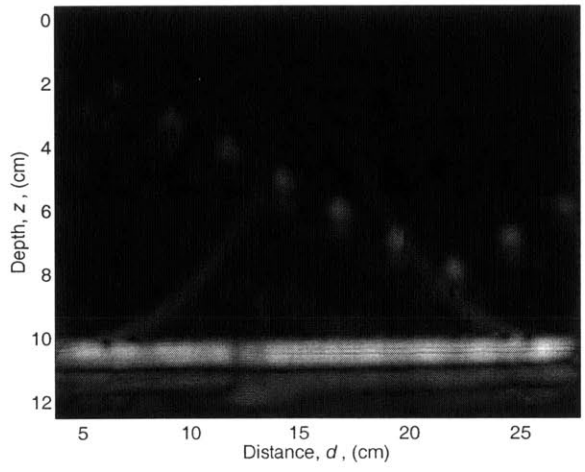

Figure 6-14: Case 4: The image of the cavities and the border of aluminum specimen, spatial sampling rate: 0.80 mm, depth of cavity: 30.00 mm, the radius of the transducer: 6.35mm.

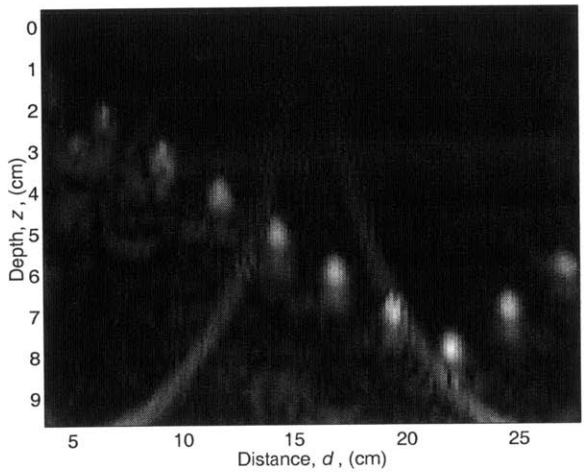

Figure 6-15: Case 4: The zoomed image of the cavities in aluminum specimen, spatial sampling rate: 0.80 mm, depth of cavity: 30.00 mm, the radius of the transducer: 6.35mm.

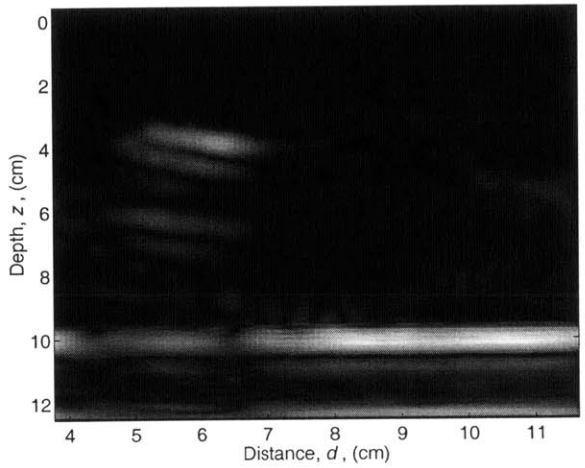

Figure 6-16: Case 6: The image of the crack in aluminum specimen, spatial sampling rate: 0.80 mm, depth of cavity: 30.00 mm, the radius of the transducer: 6.35mm.

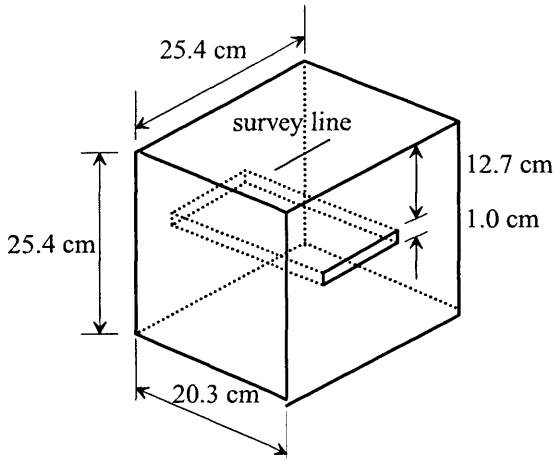

Figure 6-17: The dimension of the mortar specimen. The polyethylene plate is ended in the middle of the specimen.

Table 6.3: The configuration of the parameters used in the experiment (crack model)

Specimen	Mortar
Model	One delamination
The depth of discontinuity	12.7 mm
The angle of crack	0 °
Transducer	500 kHz flat
Radius of the transducer	14.3 mm
Sampling frequency	10 MHz
Data number	2000
Offset	50.8 mm
The number of shot	50

dimension of the mortar specimen is 10 in. × 10 in. × 8 in. and a polyethylene of 10 mm thickness plate is embedded at the middle of the specimen. The dimension of the mortar specimen is shown in figure 6-17. The wave speed in the mortar and in the polyethylene are 4530 m/s and 2360 m/s, respectively.

The data stacking is applied to the signals. The 12 time histories of which the nearest offset is 5.08 cm and the farthest offset is 8.57 cm are used for CMP stacking. Time histories of each offset measured at the 10th and 45th CMP are shown in figure 6-18 and 6-19. The amplitudes of each signal are normalized by the maximum amplitudes. The predicted arrival time of surface wave is 20.16 μsec for the nearest offset data and 34.02 μsec for the farthest offset data. The predicted arrival time of P-wave from the upper surface of the polyethylene plate is 57 μsec for the nearest offset data and 59 μsec for the farthest offset data. At the 10th CMP, reflected wave off the top surface of the polyethylene plate is clearly shown at approximately 60 μsec, however, no significant signal is observed at the 45th CMP. There may be an unexpected delamination at the 45th CMP, because waves observed at 17 μsec can be regarded as reflected waves, considering the shape of the wave and different arrival time from the surface wave. Since most of the energy of incident wave is reflected from these delaminations, the waves reached to the top of polyethylene plate becomes weak. Furthermore, the reflected wave from the unexpected delamination may change its mode to surface, PS and SS wave and they become strong noise. These two phenomena decrease the SNR significantly and make hard to obtain clear image of the polyethylene plate.

The stacked signal is compared with the waveform recorded at the nearest receiver (Fig. 6-20). For the comparison, the stacked signal is normalized by dividing the amplitude. In the figure, the reflected signal appearing approximately 60 μsec is boosted while keeping the amplitude of the noise low level. As discussed previously in Chapter 4 and described in

the reference [15], data stacking process is efficient to improve the SNR of a noisy signals. The diffraction curve and the image of the internal structure of the specimen is shown in Figs 6-21 and 6-21. The embedded polyethylene plate can be seen in the left hand side of the image (Fig. 6-23). The 10th CMP is there. The SNR of the signal observed at this region is not quite good, however, due to the data stacking, the SNR is improved and the clear image can be obtained. On the other hands, the image of the polyethylene plate cannot observed in the right hand side (Fig.6-24). The 45th CMP is there. Several unexpected delaminations are seen in this figure for example (distance, depth) = (7, 13.5) cm and (8, 14) cm. According to the Chapter 4 and 5, the image of shallow delamination is tend to be distorted because the directed beam cannot reach to the point of small depth-offset ratio. Therefore, the migration is carried out using the closest three offset data to investigate the unexpected delamination. The image is shown in figure 6-25. In this figure, it is clear that the delamination is at the depth 4 cm, which is equivalent to the reflected wave observed at 17 μsec of the time histories measured at the 45th CMP.

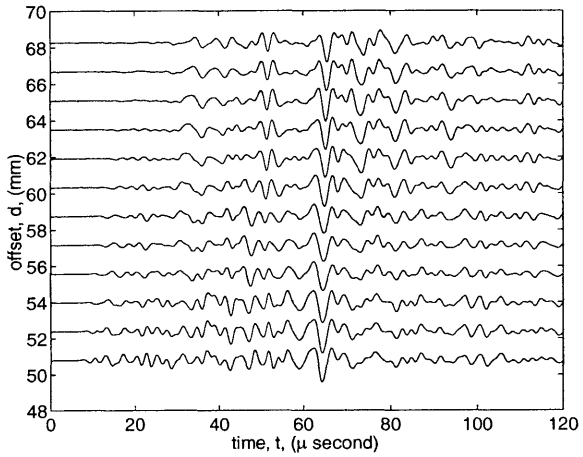

Figure 6-18: The time histories measured at CMP 10. The reflected signal off the top surface of the polyethylene is seen at 60 μ sec.

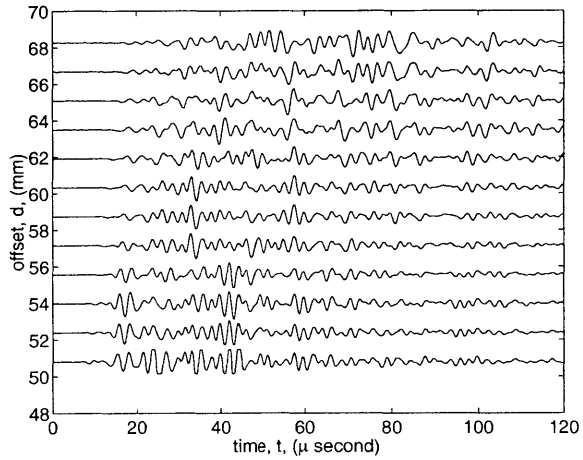

Figure 6-19: The time histories measured at CMP 45.

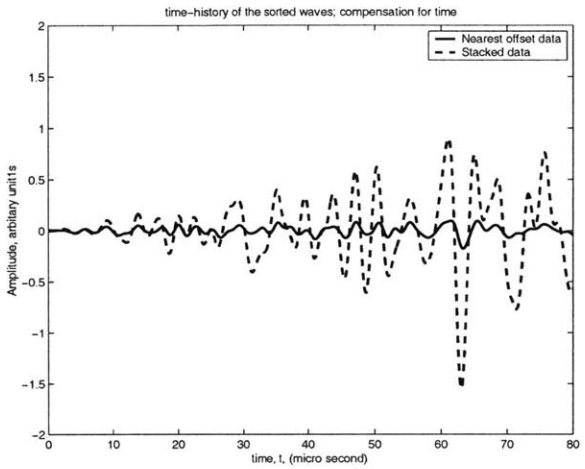

Figure 6-20: The stacked time history is compared with the time history measured at nearest offset receiver. The reflected signal is boosted up.

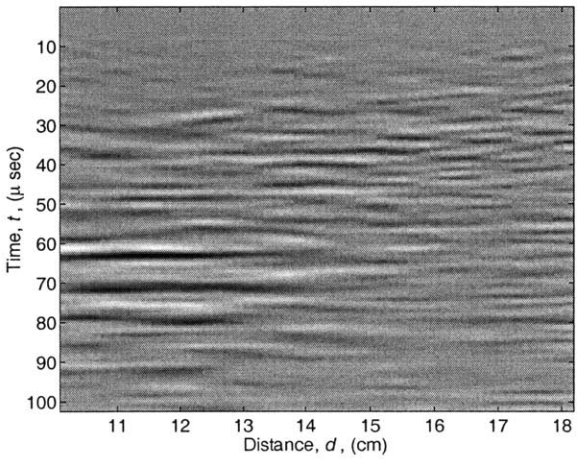

Figure 6-21: The reflected waves obtained from mortar specimen.

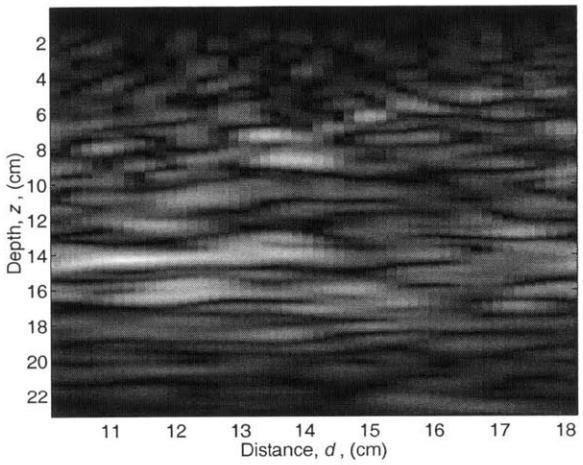

Figure 6-22: The image of the embedded polyethylene plate in mortar.

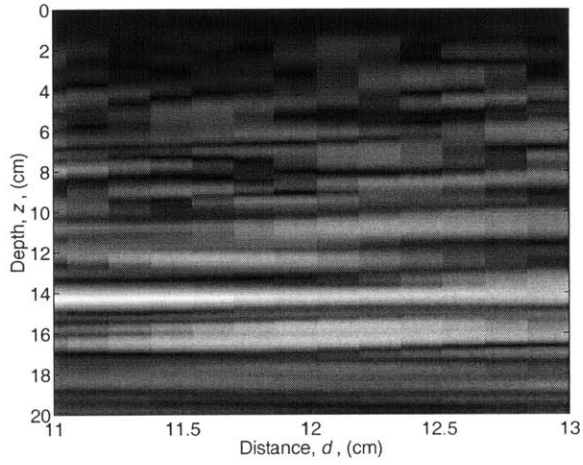

Figure 6-23: Part of the image of the polyethylene plate embedded in the mortar specimen (11 cm – 13 cm). The image is clear at this part.

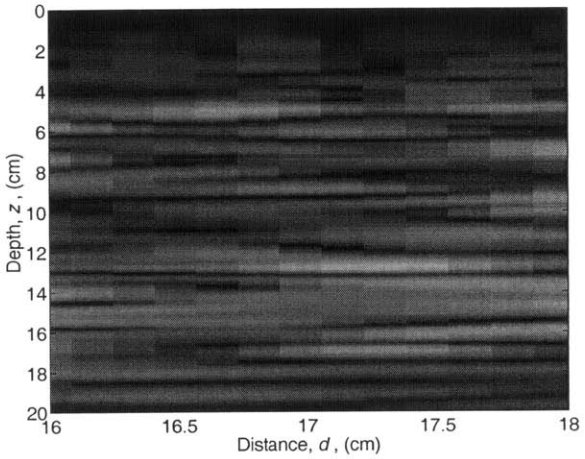

Figure 6-24: Part of the image of the polyethylene plate embedded in the mortar specimen (16 cm – 18 cm). The image is obscure at this part.

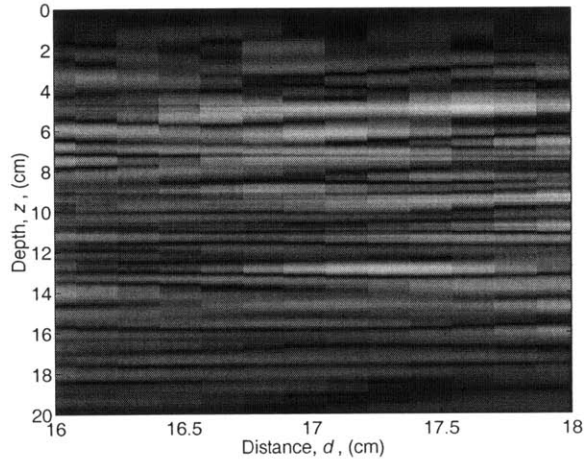

Figure 6-25: The image of the polyethylene plate embedded in the mortar specimen. This image is obtained using nearest three offset data.

Chapter 7

Conclusions and Future Work

In this chapter, at first, the conclusion is described and finally the future work is discussed.

7.1 Conclusions

The following conclusions are drawn from this study.

7.1.1 Noise

- The data stacking process improve the signal-noise-ratio.
- The function of the inverse filter to eliminate the signal which wave number is a complex number remove noise on the experimental data.

7.1.2 Directivity

- Beam directivity should be considered in a design of an array. Large number of receivers is not efficient for the array which consists of a transmitter of well-directed beam.
- Well-directed beam distort the image. The image is skewed and ghost appears around the image.
- Due to the beam directivity, the image of extremely shallow reflector is not constructed correctly.
- Inverse filter reconstruct clear image from distorted signals, except for the reflected signal from extremely shallow reflector and the reflected signal by the beam of narrow main lobe.

7.1.3 Preferable condition of the system

- Broad band and omni-directivity transducer
- No side lobe in the directivity pattern of transducer
- small offset value
- Enough spatial sampling rate and temporal sampling frequency not to cause aliasing

7.1.4 Feasibility of reflection seismology

- Reflection seismology is feasible for small scale structures, but scale effects should be taking into account, such as beam directivity.

7.2 Future Works

The image of inner structure of concrete cannot obtained in this study. The considerable reason is that the transducer is not appropriate for concrete inspection. It is say that center frequency of this transducer is high, the power given to transducer is not enough, or the incident wave propagates only within very narrow angle, etc. As future work, experiments with appropriate transducer is considered.

Bibliography

[1] O Büyüköztürk, "Imaging of concrete structures," *NDT&E Int.*, **31**(4), 233–243, 1998.

[2] H.W. Cole, *Understanding radar*, 2nd ed., Blackwell Scientific, 1992.

[3] G. Franceschetti and R. Lanari, *Synthetic aperture radar processing*, CRC press, 1999.

[4] P. Kearey and M. Brooks, *An introduction to geophysical exploration*, 2nd ed., Blackwell Scientific, 1991.

[5] Ö. Yilmaz, *Seismic Data Processing*, Society of Exploration Geophysics, 1987.

[6] E.A. Kozlov, *Migration in Seismic Prospecting*, Ashgate Publishing Company, 1990.

[7] M. Krause, F. Mielentz, B. Milman, W. Müller, V. Schmitz and H. Wiggenhauser, "Ultrasonic imaging of concrete members using an array system," *NDT&E Int.*, **34**, 403–408, 2001.

[8] P.-L. Liu, C.-D. Tsai and T.-T. Wu, "Imaging of surface-breaking concrete cracks using transient elastic waves,"*NDT&E Intl.*, **29**, 323–331, 1996.

[9] P.-L. Liu, K.-H Lee, T.-T. Wu and M.-K Kuo, "Scan of surface-opening cracks in reinforced concrete using transient elastic waves,"*NDT&E Int.*, **34**, 219–226, 2001.

[10] P.M. Shearer, *Introduction to Seismology*, Cambridge university press, 1999.

[11] G.F. Miller and H. Pursey, "The field and radiation impedance of mechanical radiators on the free surface of a semi-infinite isotropic solid," Proc. R. Soc. London, Ser. **A 223**, 521–541 1954.

[12] S.-C. Wooh and Q. Zhou, "Behavior of laser-induced ultrasonic waves radiated from a wet surface. Part I. Theory," *J. Applied Physics*, **89**, 3469–3477, 2001.

[13] Y.-H. Pao and C,-C. Mow, *Diffraction of Elastic Wave and Dynamic Stress Concentration*, Crane Russak, 1973.

[14] I.D. Hale, *Dip-Moveout by Fourier Transform*, Ph.D.thesis, Stanford university, 1983.

[15] Y.-F. Chang, C.-Y. Wang and C.-H. Hsieh, "Feasibility of detecting embedded cracks in concrete structures by reflection seismology," *NDT&E Int.*, **34**, 39–48, 2001.

Appendix A

Matlab code

A.1 Weiner prediction filter

[Definition of the parameters]

```
B      = 500*1e3          ; % Band width (Hz)
freq   = 1*1e6            ; % Frequency of the Signal (Hz)
num    = 2048             ; % Number of data(time)
sfreq  = 25*1e6           ; % Sampling frequency (Hz)
c      = 6.32*1e3         ; % Wavespeed in the object (m/s)
t0     = 0.5e-5           ; % Location of the reflector1
t1     = 3.0e-5           ; % Location of the reflector2
alpha  = 1                ; % Time lag
lf     = 128              ; % Length of the filter
ep     = 0.001            ; % white noise
y      = amp(1:lf+alpha)  ; % measured signal
time   = t/10^(-6)        ; % time for axis
```

[Culculation of the variables]

```
al   = B/2*2*pi   ; % a variable to control band width
w0   = 2*pi*freq  ; % Angular frequency
```

[Generation of the input signal]

```
t     = (1:num)/sfreq                                                    ;
amp   = zeros(1,num)                                                     ;
wave  = exp(-1e6*(1/sfreq:1/sfreq:5/freq)).*sin((1/sfreq:1/sfreq:5/freq)*w0)  ;
nw    = length(wave)                                                     ;

for l=33:32+nw
    amp(l) = amp(l)+wave(l-32) ;
end
for l=513:512+nw
    amp(l) = amp(l)+wave(l-512) ;
end
for l=535:534+nw
    amp(l) = amp(l)+wave(l-534) ;
end
```

[Calculation of auto-correlation]

```
ac = zeros(1,lf+alpha) ;

for i=1:lf+alpha
    for k=1:lf+alpha-i+1
        ac(i)=ac(i)+y(k)*y(i+k-1) ;
    end
end

ac = ac/max(ac) ;
ac(1) = ac(1)+ep ;
```

[Calculation of filter operator]

```
m = 1 ;
r = zeros(lf,lf) ;


for ik = 1:lf
    for m:lf
        r(ik,i) = ac(i-m+1) ;
    end
    if m > 1
      for i=1:m-1
          r(ik,i) = ac(m-i+1) ;
```

```
      end
    end
    m = m + 1 ;
end
for i=1:lf
    ra(i) = ac(alpha+i) ;
end


aa = inv(r)*ra' ;
a(1) = 1 ;


if alpha > 1
  for i = 2:alpha ;
      a(i) = 0 ;
  end
end
for i = alpha+1:alpha+lf
    a(i) =-(aa(i-alpha)) ;
end


c = conv(a, amp) ;
```

[Plotting]

```
subplot(2,1,1);
plot(time,amp);
axis ([0 40 -1 1]);
xlabel('Time, t, \ second')
ylabel('Amplitude, arbitrary unit')
title('(a) Before deconvolution')

    subplot(2,1,2);
plot(time,c(1:num));
axis ([0 40 -0.5 0.5]);
xlabel('Time, t, \ mu second ')
ylabel('Amplitude, arbitrary unit')
title('(b) After deconvolution')
```

A.2 Migration

Definition of the parameters

```
num    = 2048              ; % Number of data(time)
sfreq  = 25*1e6            ; % Sampling frequency (Hz)
c      = 6.32*1e3          ; % Wavespeed in the object (m/s)
snum   = 50                ; % Number of CMP
mf     = 4                 ; %
numd   = 1024              ; % Data number for display
num    = numd*mf           ; % Data number
sx     = 0.00159           ; % Sampling rate
nkx    = 1/(2*sx)          ; % Nyquist wave number
nkz    = 1/(2*(c/2)/sfreq) ; % Nyquist wave number
```

initialization of matrix

```
fts   = zeros( num,snum) ;
fts1  = zeros(num/2,snum) ;
fts2  = zeros(num/2,snum) ;
fts3  = zeros( num,snum) ;
C     = zeros( num,snum) ;
```

read files

```
for i = 1: snum ;
    filenamel = strcat('expt1c_', num2str(i)) ;
    filenamer = '.dat' ;
    filename = strcat(filenamel, filenamer) ;
    fid = fopen(filename,'r') ;
    x = fscanf(fid, '%f' ,[2,inf]) ;
    y = (x(2, 1:num/mf))' ;
    C(1:num/mf, i) = y - mean(y) ;
    fclose(fid)
end
```

Set the property for axis

```
time  = [1:num]./sfreq*10^6          ; % t-axis (μsec.)
x     = 1.5*0.0254+(0:snum)*sx       ; % x-axis (m)
xf    = (-snum/2:snum/2)/(num*sx)    ; % kx-axis (Hz)
yf    = (1:num/2)/(num/sfreq)        ; % ky-axis (Hz)
```

Plot the diffraction curve

```
h = axes('fontsize',16) ;
imagesc(x*10^2,time(1:numd),C(1:numd,:));
ylabel('Time, t , (\mu sec)')
xlabel('Distance, d , (cm)')
```

Two dimentional Fourier transform

```
fts = fft2(C); fts1(1:num/2, 1:snum/2) = fts(1:num/2, snum/2+1:snum);
fts1(1:num/2, snum/2+1:snum) = fts(1:num/2, 1:snum/2);
```

Geometrical transform

```
for n=1:snum ;
    kx = -nkx-nkx/(snum-1)+nkx*2/(snum-1)*(n-1) ;
    ft = zeros(1,num/2) ;
    idex = 0 ;
    for i=1:num/2 ;
        omega(i)=sfreq/num*(i-1) ;
        if omega(i)^2/(c/2)^2-kx^2 ¿ 0
          idex=idex+1 ;
          kzst(idex) = nkz*2/num*idex ;
          kz(idex) = sqrt(omega(i)^2/(c/2)^2-kx^2) ;
          f1 = c/2*kz(idex)/sqrt(kx^2+kz(idex)^2) ;
          ft(idex) = fts1(i,n)*f1 ;
        end
    end
    map = interp1(kz(1:idex), ft(1:idex), kzst(1:idex), 'cubic') ;
    lmap=length(map) ;
    for l=1:lmap ;
        p=isnan(map(l)) ;
        if p > 0 ;
          fts2(l,n)=0 ;
        else
          fts2(l, n)=map(l) ;
        end
    end
end


fts3(1:num/2, 1:snum/2) = fts2(1:num/2, snum/2+1:snum) ;
fts3(1:num/2, snum/2+1:snum) = fts2(1:num/2, 1:snum/2) ;
```

Inverse Fourier transform

```
MD=ifft2(fts3) ;
MD=abs(MD) ;
```

Plot the image of inner structure

```
figure ;
h = axes('fontsize',16) ;
colormap(gray)
imagesc(x*10^2, time(1:numd)*c/2*10^(-4), MD(1:numd,:)) ;
ylabel('Depth, z , (cm)')
xlabel('Distance, d , (cm)')
print -deps expt1alxz
```